Studies of Thin Metal Silicides on Silicon (111)

Ian Matthew Scott

Submitted for the Degree of Doctor of Philosophy

University of York

Department of Physics

September 2004

Abstract

This work describes the study of RE/Si(111) (RE – rare earth) and Fe/Si(111) surfaces by means of medium energy ion scattering (MEIS), scanning tunnelling microscopy (STM) and scanning tunnelling spectroscopy (STS).

The Tm/Si(111) surface has been studied by means of MEIS. Data has been obtained from the 1 × 1 surface reconstruction formed at monolayer rare earth coverage. The data have been compared to simulations for a model based on the known structures of other RE silicides. The structure of the Tm silicide formed has been seen to fall into this class of structure. This investigation has led to a re-evaluation of the determination of the structural parameters for this model. A trend in the structural parameters has been revealed across the rare earth series.

The electronic structure of the rare earth silicide surface has been investigated. STS has been performed on the Ho silicide 1 × 1 surface. A lack of distinction between inequivalent sites has been observed and the data found to be in broad agreement with what is known of the electronic structure of these RE silicides.

A MEIS investigation has been made of the initial growth of Fe on the Si(111) 7 × 7 surface. Two phases have been found to form depending on anneal temperature. At anneal temperatures of around 300 ˚C a 1 × 1 phase is formed and at higher anneal temperatures a 2 × 2 phase is found. Data have been obtained from three scattering geometries. The data indicate that both phases are structurally very similar. A CsCl-type structural model is proposed, the 2 × 2 phase being formed by a Si adatom overlayer.

The use of the RE silicide as a growth template has also been briefly investigated by MEIS. The deposition of Fe onto the Ho silicide surface has been found to disrupt the structure and progressive annealing failed to reorder the system.

Contents

Contents 3

List of Figures 8

List of Tables 18

Acknowledgements 19

Declaration 20

Publications 20

1 Introduction 21

1.1 The Surface 21

1.2 Techniques of Surface Science 23

1.2.1 Scanning Tunnelling Microscopy 24

1.2.2 Low Energy Electron Diffraction 24

1.2.3 Reflection High Energy Electron Diffraction 26

1.2.4 Medium Energy Ion Scattering 26

1.2.5 Surface X-Ray Diffraction 27

1.2.6 X-Ray Photoelectron Spectroscopy 27

1.2.7 Ultraviolet Photoelectron Spectroscopy 27

1.2.8 Auger Electron Spectroscopy 28

1.2.9 Electron Energy Loss Spectroscopy 29

1.2.10 Surface Extended X-ray Fine Structure 30

1.3 Metal–Semiconductor Interfaces 31

1.4 Materials Studied 33

1.4.1 Two Dimensional Rare Earth Silicides 33

1.4.2 Iron Silicides 35

1.4.3 Metal Growth on 2D Rare Earth Silicides 36

References 36

2 Experimental Aspects 41

2.1 The Daresbury MEIS Facility 41

2.2 Scanning Tunnelling Microscopy 44

2.2.1 General Principle 44

2.2.2 Theory 47

2.2.3 Scanning Tunnelling Spectroscopy 50

2.2.4 Apparatus 51

2.3 Low Energy Electron Diffraction 53

References 58

3 Medium Energy Ion Scattering 60

3.1 Introduction 60

3.2 The Technique of MEIS 61

3.2.1 Shadowing and Blocking 61

3.2.2 Kinematic Scattering 64

3.3 Simulation of Scattering Curves 69

3.3.1 Hitting and Detection Probabilities 69

3.3.2 Calculation of Probabilities: The Standard Method 71

3.3.3 Calculation of Probabilities: Tromp and van der Veen's Method 72

3.3.4 Connection of Ingoing and Outgoing Ion Tracks 75

3.3.5 Tracking of Ions: The Single Row Approximation 76

3.3.6 Tracking of Ions: The Complete Crystal Method 76

3.3.7 Multiparameter Simulations....78

3.4 Comparison of Simulation with Experimental Data....78

References....79

4 MEIS Investigation of Thulium Silicide 82

4.1 Introduction....82

4.2 Experimental Details....82

4.3 Results and Discussion....87

4.3.1 Experimental Results and Analysis....87

4.3.2 Computer Simulations....89

4.3.3 Re-examination of Best Fit Model....94

4.4 Conclusion....97

References....99

5 Structural Trends and the Influence of R-factors 101

5.1 Introduction....101

5.2 A Possible Trend....103

5.3 The Possible Influence of the R-factor....106

5.4 Re-examination of MEIS Structural Results....107

5.5 Examining the R-Factor....109

5.5.1 The Influence of the Low Angle Blocking Dip....109

5.5.2 Alternative R-Factors....112

5.5.3 Performance of the R-factors....114

5.5.4 Errors in the Results....118

5.5.5 Conclusion....120

5.6 Conclusion 121

References 123

6 MEIS Study of the Initial Growth of Fe on Si(111) 125

6.1 Introduction 125

6.2 Experimental Details 126

6.3 Results and Discussion 127

6.3.1 Experimental Data 127

6.3.2 Possible Models 133

6.3.3 Optimising Structural Parameters 134

6.4 Conclusions 139

References 140

7 Studies of the 2D Silicide Surface 143

7.1 Introduction 143

7.2 STS of 2D Holmium Silicide 143

7.2.1 Introduction 143

7.2.2 Experimental 144

7.2.3 Scanning Tunnelling Microscopy 145

7.2.4 Scanning Tunnelling Spectroscopy 146

7.2.5 Spatially Resolved Spectra 148

7.3 Initial MEIS Study of Fe Growth on 2D Holmium Silicide 151

7.3.1 Introduction 151

7.3.2 Experimental 151

7.3.3 Results and Discussion 152

7.4 Conclusion 155

References 155

8 Conclusion 158

8.1 MEIS Study of Thulium Silicide 158

8.2 Structural Trends in 2D Silicides 159

8.3 R-factor Analysis of MEIS Data 160

8.4 Iron Growth on Si(111) 161

8.5 Studies of the Silicide Surface 162

8.5.1 Iron Growth on 2D Silicides 162

8.5.2 STS of 2D Silicide 162

8.6 Future Work 163

Glossary 165

List of Figures

Figure 1.1: Simplified side view of a) a surface relaxation in which the atomic spacing changes near to the surface; b) a surface reconstruction, in which the atomic arrangement reconfigures to produce a new two-dimensional unit cell. 22

Figure 1.2: The Auger process. A high energy electron removes a core level electron from the atom (a), leaving an excited state (b). The atom relaxes via a less tightly bond electron filling the core level hole. The energy liberated causes the ejection of a third, Auger electron (c). 28

Figure 1.3: Formation of a Schottky barrier, Φ_{SB}, for an n-type semiconductor in contact with a metal. The Schottky barrier forms, and the junction is rectifying, if the metal wor function, φ_m, is greater than the semiconductor workfunction, φ_s. E_v is the top of the valence band, E_c the bottom of the conduction band and E_f the Fermi level. The band gap of the semiconductor, E_g is also indicated. 32

Figure 1.4: Structure of the 2D RE silicides. The RE forms a single atomic layer situated in T4 sites above the bulk Si. The silicide is terminated by a bulk-like Si bilayer, rotated by 180° with respect to the bulk. Top: Side view. Bottom: Top view (i.e. along the surface normal). Inset: Ball and stick model of the surface. 34

Figure 2.1: Schematic diagram of the Daresbury MEIS facility beam line. Ions are produced by a duoplasmatron source and accelerated to around 100 keV. The ion beam is then focused and collimated before entering the scattering chamber. 41

Figure 2.2: Schematic diagram of the Daresbury MEIS facility user end station. The ion beam enters at the main scattering chamber. Sample preparation is performed in a separate chamber and sample storage and fast entry is also available. 42

Figure 2.3: The torodial electrostatic analyser and 2D detector produce the 2D data sets in MEIS experiments. Ions entering the detector are bent through 90˚ before hitting a set of channel plates which amplify the charge so it may be detected by the 2D detector plate. 44

Figure 2.4: The general operation of the scanning tunnelling microscope in constant current mode. As the tip is scanned across the surface its z-position is adjusted to maintain a constant tunnelling current. This results in the tip following the contours of the surface... 45

Figure 2.5: The model tip used in the calculations of Tersoff and Hamann [13, 14]. The tip is taken as a spherical potential well of radius R, centred at $\mathbf{r_0}$ a distance d above the surface... 47

Figure 2.6: Qualitative description of the reciprocity principle. Probing surface s states with a tip d state is equivalent to probing d states with a tip s state... 49

Figure 2.7: Bias condition dependence of STM imaging, in the case of the Si(111) 7×7 surface. (a) Unoccupied states with the sample biased at +1.5 V. (b) Occupied states with the sample biased at –1.5 V. The unit cell is marked in each case. Note that in the case of (b) a difference is clear between the faulted and unfaulted half of the unit cell, whilst in (a) the two halves appear the same. From Avouris & Wolkow [16]............................. 50

Figure 2.8: Schematic diagram of the STM 1 system. The STM is housed in a UHV side chamber attached to a UHV sample preparation chamber equipped with LEED, AES and deposition sources.................................... 52

Figure 2.9: Schematic diagram of AFM/STM systems used. The UHV STM side chamber may be isolated from the main UHV sample preparation chamber. Samples may be quickly exchanged in and out of the system using a load lock 52

Figure 2.10: Simple diffraction in 1D. Constructive interference occurs when the Bragg condition is met, i.e. path difference d=nλ, λ being the electron wavelength and n=...-2,-1,0,1,2,3,.. 54

Figure 2.11: The Ewald sphere for elastic scattering in 2D. The bragg condition $\mathbf{k_i}-\mathbf{k_s}=\mathbf{g}$ is met whenever the sphere crosses a reciprocal lattice rod. 55

Figure 2.12: An example LEED pattern [24], showing the diffraction pattern from the clean Si (111) 7 × 7 surface with incident electron energy of 40 eV. Note that the periodicity of the surface is immediately apparent................56

Figure 2.13: Typical LEED apparatus. Electrons are diffracted from the sample and accelerated between the grid G1 and the fluorescent screen. The grids G2 and G3 filter out the lower energy, inelastically scattered electrons to reduce the background. It is often the case that the fluorescent screen is deposited on a window so that the pattern may be viewed through the glass to avoid the problems with the screen being obscured by the sample mountings. 57

Figure 3.1: Shadowing. By aligning the ion beam along a low index crystallographic direction, the atoms deeper in the crystal are effectively shadowed from the beam. 62

Figure 3.2: Blocking. Scattered ions are blocked in their path back out of the crystal by atoms closer to the surface in a process analogous to the initial blocking. A shift in atomic position results in a shift in the angular position of a blocking feature..63

Figure 3.3: The kinematic factor k^2 as a function of scattering angle for two target masses of 28 amu and 168 amu, calculated for the case of H^+ ions. .64

Figure 3.4: An example MEIS spectra (taken from the Tm 2D silicide system, see Chapter 4 for details). This spectrum demonstrates many of the features of a typical MEIS spectrum. The signals from scattering from the Si and Tm are well separated due to the mass difference between the two elements. The Tm scattering signal shows the characteristic fall in counts at increasing scattering angle due to the Rutherford scattering cross-section. The drop in energy with increasing scattering angle is most evident in the Si scattering signal. The Tm scattering signal shows clear evidence of ions being blocked at specific scattering angles. The detection around a major crystallographic direction is evidenced by the bulk blocking feature....................................65

Figure 3.5: The energy loss due to inelastic scattering becomes greater the deeper the ion penetrates. An ion entering the crystal with energy E_0 and being scattered at a depth d from the surface exits with energy given by Equation 3.9. 67

Figure 3.6: Basic double alignment scattering. Open circles indicate equilibrium positions of atoms, filled circles the thermally displaced positions in the crystal snapshot. The ion enters parallel to the z_1-axis, scatters from atom A and exits parallel to the z_2-axis 70

Figure 3.7: Schematic of the standard scheme for determining hitting probabilities. The ion enters at $\mathbf{r_0}$ and scatters from each atom in turn before colliding with the atom located at $\mathbf{r_0} + \mathbf{\Delta n}$. Note the z´-axis is the z-axis of the Tromp and van der Veen method. 72

Figure 3.8: Schematic of Tromp and van der Veen's scheme for determining hitting probabilities. The ion enters along the z-axis and is scattered by each atom in turn until passing through the ith layer at $\mathbf{\Delta n}$, $\boldsymbol{\delta}\mathbf{r_i}$ from the ith atom. This scheme is related to Barrets by a simple coordinate transform (see Figure 3.7). 73

Figure 3.9: In the complete crystal method an auxiliary lattice can be constructed by grouping atoms with (nearly) identical x-, y- or z-coordinates. This can then be used to track the ion through the crystal. As each atom occupies one auxiliary lattice point, and each lattice point contains zero or one atoms, only four auxiliary lattice points need be checked for potential collision partners. 77

Figure 4.1: Structure of 2D rare earth silicides. The RE forms a single atomic layer located in T4 sites above the bulk Si. The silicide is terminated by a bulk-like Si bilayer (Si_1 and Si_2) which is rotated by 180˚ with respect to the bulk. a) side view, b) the view along the surface normal (i.e. top view). 83

Figure 4.2: The origin of the blocking dips in the Tm signal in the two scattering geometries indicated. a) [$\bar{1}$ 00]/[$\bar{1}$ 11] b) [1$\bar{1}$ $\bar{1}$]/[100]. The arrows indicate the origin of the blocking features labelled in Figure 4.5. Refer to Figure 4.1 for further details of the structure (note that in this figure only those atoms within the scattering plane are shown). Notice that ε depends only on Si_2..85

Figure 4.3: Typical MEIS spectra from the Tm silicide for the two experimental geometries employed (left [$\bar{1}$ 00]/[$\bar{1}$ 11]; right [1$\bar{1}$ $\bar{1}$]/[100]). The separation of the Tm and Si signals, and the bulk blocking features are all clearly visible. The Tm signal shows decreased intensity at scattering angles at which blocking has occurred..86

Figure 4.4: The comparison of a simulation of bulk terminated Si (111) to the experimental angular cross section through the bulk scattered ion signal, with angular offset applied. Matching the postition of the bulk blocking feature allows the angular scale to be calibrated correcting for any mechanical offset of the analyser. (a) [$\bar{1}$ 00]/[$\bar{1}$ 11] (b) [1$\bar{1}$ $\bar{1}$]/[100]..........88

Figure 4.5: The corrected angular cross section through the Tm signal for the (a) [$\bar{1}$ 00]/[$\bar{1}$ 11] geometry and (b) [1$\bar{1}$ $\bar{1}$]/[100] geometry. The curves have been corrected for the angular offset and the fall off in counts due to Rutherford scattering cross section, and scaled to an arbitrary value. Also shown for comparison purposes is the experimental cross section through the Ho signal from a 2D Ho silicide [5]. The similarity of the two curves indicates the structures are very alike, as expected. The small fluctuations within the curves are experimental noise. The labelling of blocking dips refers to Figure 4.2. 90

Figure 4.6: Ball and stick representation of the Tm 2D silicide surface, showing the bond lengths of Table 4.1..92

Figure 4.7: Comparison between experimental data and the simulated scattering curve for the initial structural solution for 2D Tm silicide (note that for ease of display the curves have been corrected for the fall off in counts due to the Rutherford scattering cross-section). The experimental data has been freely scaled to the simulation. (a) [$\bar{1}$ 00]/[$\bar{1}$ 11] (b) [1$\bar{1}$ $\bar{1}$]/[100]. The labelling of blocking dips refers to Figure 4.2. Note the poor match of the 57˚ (ε) blocking feature in the [$\bar{1}$ 00]/[$\bar{1}$ 11] geometry. 93

Figure 4.8: Comparison between experimental data and the simulated scattering curve for the final model for two-dimensional Tm silicide (again corrected for Rutherford scattering cross-section). The experimental yield is freely scaled to the simulation. (a) [$\bar{1}$ 00]/[$\bar{1}$ 11] (b) [1$\bar{1}$ $\bar{1}$]/[100]. The ~57˚ (ε) dip position is now visually a better fit. 95

Figure 4.9: Ball and stick representation of the Tm 2D silicide surface, showing the bond lengths of Table 4.2. 96

Figure 4.10: Comparison between experimental data and simulation for the “by eye” fit, corrected for Rutherford scattering cross-section. (a) [$\bar{1}$ 00]/[$\bar{1}$ 11] (b) [1$\bar{1}$ $\bar{1}$]/[100]. The ~57˚ (ε) dip position has been further improved. 98

Figure 5.1: (a) RE–Si bond lengths in bulk rare earth silicides. (b) Ionic radii of rare earth metals. Both show a decreasing trend across the series. 102

Figure 5.2: Comparison of experimental MEIS scattering curves for 2D rare earth silicides. This feature is due to the blocking of scattered ions by the Si_2 atoms and directly reflects the Si_2–RE bond length (the blocking dip labelled ε in the previous Chapter). Curves have been scaled to an arbitrary yield and then offset for clarity. 104

Figure 5.3: Comparison of experimental MEIS data for 2D rare earth silicides. The blocking dip shown is due to blocking of scattered ions by the Si_1 atoms (the blocking dip labelled δ in the previous Chapter). Curves have been scaled to a common arbitrary yield and then offset for clarity. 105

Figure 5.4: Contribution of each point to the total R-factor. Note the significance of the lowest angle dip. The dashed line shows similar contributions for the simulation of the final solution. 110

Figure 5.5: Contribution of each point to the total R-factor when the Rutherford scattering cross section is not taken into account. This eliminates the added weight given to lower angles due to the additional number of counts. The depth of the lowest angle dip is still the most important factor. 110

Figure 5.6: Contributions to the R-factor when discounting the lowest angle dip from the calculation of the R-factor. This produces a much better fit to the higher angle dips than that shown in Figure 5.4 and Figure 5.5. 112

Figure 5.7: Comparison of (a) the original Tm silicide MEIS scattering curve and (b) the “flipped” version. The inset shows a typical LEED I–V curve [10]. The Pendry R-factor was originally designed to deal with peaks rather than dips. The flipped data may be considered qualitatively more like the LEED data for which the Pendry R-factor is standard. 117

Figure 5.8: The structural trend in the Si_2–RE bond length across the rare earth series. This plot is derived from the structural model determined using R_{Pflip}. Other methods of determining the best fit model show is a similar trend. 122

Figure 6.1: Bulk phase diagram for Fe silicide. After von Kanel et al. [15]. The FeSi system exhibits many phases in the bulk dependent on the precise Fe:Si composition and sample preparation. 125

Figure 6.2: Typical MEIS spectra from the FeSi 1 × 1 phase. Left to right: $[\bar{1}00]/[\bar{1}11]$, $[1\bar{1}0]/[100]$, $[1\bar{1}\bar{1}]/[100]$. The Fe signal shows clear blocking dips. 128

Figure 6.3: Typical MEIS spectra from the FeSi 2 × 2 phase. Left to right: $[\bar{1}00]/[\bar{1}11]$; $[1\bar{1}0]/[100]$; $[1\bar{1}\bar{1}]/[100]$. The spectra are very similar to those observed for the 1 × 1 phase (Figure 6.2). 129

Figure 6.4: Comparison of scattering curves from the 1 × 1 and 2 × 2 phases. [$\bar{1}$00]/[$\bar{1}$11] geometry. The scattering curves from the two phases are extremely similar, indicating that their structures are very alike. See also Figure 6.5 and Figure 6.6. 131

Figure 6.5: Comparison of scattering curves from the 1 × 1 and 2 × 2 phases. [1$\bar{1}$0]/[100] geometry. See also Figure 6.4 and Figure 6.6.............................132

Figure 6.6: Comparison of scattering curves from the 1 × 1 and 2 × 2 phases. [1$\bar{1}\bar{1}$]/[100] geometry. See also Figure 6.4 and Figure 6.5............................132

Figure 6.7: The proposed structural model for the initial Fe silicide growth. Side view showing the scattering plane. Note that the 2 × 2 phase is shown; the 1 × 1 phase is proposed to be identical but without the ordered Si overlayer, Si_{ad}. Inset: Ball and stick model of the surface—the model on the right has the bulk Si removed for clarity...134

Figure 6.8: Origin of the blocking features. Note how the adatoms are mainly shadowed from the scattered ions. Red lines indicate the incident ion directions, green lines the origin of the observed blocking dips Top: [$\bar{1}$00]/[$\bar{1}$11] Bottom: [1$\bar{1}$0]/[100] and [1$\bar{1}\bar{1}$]/[100]—as ions are detected around [100] in both cases the same blocking dips are observed, although at different scattering angles. 135

Figure 6.9: Ball and stick model of the surface, showing the bond lengths detailed in Table 6.1. 136

Figure 6.10: Comparison of simulated and experimental scattering curves for the final structural model. The [$\bar{1}$00]/[$\bar{1}$11] geometry..................................137

Figure 6.11 Comparison of simulated and experimental scattering curves for the final structural model. The [1$\bar{1}$0]/[100] geometry...................................138

Figure 6.12: Comparison of simulated and experimental scattering curves for the final structural model. The [1$\bar{1}\bar{1}$]/[100] geometry..................................138

Figure 7.1: Theoretical band structure of RE 2D silicide [4]. Note the hole pocket at the $\bar{\Gamma}$ point. 144

Figure 7.2: Atomically resolved STM image of the 2D Ho silicide surface. Imaged aquired at a bias voltage of 2V, tunnelling current 2nA. ~10 nm × ~3 nm. 145

Figure 7.3: Inequivalent sites on the 2D silicide surface. Top: atomically resolved STM image, bias voltage 2 V, tunnelling current 2 nA. ~5.0 nm × ~3.6 nm. Bottom: Schematic top view of the surface. 146

Figure 7.4: Typical plot of tunnelling current, I, versus bias voltage, V, averaged from equivalent sites on the atomically resolved 2D silicide surface close to zero applied voltage. 147

Figure 7.5: The LDOS is better represented by a plot of (dI/dV)/(I/V) versus bias voltage. Arrowed are features corresponding to bands in the 2D silicide band structure 148

Figure 7.6: STS spectra from three inequivalent sites on the atomically resolved 2D Ho silicide surface. Arrowed are features corresponding to bands in the 2D silicide band structure.......... 149

Figure 7.7: Comparison of STS from a region of 2D silicide and various sites within the Si(111) 7 × 7 unit cell. 149

Figure 7.8: The sequence of MEIS spectra from Fe deposition on Ho 2D silicide. [$1\bar{1}0$] incident direction with detection around [100]. a) As deposited b) After anneal to ~550 ˚C c) After anneal to ~700 ˚C. The inset shows the Ho scattering signal from the 2D silicide before Fe deposition. The surface is initially disrupted and increasing annealing simply causes diffusion of the Fe and Ho into the bulk substrate.......... 153

Figure 7.9: Scattering cross section through the Ho (top) and Fe (bottom) signals of spectra shown in Figure 7.8. a) As deposited b) After anneal to ~550 ˚C. Inset: The scattering curve through the Ho signal before Fe deposition. The lack of blocking features in the Ho and Fe signals indicate a lack of order at the surface. 154

Figure 8.1: Side view of the Tm 2D silicide structure indicating the bond lengths. Bulk Si has been omitted for clarity. The silicide consists of a single RE layer beneath a bulk-like Si bilayer. The bilayer is rotated by 180° with respect to the bulk. 159

Figure 8.2: Side view of the Fe silicide, showing the 2 × 2 Si adatom layer and indicating bond lengths. Bulk Si has been omitted for clarity. The silicide is a CsCl-type structure with, in the case of the 2 × 2 phase, an additional layer of Si adatoms in a 2 × 2 arrangment. 161

List of Tables

Table 4.1: Structural parameters for the initial best model for the Tm silicide under discussion. The Si_1–Tm bond length is thought to be underestimated while the Si_1–Si_2 bond length is overestimated..94

Table 4.2: Structural parameters for the final model for 2D Tm silicide............96

Table 4.3: Structural parameters determined from a "by eye" fit.......................98

Table 5.1: Published structural results for two-dimensional rare earth silicides. Refer to Figure 4.1 for atomic labels. Techniques other than MEIS show a longer Si_2–RE bond length for a given rare earth. 103

Table 5.2: Bond lengths calculated from purely geometrical considerations (i.e. the measured angular position of the relevant blocking dip). Also shown for comparison are the published bond lengths. 107

Table 5.3: Revised structural parameters for 2D rare earth silicides and the corresponding subjective "by eye" fits. A general trend for a decrease in the Si_2–RE bond length with increasing atomic number emerges..................108

Table 5.4: Vertical separations between the Si_1 and RE atoms as found in the original published results, from a revised study of the data and from fitting by eye. The by eye results show that it is possible to subjectively fit blocking dips of this form. 109

Table 5.5: Comparison of the best fit models derived from comparing simulated and experimental blocking curves using a variety of R-factors. Also shown are the best subjective visual fits ("By Eye"). A trend in the Si_2–RE bond length is apparent in the results from a number of comparison methods; notably the "by eye" comparison, R_{min}, R_{Pflip} and R_{χ}-refined. 115

Table 6.1: Structural parameters for the final model. See Figure 6.7 for labels.136

Acknowledgements

It is with pleasure that I may take this opportunity to thank those who have been of immeasurable help during the course of this work. There are inevitably far too many to fully list but some are deserving of particular mention:

Firstly I must deeply thank my supervisor, Dr. Steve Tear, for his unending patience, wisdom, encouragement and guidance during my research. Undoubtedly this work would not exist but for his expert help.

I must also thank Dr. Paul Bailey and Dr. Tim Noakes of the Daresbury MEIS laboratory for their guidance and assistance in the work performed there.

Members of the University of York Surface Physics Group, both past and present, have always been available to suggest new ideas, offer encouragement and generally share the experience of working as part of an experimental physics group. I am grateful for all they have offered and hope I contributed in return.

In a similar vein the running of a successful laboratory relies on its technical support and I could not have hoped for better than Dave Coulthard, Richard Armitage, Pete Durkin and the rest of the Physics Department’s excellent technical staff.

On a final personal note, none of this would have been possible without Rachel. She has been my strength and beacon of light through darkness, for which I am reduced to a simple, inadequate, thank you.

Declaration

The work presented in this thesis is that of the author except where the contributions of others have been acknowledged explicitly in the text or by means of references. No part of this work has been presented for any other qualification at this or at any other university.

Publications

Growth and electronic structure of holmium silicides by STM and STS, E.W. Perkins, I. M. Scott and S. P. Tear, *Surface Science* **578** 80 (2005)

Chapter 1
Introduction

1.1 The Surface

The surfaces of solids are unique and unusual. When a surface is formed, the order present within the bulk of the solid is suddenly and dramatically broken. The removal of symmetry in one dimension results in a high number of dangling bonds and free energy. Not surprisingly the minimisation of this free energy often induces a change within the near surface region. This change may be a simple relaxation—in which the spacing of the top few atomic layers changes whilst maintaining the 2D periodicity—or, more radically and usually the case for semiconductors, a reconstruction producing a new 2D unit cell at the surface. These two possibilities are represented in a much simplified manner in Figure 1.1. Although such a reconstruction can strain the lattice this is more than compensated for in the reduction of the free energy derived from the associated removal of the dangling bonds. The changes at the surface of a material mean that the surface may have greatly different properties to the bulk. The technological importance of surfaces cannot be overstated. Examples of areas where the surface plays a main and vital role include the interaction of metals with semiconductors, catalytic reactions, the growth of crystals, and a myriad of others [1-7].

Despite the rearrangement of the surface to reduce the free energy, many surfaces remain unstable and readily react. This results in the potential for even small amounts of contamination interfering with the interface under investigation. Of course, even without this aspect, in order to study surfaces in their pristine condition then it is necessary to control the environment in which they are prepared and studied. At atmospheric pressure a surface is effectively instantly covered in many layers of adsorbates. Even at a pressure of around

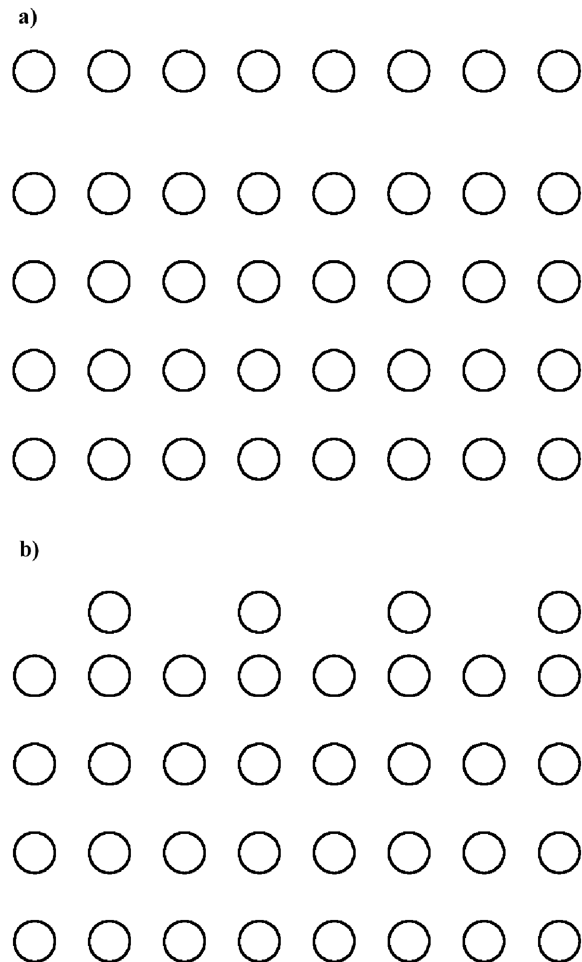

Figure 1.1: Simplified side view of a) a surface relaxation in which the atomic spacing changes near to the surface; b) a surface reconstruction, in which the atomic arrangement reconfigures to produce a new two-dimensional unit cell.

10^{-6} mbar it only takes around one second for one ML of gas molecules to cover the surface. It is necessary to reduce the pressure to the UHV regime of pressures less then 10^{-9} mbar to study surfaces. This increases the time for which the surface remains "clean" to the order of a few hours allowing experiments and analysis to be performed.

The changes at the surface of a material mean that the surface may have greatly different properties to the bulk. Not only is the structure different but the electronic and magnetic properties are also likely to differ. In the case of semiconductors the surface can cause electronic states to appear within the band

gap, with wavefunctions localised perpendicular to the surface. These surface states can have important implications for the interaction of the surface with overlayers grown on it.

1.2 Techniques of Surface Science

A wide and varied range of techniques have been developed to aid in the studies of surfaces and the near surface region. The range of available instrumentation is ever increasing. Some techniques, such as LEED, have been successfully used for decades. Others, such as STM, have come to define the more modern era of surface science. Yet other techniques such as RBS owe much to the original experiments and ideas that led to an understanding of the atomic nature of matter.

The surface sensitivity required of these techniques is achieved in a variety of ways. Chemical sensitivity to some element known to be present only at the surface gives an obvious method. Some techniques rely upon geometry, either of the experimental arrangement—such as in RHEED or SXRD—or of the crystal under study, such as in MEIS. Various spectroscopy techniques rely upon the small escape depth of electrons to ensure sensitivity only to the surface region. Other techniques, such as STM, may probe only the surface by their very nature.

In isolation, each technique can reveal much, but surface science often relies on the interplay between numerous experimental methods. Some techniques have become almost standard for surface science, such as LEED, STM, and AES. Others are less common, such as UPS and EELS. Still others are limited by their need for large experimental facilities, such as SXRD, MEIS and more. Many excellent references have been written on surface science techniques and the field in general. See for example Woodruff & Delchar [3], Prutton [1], Zangwill [4].

1.2.1 Scanning Tunnelling Microscopy

The STM has risen to great prominence since its invention in the early 1980s [8-11]. The power of the STM lies in its ability to give direct, real space information about the surface on the atomic scale [12-14]. STM involves bringing a very fine metallic probe tip into almost contact with the conducting surface of interest. The appliance of a bias voltage between the tip and surface results in a measurable tunnelling current which depends on the separation between the two. More details of STM may be found in the next chapter. Often the information from STM relates directly to the surface structure. It is necessary to be cautious in the interpretation of STM images, however, as electronic effects can play a large or dominating role. At times this can make STM images difficult to interpret or even misleading. However, the electronic nature of STM can also be harnessed to provide further information. By examining the variation of the tunnelling current with bias voltage—a technique known as scanning tunnelling spectroscopy—the surface electronic structure may be studied. This is especially useful if a normal STM image is acquired at the same time such that each point at which STS data is taken can be related to an atomically resolved surface feature.

STM is also restricted to non-insulator surfaces. This has led to the development of a number of related techniques such as AFM [11, 15, 16] where the tunnelling current of STM is replaced with the van der Waals interaction between a probe tip and the surface (this is normally detected by measuring the deflection of a cantilever on which the probe tip is mounted), and other derivatives. STM and STS are further discussed in Section 2.2.

1.2.2 Low Energy Electron Diffraction

LEED has become a mainstay of the surface science laboratory. In this technique a collimated beam of electrons with energy in the region of around 20–300 eV falls onto the surface. At this energy the de Broglie wavelength of the electrons is comparable to the atomic spacing within the crystal and diffraction occurs. The diffraction pattern formed consists of a pattern of spots which contract toward the

specular spot as the beam energy increases. As the scattering cross-section of the electrons is high and the mean free path small within the energy range involved, the technique is surface sensitive. The LEED pattern gives information about the reconstruction of the surface (see Section 2.3 for details). The spacing between the spots (as a function of beam energy) is inversely related to the 2D lattice spacing. Also, the symmetry of the LEED pattern reveals the symmetry of the surface. LEED has the power that it may act as a quick diagnostic tool to reveal to some extent the cleanliness of a surface (as the surface sensitive nature ensures that even a small layer of contamination degrades the LEED pattern) and any surface reconstruction before using another technique. This, and the fact that it is a fairly simple task to set up LEED equipment in any well equipped surface science laboratory, have led to LEED being one of the most widely used techniques; it is rare indeed to find a piece of surface science apparatus not equipped with a basic LEED.

The disadvantage of LEED lies mainly in that it gives little immediate information about the position (or types) of the atoms within the unit cell. For instance different atom configurations which share the same periodicity will give rise to superficially the same LEED pattern. LEED may be used as a quantitative crystallographic method but this is more complicated [17]. The high scattering cross-section means that multiple elastic scattering events contribute to the scattered beams, and a simple kinematic scattering theory fails. The use of LEED in a quantitative manner requires careful and painstaking measurement of the variation of the intensity of the LEED spots as a function of incident electron energy, to produce so called I(V) curves. This must then be followed by further time consuming computer simulations of the I(V) curves resulting from a number of trial structures. Comparison between experiment and simulation then proceeds in an interactive process. This of course assumes that some starting trial structure can be arrived at first. LEED is further discussed in Section 2.3.

1.2.3 *Reflection High Energy Electron Diffraction*

In RHEED a beam of electrons with energy typically in the range 10–100 keV is made to fall on the surface at a very grazing angle. Diffraction streaks are then observed on a fluorescent screen much as spots are for LEED (though there is no need for the screen to be raised to high voltage nor to screen secondary electrons as the energy of the diffracted electrons is already sufficient to cause florescence much higher than the background). The spacing of these streaks can reveal the lattice parameters. RHEED has the disadvantage that the scattering geometry must be changed, by rocking the sample or rotating about the surface normal, in order to obtain the full 2D diffraction pattern. It is also affected by the roughness of the surface. Due to the grazing angle small bumps in the surface can detract from the pattern, though this is often actually useful in determining the quality of the surface. RHEED is useful in that the RHEED pattern may be observed during sample preparation and the deposition of adsorbates. It therefore often forms a diagnostic tool in thin film growth.

1.2.4 *Medium Energy Ion Scattering*

MEIS is relatively lesser known technique. It offers surface and near surface sensitive structural information. Ions (usually H^+ or He^+) are accelerated to around 100 keV and focused onto the surface. Those scattered from the surface are detected over a range of angles and energies. In this way MEIS is an enhancement of RBS and is related to the techniques of HEIS in which the ions are of much higher energy (about 2 MeV) and somewhat less so to LEIS which involves energies of only a few keV. MEIS has advantages over techniques such as LEED in that it supplies easily interpreted real space information and can distinguish mass separated elements. It is not however overly sensitive to lighter elements. Structural analysis still requires computer simulation and MEIS also has the disadvantage of requiring a dedicated ion source at a large scientific facility. A further discussion of MEIS may be found in Chapter 3.

1.2.5 Surface X-Ray Diffraction

As is the case in RHEED, SXRD employs a grazing incidence and exit geometry. A 2D lattice of rods is produced, observed by rotating the sample about the surface normal until the detector cuts each rod. By then observing the change in intensity of the rod as the exit angle is varied the out of plane atomic displacements can be determined. Although the technique can give superior angular resolution than electron diffraction the intensities of the diffracted beam can be much smaller. The intensity of X-ray therefore needed for SXRD restricts its use to synchrotron radiation sources.

1.2.6 X-Ray Photoelectron Spectroscopy

X-rays are made to fall on the surface, ionising an electronic shell and ejecting a photoelectron. The energy of the photoelectron is given by

$$E_k = h\nu - E_B - \Phi \tag{1.1}$$

where $h\nu$ is the energy of the incident X-ray and E_B is the initial binding energy of the electron, and Φ is the work function of the surface. XPS is therefore a chemically sensitive probe of the surface. Further the energy resolution is high enough to detect the small shifts in energy due to the chemical state of the atom.

1.2.7 Ultraviolet Photoelectron Spectroscopy

UPS is related to XPS. In the case of UPS though the incident photons are not sufficiently energetic to ionise core level electrons and so this technique is a probe of the valence states. UPS is commonly used in investigating the surface band structure. By looking at the angles at which the photoelectrons are produced, a technique known as angle resolved UPS, the initial **k** state of the electrons may be found and a band map drawn. The interpretation of UPS spectra is somewhat complicated. The mean free path for electron–electron scattering varies rapidly at low kinetic energies and electrons from closer to the Fermi energy have a smaller mean free path than those from the bottom of the

conduction band. Also if an electron is ejected with low kinetic energy the probability of photoemission is affected by the density of states available to the photoelectron.

1.2.8 Auger Electron Spectroscopy

Like UPS and XPS, AES involves analysing the energy of emitted electrons. A beam of high energy (typically in the region of 3–5 keV) electrons is caused to fall on the surface. The incident electron may remove a core level electron from the atom, leaving the atom in a highly excited state. The atom may then relax via the transition of a second electron from a less tightly bound shell to fill the core level hole. The energy liberated by this transition ejects a third, Auger electron, which is then detected.

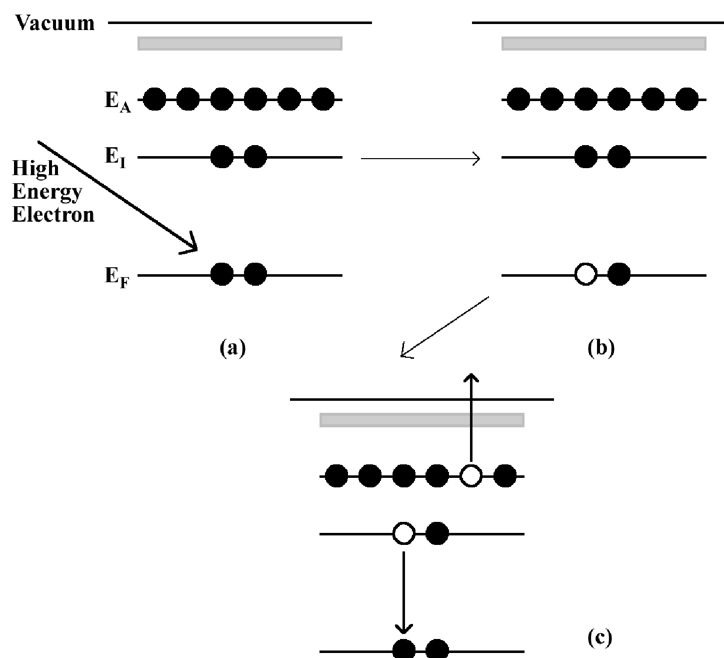

Figure 1.2: The Auger process. A high energy electron removes a core level electron from the atom (a), leaving an excited state (b). The atom relaxes via a less tightly bond electron filling the core level hole. The energy liberated causes the ejection of a third, Auger electron (c).

The process is illustrated in Figure 1.2. The kinetic energy of the Auger electron is given by

$$E_{KE} = E_F - E_I - E_A \qquad (1.2)$$

where E_I is the initial energy of the electron filling the core hole, E_F is the final energy of this electron and E_A is the binding energy of the Auger electron. Note that the final energy of the Auger electron is therefore independent of the incident electron beam (indeed sometimes X-rays may be used to initiate the same process; AES lines are present in XPS spectra).

The initial ionisation of a core level electron is non-selective and may be in various shells. There are also then a number of different electrons which may fill the resultant core level hole. This number of possible Auger transitions results in a characteristic spectrum of peaks at various energies of the ejected Auger electron. AES is hence chemically sensitive.

AES has the advantage that it is fairly simple to perform. Standard LEED optics may be adapted to act as an electron energy analyser in use with AES. The technique is very sensitive to small coverages and gives a useful indication of the cleanliness of a surface. It is a complex technique to use in a fully quantitative manner however. By focussing the electron beam and sweeping it across the surface, spatially resolved AES can be achieved (this is known as a scanning Auger microscope).

1.2.9 Electron Energy Loss Spectroscopy

A beam of monoenergetic electrons is scattered from the surface and the energies of the scattered electrons analysed. There will be specific energy losses due to the excitation of particular processes within the solid. These losses will appear as peaks at a fixed energy from the primary energy. The largest features are normally due to surface and bulk plasmon losses but it is possible to detect losses due to other processes, including the excitation and ionisation of core level

electrons in the solid (which gives an elemental identification). High resolution EELS allows the detection of the losses due to the vibrational states of absorbed molecules, which can be used to identify those molecules.

1.2.10 Surface Extended X-ray Fine Structure

If the absorption coefficient of a beam of X-rays transmitted through a solid is plotted as a function of incident X-ray energy then fine structure is observed. Absorption edges occur when the X-rays reach sufficient energy to excite a new core level. At energies above these edges the absorption coefficient is seen to oscillate–the extended X-ray fine structure. These oscillations are due to photoelectrons excited by the X-rays. The photoelectrons are backscattered by the neighbouring atoms and then interfere with the outgoing photoelectron wave. A constructive interference causes an increase in the X-ray absorption coefficient while a destructive interference causes a corresponding decrease in the absorption coefficient. As the energy of the incident X-rays changes so the energy of the photoelectrons, and hence their wavelength, changes. The interference moves from constructive to destructive to constructive, causing the observed ripple in the absorption coefficient.

If there is an atomic species on the surface (and only the surface) then it may be studied by tuning to the relevant, atom specific absorption edge. If this is not the case then surface sensitivity must be gained by indirectly observing EXAFS oscillations. The X-ray absorption is linked to the formation of core holes so a process reliant on this formation may be used to probe the absorption coefficient. For instance the yield of Auger electrons will vary in a way related to the absorption coefficient. The small escape depth of these electrons then gives surface sensitivity and the technique is known as surface EXAFS. SEXAFS has the disadvantage that a bright, monochromatic X-ray source such as that produced by monochromated synchrotron radiation is needed. It does give information on the chemical environment of the absorber, including the bond lengths and coordination number.

1.3 Metal–Semiconductor Interfaces

The metal–semiconductor interface is of interest both from a fundamental science perspective and in terms of technological importance [18-20]. Not only is the interface the initial contact to the semiconductor device but its electronic properties are important within the device.

When a metal and semiconductor are brought into contact charge flows between the two in order to equalise the Fermi levels. In the case of an *n*-type semiconductor the contact is Ohmic if the metal workfunction, φ_m, is less than the semiconductor workfunction, φ_s. If $\varphi_m > \varphi_s$ then the contact is rectifying, with a "Schottky" barrier height given by

$$\Phi_{SB} = \varphi_m - \chi \tag{1.3}$$

where χ is the semiconductor electron affinity. This situation is illustrated in Figure 1.3.

Unfortunately, this simplistic description rarely applies to the experimental results [21]. The above model assumes that during the interface formation the local semiconductor band structure is free to move with respect to E_f since the Fermi level is within the band gap (which lacks electronic states). The presence of surface states within the band gap of the semiconductor "pins" the Fermi level so that it is no longer free to move. This results in Equation 1.3 no longer being valid. Indeed, if the Fermi level is pinned then

$$\Phi_{SB} = E_c - E_f \tag{1.4}$$

and the barrier may be independent of the metal involved.

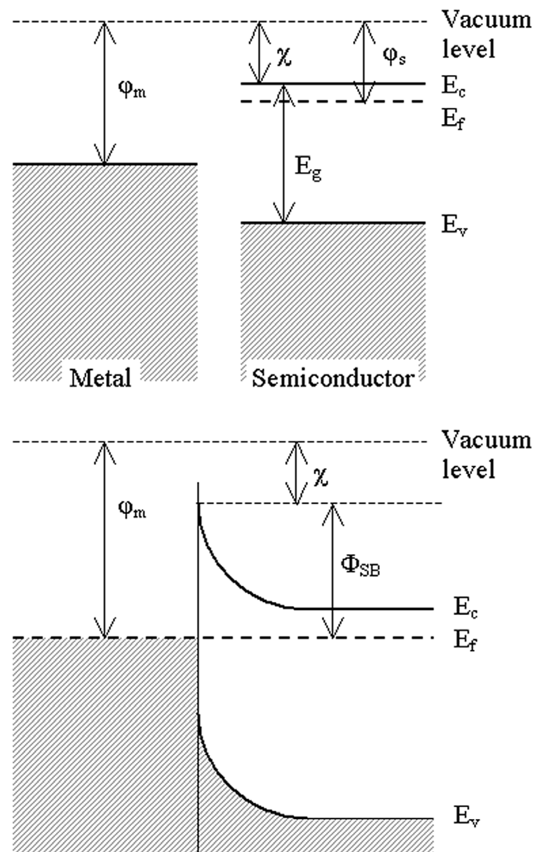

Figure 1.3: Formation of a Schottky barrier, Φ_{SB}, for an n-type semiconductor in contact with a metal. The Schottky barrier forms, and the junction is rectifying, if the metal wor function, φ_m, is greater than the semiconductor workfunction, φ_s. E_v is the top of the valence band, E_c the bottom of the conduction band and E_f the Fermi level. The band gap of the semiconductor, E_g is also indicated.

Driven by technological uses the investigation of metal–semiconductor interfaces has been intense. The formation and epitaxial growth of metal silicides on semiconductor surfaces offers potential technological benefits and growth on the group IV semiconductors, and Si in particular, offers easy integration with current technology [22-24].

In practice the interface of metal and semiconductor is a complex region affected by the interplay of chemistry, disorder, defects and other factors [25]. Clearly it is important to have an atomistic understanding in the low coverage regime in order to fully understand the growth processes involved. Investigation of the low

coverage regime gives insight into the amount of intermixing of the surface semiconductor and the metal, as well as the abruptness of the interface. Exact atomic arrangement also becomes increasingly important as the drive towards miniaturisation and nanotechnology continues.

1.4 Materials Studied

1.4.1 Two Dimensional Rare Earth Silicides

The growth of RE metals on Si has, over the past few years, attracted much attention. REs have been found to form a number of novel structures on Si, depending on the substrate orientation and preparation conditions. Monolayer coverages of RE have been shown to form self ordered nanowire arrays on Si(100) [26-30]. On the Si(111) surface perhaps the most interesting structure found is the much studied “two-dimensional” silicide formed by the trivalent RE metals.

Two-dimensional RE silicides are formed when one monolayer of RE is deposited onto the clean 7 × 7 reconstruction of Si(111) and subsequently annealed to around 500 ºC (see for example Ming *et al.* [31], Spence *et al.*, [32], Kitayama *et al.* [33]). The anneal causes a reconstruction of the surface layers. A 1 × 1 LEED pattern is observed after the formation of such a silicide. A single atomic layer of RE metal is located above the substrate in so called T4, three fold hollow sites. The silicide is terminated by a bulk like bilayer of Si, the orientation of which is rotated by 180º with respect to the bulk substrate orientation, Figure 1.4. This form of silicide has been shown to occur for most of the trivalent REs and may have useful technological applications. Unusually low Schottky barrier heights of 0.2–0.3 eV on *n*-type Si have been recorded for the silicon–RE silicide interface [34-38]. Further study is required to fully understand these interesting structures, both in terms of their electronic properties and as a possible novel growth template.

Original in colour

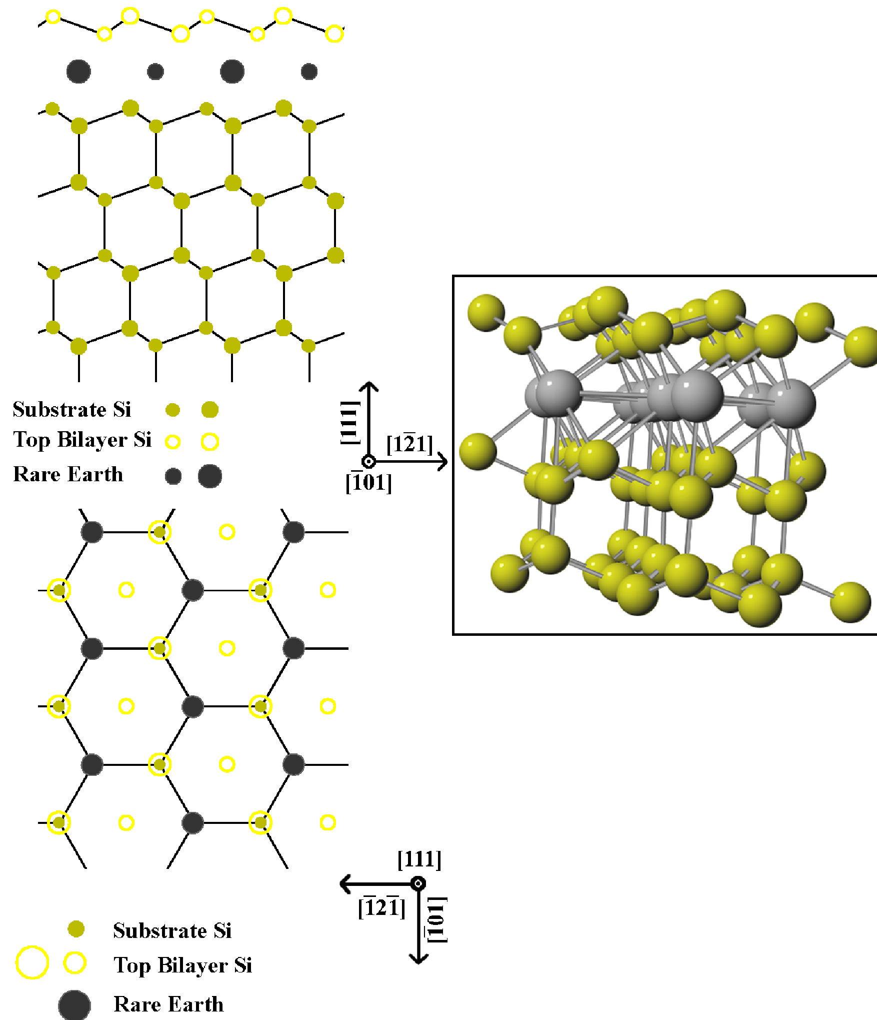

Figure 1.4: Structure of the 2D RE silicides. The RE forms a single atomic layer situated in T4 sites above the bulk Si. The silicide is terminated by a bulk-like Si bilayer, rotated by 180° with respect to the bulk. Top: Side view. Bottom: Top view (i.e. along the surface normal). Inset: Ball and stick model of the surface.

The large mass separation between RE and Si makes this an ideal system for MEIS study. The structure is made even more ideal by the heavy RE residing beneath the top Si bilayer. Analysing the MEIS signal from the RE allows a simple determination of the positions of the atoms within this bilayer. A MEIS analysis of the Tm 2D silicide is described in Chapter 4. A more general discussion of MEIS studies of all these 2D silicides is presented in Chapter 5.

MEIS does not reveal any information about the less well understood electronic nature of this interface. Here STM and in particular STS can produce atomically resolved electronic data. STS data obtained from the Ho 2D silicide is presented and discussed in Chapter 7.

1.4.2 Iron Silicides

The growth of Fe on Si has been studied for many years and with a wide variety of techniques [39-43]. Its study has risen in prominence again in recent years with the advent of spin electronics ("spintronics") [44, 45] and the possible role of Fe in spin injection into the semiconductor substrate [46]. The β-phase has attracted particular attention due to its semiconducting properties and good lattice match with Si (+2 % for CsCl structure [47]). The phase diagram for Fe coverage and anneal temperature is however complex [48] and little is known of the exact atomic configuration of some phases. In order to understand such complex systems it is useful to study the initial growth of the metal on the clean Si(111) 7×7 surface, in the monolayer (ML) coverage regime.

At monolayer coverage it is known that a 1×1 LEED pattern may be formed after a moderate anneal. This evolves to a 2×2 pattern after a higher temperature anneal [49]. It is thought from ISS [50] and STM [51] experiments that the 2×2 reconstruction is due to Si adatoms. The complete structure of this phase, and the 1 x 1 phase, is unknown. The differing masses of Si and Fe allow the elements to be resolved in a MEIS experiment. As MEIS is a powerful quantitative structural technique a structural determination for both the 1×1 and 2×2 phases may be

presented. They are found to be very similar, with the 2 × 2 indeed caused by a ¼ ML of Si adatoms, as discussed in Chapter 6.

1.4.3 Metal Growth on 2D Rare Earth Silicides

As mentioned above, the novel Si bilayer termination of the 2D RE silicides may form an interesting growth template. It is an intriguing possibility that the presence of the single atomic layer of rare earth immediately beneath this bilayer may act as a barrier to diffusion of metal overlayers into the bulk. The growth of Fe silicides particularly suffers from interdiffusion of the Si and Fe causing a rough interface. Chapter 7 shows an initial investigation of Fe growth on Ho 2D silicide. MEIS offers a valuable tool for studying this system as all three elements are well separated in mass and the signal from each may be independently considered. MEIS also offers a simple to interpret indication of the quality of the interface in an initial investigation.

References

1. M. Prutton, *Introduction to Surface Physics*, Oxford University Press (1994)

2. D. A. King and D. P. Woodruff, eds. *The Chemical Physics of Solid Surfaces and Heterogenous Catalysis*. , Elsevier Scientific Publishing: Amsterdam.(1993)

3. D. P. Woodruff and T. A. Delchar, *Modern Techniques of Surface Science*, Cambridge University Press (1986)

4. A. Zangwill, *Physics at Surfaces*, Cambridge University Press (1988)

5. R. A. Stradling and P. Klipstein, eds. *Growth and Characterisation of Semiconductors*. , Hilger: Bristol.(1990)

6. G. Attard and C. Barnes, *Surfaces*, Oxford University Press (1998)

7. J. B. Hudson, *Surface Science: An Introduction*, Butterworth-Heinemann (1992)

8. G. Binnig, H. Rohrer, Ch. Gerber and E. Weibel, *Phys. Rev. Lett.* **50** 120 (1983)

9. G. Binnig and H. Rohrer, *Surf. Sci.* **126** 236 (1983)

10. H. -J. Guntherodt and R. Wiesendanger, eds. *Scanning Tunneling Microscopy.* , Springer-Verlag: Berlin.(1992)

11. R. Wiesendanger, *Scanning probe microscopy and spectroscopy : methods and applications*, Cambridge University Press 637 (1994)

12. Ph. Avouris and I. -W. Lyo, *Studying surface chemistry atom-by-atom using the scanning tunneling microscope*, in *Chemistry and Physics of Solid Surfaces*, p. 371, Springer-Verlag: Berlin (1990)

13. N. D. Lang, *Phys. Rev. B* **34** 5947 (1986)

14. W. D. Schneider, *Surf. Sci.* **514** 74 (2002)

15. S. F. Alvarado, *Surf. Rev. Lett.* **2** 607 (1995)

16. G. Binning, C. F. Quate and Ch. Gerber, *Phys. Rev. Lett.* **56** 930 (1986)

17. J. B. Pendry, *Low Energy Electron Diffraction: The Theory and Its Application to Determination of Surface Structure*, Academic Press (1974)

18. S. P. Muraka, *Silicides for VLSI Applications*, Academic Press (1983)

19. H. von Känel, *Mater. Sci. Rep.* **8** 193 (1992)

20. J. Derrien, J. Chevrier, V. Le Thanh, T. E. Crumbaker, J. Y. Natoli and I. Berbezier, *Appl. Surf. Sci.* **70/71** 546 (1993)

21. G. Margaritondo, *Rep. Prog. Phys.* **62** 765 (1999)

22. A. H. Reader, A. H. van Ommen, P. J. W. Weijs, R. A. M. Wolters and D. J. Oostra, *Rep. Prog. Phys.* **56** 1397 (1993)

23. F. M. d'Heurle, *J. Electron. Mater.* **27** 1138 (1998)

24. S. P. Murarka, *Intermetallics* **3** 173 (1995)

25. E. H. Rhoderick and R. H. Williams, *Metal-Semiconductor Contacts*, Oxford Science Publications (1988)

26. C. Ohbuchi and J. Nogami, *Phys. Rev. B* **66** 165323 (2002)

27. J. Yang, Q. Cai, X. -D. Wang and R. Koch, *Surf. Sci.* **526** 291 (2003)

28. Y. Chen, D. A. A. Ohlberg and R. Stanley Williams, *J. Appl. Phys.* **91** 3213 (2002)

29. C. Preinesberger, S. K. Becker, S. Vandré, T. Kalka and M. Dähne, *J. Appl. Phys.* **91** 1695 (2002)

30. R. Ragan, Y. Chen, D. A. A. Ohlberg, G. Medeiros-Ribeiro and R. Stanley Williams, *J. Cryst. Growth* **251** 657 (2003)

31. L. Ming, L. Grill, M. G. Ramsey, F. P. Netzer and J. A. D. Matthew, *Surf. Sci.* **375** 24 (1997)

32. D. J. Spence, S. P. Tear, T. C. Q. Noakes and P. Bailey, *Phys. Rev. B* **61** 5707 (2000)

33. H. Kitayama, S. P. Tear, D. J. Spence and T. Urano, *Surf. Sci.* **482-485** 1481 (2001)

34. K. N. Tu, R. D. Thompson and B. Y. Tsaur, *Appl. Phys. Lett.* **38** 626 (1981)

35. H. Norde, J. de Sousa Pires, F. Pesavento F. d'Heurle, S. Petersson and P. A. Tove, *Appl. Phys. Lett.* **38** 865 (1981)

36. M. H. Tuilier, G. Gewinner, C. Pirri, P. Wetzel, D. Bomont and O. Heckmann, *J. Phys. IV* **4** 187 (1994)

37. S. Vandré, T. Kalka, C. Preinesberger and M. Dähne-Prietsch, *Phys. Rev. Lett.* **82** 1927 (1999)

38. S. Vandré, T. Kalka, C. Preinesberger and M. Dähne-Prietsch, *J. Vac. Sci. Technol. B* **17** 1682 (1999)

39. J. de la Figuera, A. L. V. De Parga, J. Alverez, J. Ibanez, C. Ocal and R. Miranda, *Surf. Sci.* **264** 45 (1992)

40. W. Raunau, H. Niehus, T. Schilling and G. Comsa, *Surf. Sci.* **286** 203 (1993)

41. A. L. V. De Parga, J. de la Figuera, C. Ocal and R. Miranda, *Ultramicroscopy* **42-44** 845 (1992)

42. T. Ehara, S. Nakagomi and Y. Kokubun, *Solid-State Electron.* **47** 353 (2003)

43. H. T. Lu, L. J. Chen, Y. L. Chueh and L. J. Chou, *J. Appl. Phys.* **93** 1468 (2003)

44. G. A. Prinz, *Science* **282** 1660 (1998)

45. M. Oestreich, *Nature* **402** 735 (1999)

46. H. J. Zhu, M. Ramsteiner, H. Kostial, M. Wassermeier, H. -P. Schönherr and K. H. Ploog, *Phys. Rev. Lett.* **87** 016601 (2001)

47. K. A. Mäder, H. von Känel and A. Baldereschi, *Phys. Rev. B* **48** 4364 (1993)

48. H. von Kanel, N. Onda, H. Sirringhaus, E. Muller-Gubler, S. Goncalces-Conto and C. Schwarz, *Appl. Surf. Sci.* **70/71** 559 (1993)

49. U. Starke, W. Weiss, M. Kutschera, R. Bandorf and K. Heinz, *J. Appl. Phys.* **91** 6154 (2002)

50. U. Kafader, P. Wetzel, C. Pirri and G. Gewinner, *Appl. Surf. Sci.* **70/71** 573 (1993)

51. A. L. Vazquez de Parga, J. de la Figuera, C. Ocal and R. Miranda, *Europhys. Lett.* **18** 595 (1992)

Chapter 2
Experimental Aspects

2.1 The Daresbury MEIS Facility

All MEIS experiments in this work were performed at the Daresbury MEIS facility, located at the CCLRC Daresbury Laboratory, Warrington, UK [1, 2]. The facility is a relatively new laboratory originally developed as a collaboration between the Universities of Warwick and Salford to provide a resource to the UK surface science community. The facility was commissioned on 1st April 1996. A description of the technique of MEIS itself may be found in Chapter 3; this section describes the MEIS facility.

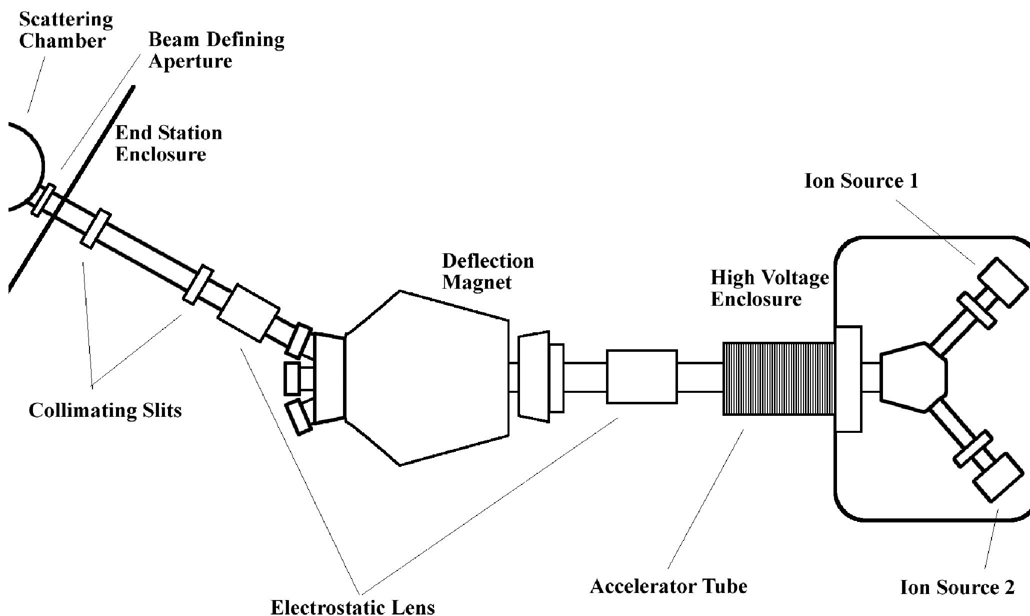

Figure 2.1: Schematic diagram of the Daresbury MEIS facility beam line. Ions are produced by a duoplasmatron source and accelerated to around 100 keV. The ion beam is then focused and collimated before entering the scattering chamber.

The Daresbury MEIS facility comprises an ion source, beam line and end user experimental station. The ion source is a hot-cathode duoplasmatron source and accelerator capable of operating at up to 400 keV, which were derived from the decommissioned Nuclear Structure Facility previously located at Daresbury. The ion source and accelerator are connected via the beam line to a user end station consisting of several interconnected UHV chambers. A schematic diagram of the ion source and beam line is shown in Figure 2.1. The collimating slits and beam defining aperture ensure a beam divergence of < 0.1 ° and size of 0.5 × 1.0 mm^2 (vertical × horizontal) at the sample. The ion source, beam line components and detector are all remotely computer controlled from within the end station.

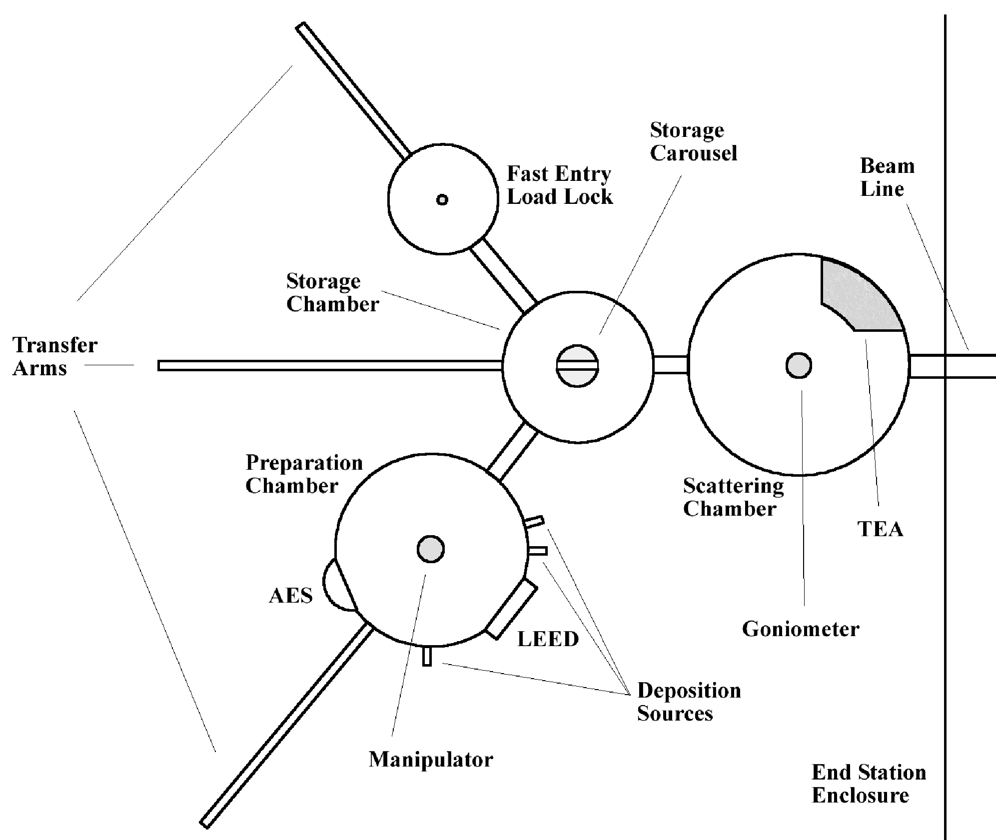

Figure 2.2: Schematic diagram of the Daresbury MEIS facility user end station. The ion beam enters at the main scattering chamber. Sample preparation is performed in a separate chamber and sample storage and fast entry is also available.

The end station itself consists of three UHV chambers and a fast entry load lock, connected by transfer arms to allow for free movement of samples. The chambers are isolated from one another by means of viton gate valves when sample transfer is not taking place. A schematic of the end station is shown in Figure 2.2. The load lock allows for a sample to be put into the UHV system within about 30 minutes. It also contains simple heating facilities to degas sample holders and samples in preparation for UHV compatibility. The sample storage chamber contains a rotating carousel capable of holding up to six samples. One of the storage positions on this carousel offers electron–beam sample heating. The base pressure of this chamber is around 3×10^{-10} mbar after bakeout, being pumped by a combination of a rotary backed turbomolecular pump and a TSP.

The sample preparation chamber operates at a base pressure of 1×10^{-10} mbar, being pumped in a similar manner to the storage chamber. The chamber is equipped with a sample manipulator offering lateral translation and sample rotation. The system offers a rear view LEED, AES, e^-–beam heating of samples, and the facility to Ar^+ ion bombard samples. A variety of deposition sources can also easily be attached to the chamber for sample preparation. Sample temperature may be monitored by means of an external infrared pyrometer.

The scattering chamber operates at a base pressure of 1×10^{-10} mbar. Like the other UHV chambers this is pumped by a combination of turbomolecular pump and TSP. The chamber is equipped with a goniometer (high precision manipulator) allowing three degrees of sample rotation to within 0.1˚, as well as XYZ-translation. Immediately the ion beam enters this chamber there is a beam monitor consisting of vertical strands, 50 μm diameter, of gold coated tungsten (shielded at −300 V to suppress secondary electron loss). This measures a fixed amount of the ion beam to give a measure of the current transmitted to the sample.

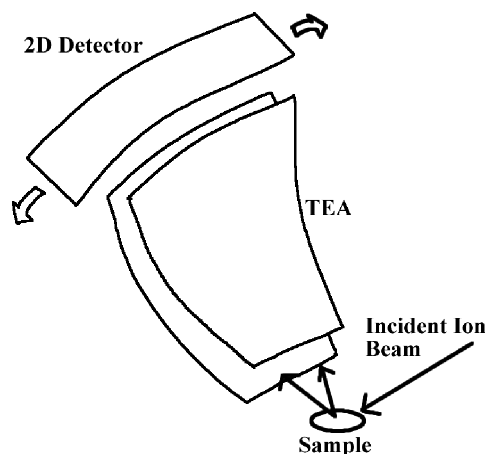

Figure 2.3: The torodial electrostatic analyser and 2D detector produce the 2D data sets in MEIS experiments. Ions entering the detector are bent through 90° before hitting a set of channel plates which amplify the charge so it may be detected by the 2D detector plate.

The scattering chamber also contains the TEA. This admits the scattered ions over a 27 ° window and an energy window of 2 % of the pass energy. The operation of the TEA is similar to a hemispherical analyser. The ions are electrostatically bent through 90 ° where they impinge upon a set of channel plates to produce an amplified charge which is detected by a position sensitive detector plate, hence producing the 2D map of scattered ions (Figure 2.3).

2.2 Scanning Tunnelling Microscopy

2.2.1 General Principle

STM was developed in the early 1980s, initially by G. Binnig and H. Rohrer [3, 4]. It has rapidly become one of the main—and most powerful—tools available to the surface scientist [5-10].

The scanning tunnelling microscope operates based on the phenomenon of quantum mechanical tunnelling of electrons [11-14]. From a quantum mechanical point of view the electrons may be described as wave functions and have a finite probability of tunnelling through a potential barrier in a classically

forbidden way. STM utilises this by bringing a metallic tip close (to within about 1 nm) to the surface of interest. If a bias voltage is then applied between tip and sample electrons are free to tunnel through the vacuum gap from the tip to the surface under investigation (or vice versa). This results in a tunnelling current (of the order of a few nanoamps)

$$I_T \propto V_T \exp(-A\Phi^{1/2}s) \qquad (2.1)$$

where Φ is the tunnelling barrier height and s the tunnelling barrier width.

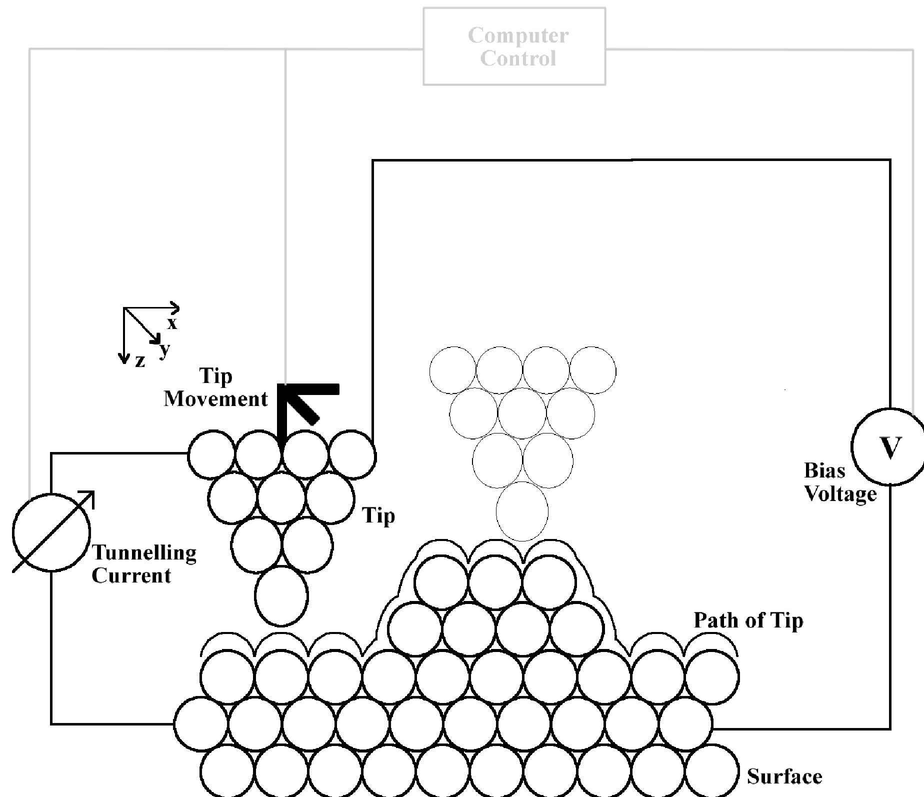

Figure 2.4: The general operation of the scanning tunnelling microscope in constant current mode. As the tip is scanned across the surface its z-position is adjusted to maintain a constant tunnelling current. This results in the tip following the contours of the surface.

The term A is given by

$$A = \left(\frac{4\pi}{h}\right)\sqrt{2m} = 1.025\ \text{Å}^{-1}\ \text{eV}^{-1/2} \qquad (2.2)$$

m being the free electron mass and h Plank's constant.

The barrier width is determined by the tip–sample separation and the barrier height by the work function. For a typical work function of a few electron volts a change in the barrier width (i.e. tip–sample separation) of about an Ångstrom produces an order of magnitude change in tunnelling current.

If the tunnelling current is monitored as the tip is scanned across the surface in a raster pattern this sensitivity of the tunnelling current to the tip–sample separation makes it possible to map out the surface topography. This mode of operation, in which the surface is mapped using the tunnelling current, is known as constant height mode. In fact it is more normal to maintain a constant tunnelling current by adjusting the tip "height", or z-position, in a feed back loop and use this position as a measure of the topography in producing a greyscale image as the tip is scanned across the surface. This mode of operation is known as constant current mode. Figure 2.4 schematically shows the principle of operation in this mode. While this mode of operation is not as fast as constant height mode it has the advantage that the tip follows the corrugation of the surface and so reduces the likelihood of tip crashes as the tip is able to move over large islands and step edges.

2.2.2 Theory

The theory of STM has been given by Tersoff and Hamann [13, 14]. Perturbation theory gives a first order for the tunnelling current given by

$$I = \frac{2\pi e}{\hbar} \sum_{\mu\nu} f(E_\mu)[1 - f(E_\nu + eV)] |M_{\mu\nu}|^2 \delta(E_\mu - E_\nu) \qquad (2.3)$$

where f(E) is the Fermi function, V the bias voltage, $M_{\mu\nu}$ is the tunnelling current matrix element between the states ψ_μ of the probe and ψ_ν of the surface and E_μ and E_ν are the energies of the states ψ_μ and ψ_ν respectively (in the absence of tunnelling).

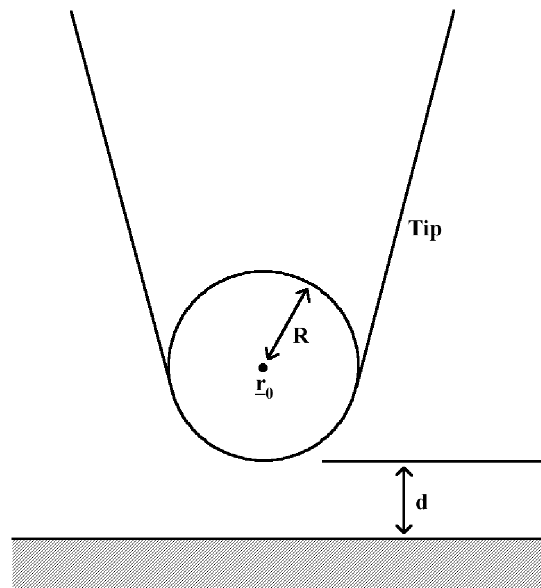

Figure 2.5: The model tip used in the calculations of Tersoff and Hamann [13, 14]. *The tip is taken as a spherical potential well of radius R, centred at* $\mathbf{r_0}$ *a distance d above the surface.*

In the limits of low temperature and voltage Equation 2.3 becomes

$$I = \frac{2\pi}{\hbar} e^2 V \sum_{\mu\nu} \left| M_{\mu\nu} \right|^2 \delta(E_\nu - E_F)\delta(E_\mu - E_F) \qquad (2.4)$$

E_F being the Fermi energy.

The probe tip was modelled as shown in Figure 2.5. The tip is taken to be a spherical potential well centred about $\mathbf{r_0}$ a distance d from the surface, with a radius of curvature R. By expanding the tunnelling matrix element as described by Bardeen [15] and writing the wave functions ψ in appropriate forms, Tersoff and Hamann were able to show that Equation 2.4 becomes

$$I = 32\pi^3 \hbar^{-1} e^2 V \varphi^2 D_t(E_F) R^2 k^{-4} e^{2kR} \sum \left| \psi_\nu(\mathbf{r_0}) \right|^2 \delta(E_\nu - E_F) \qquad (2.5)$$

Here D_t is the density of states per unit volume of the tip, φ is the work function (it is assumed the work functions of tip and sample are the same), and the term k is given by

$$k = \frac{(2m\varphi)^{1/2}}{\hbar} \qquad (2.6)$$

Equation 2.5 has important consequences. As $\left| \psi_\nu(\mathbf{r_0}) \right|^2 \propto e^{-2k(R+d)}$ the conductance σ is seen to be

$$\sigma \propto e^{-2kd} \qquad (2.7)$$

which reproduces the exponential dependence on tip–sample separation seen in Equation 2.1.

Although the theory developed by Tersoff and Hamann is useful it is too simplistic to describe some aspects of STM. For instance, the predicted lateral resolution of the STM is around 5–6 Å, which is clearly larger than can be

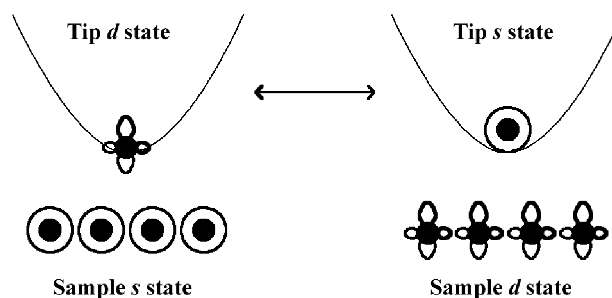

Figure 2.6: Qualitative description of the reciprocity principle. Probing surface s *states with a tip* d *state is equivalent to probing* d *states with a tip* s *state.*

achieved in practice. In order to explain this discrepancy, Chen developed a theory of the STM in which the electronic states of the probe tip were realistically considered [11, 12]. Chen showed that the resolution of the STM is due to *d* or *p* states of the probe tip. These states cause the increased resolution because of the "reciprocity principle" in STM: If the tip and sample states are interchanged then the image should be identical. The explanation is shown qualitatively in Figure 2.6. If there is a *d* state on the tip it traces not the charge density of the surface but that of a non-existent surface with a *d* state on each atom. It is this which allows higher resolutions than those predicted by theoryjust considering the *s* states. It is this effect which makes a metal such as W, a *d* band metal, an ideal material for STM probes.

It is interesting that the very reason the STM can achieve such very high lateral resolution is also one of the most important difficulties in STM. When considering the topography of a surface obtained by STM one must bear in mind that not only the surface but also the tip electronic structure plays a role. The image obtained is in realirty a convolution of the sample and tip electronic states. It is the change in the tip electronic structure when contaminates are picked up or lost that can cause an abrupt change in resolution during scanning. And on occasion it is possible that the images obtained have little relation with the surface under investigation and much more to do with the tip being used.

2.2.3 Scanning Tunnelling Spectroscopy

As electronic effects are so important in the tunnelling process, and the tunnelling current exhibits a bias voltage dependence, images taken at different biases may show striking differences. This is especially evident when considering STM images obtained when the sample is positively biased (in which case empty states of the sample are being imaged) compared to negatively biased (in which case filled states are imaged). It is this dependence that results, for instance, in the difference between STM images of the familiar Si(111) 7 × 7 reconstructed surface. In images obtained with negative sample bias one half of the reconstructed unit cell appears darker than the other; while for positive sample bias the two halves have approximately equal brightness (see for example Avouris *et al* [16], Tromp *et al.* [17], Figure 2.7).

Whilst some information may be gained by examining a surface under different bias conditions (most usually by scanning with one bias in the "forward" direction and then a different bias as the tip makes the return journey in the

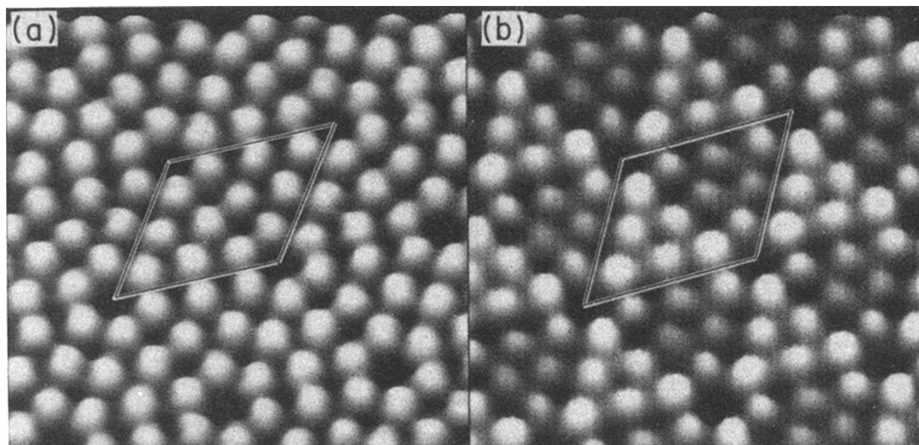

Figure 2.7: Bias condition dependence of STM imaging, in the case of the Si(111) 7×7 surface. (a) Unoccupied states with the sample biased at +1.5 V. (b) Occupied states with the sample biased at –1.5 V. The unit cell is marked in each case. Note that in the case of (b) a difference is clear between the faulted and unfaulted half of the unit cell, whilst in (a) the two halves appear the same. From Avouris & Wolkow [16].

"backward" direction) it is possible to extend the technique in a more quantitative manner. The technique of scanning tunnelling spectroscopy is one such way [7, 11, 18, 19]. In STS the tip is momentarily held stationary during the scan and the feedback loop adjusting the tip height is turned off. The tunnelling current is then measured as the bias voltage is ramped to give a plot of current versus voltage. By performing this procedure at every point on a normal STM scan (or at a grid of points) it is possible to gain spatially resolved spectroscopic information about the surface of interest. Of course due to the nature of the interaction it is important to be aware that the tip electronic structure may also influence STS data, just as it might an ordinary STM image.

2.2.4 Apparatus

The experiments reported in this work were performed using two STMs within the Surface Science Group at the University of York. Both are commercial instruments supplied by Omicron GmbH. The first is an Omicron STM 1. This STM is housed in an UHV side chamber attached to an UHV sample preparation chamber (Figure 2.8). The system is pumped by a rotary backed diffusion pump and a TSP with the base pressure after bakeout being around 1×10^{-10} mbar. The preparation chamber offers the standard surface science equipment such as a.rearview LEED capable of also performing AES, sample e^-–beam and direct current heating facilities, Ar^+ bombardment and the option to attach a variety of deposition sources. Samples may be transferred in vacu between the preparation chamber and the STM. There is also a storage carousel where up to eight samples may be held.

The STM tip is scanned across the sample surface by means a tripod arrangement of three piezoelectric tubes, one each controlling the x-, y- and z-motion. The sample itself is mounted on further piezoelectric legs running in tracks. By applying a skewed voltage pulse to these legs it is possible to move the sample in a slip–stick motion to facilitate controlled macroscopic approach to the tip. The scanning, bias voltage, etc are controlled by an interface to a HP-UX computer.

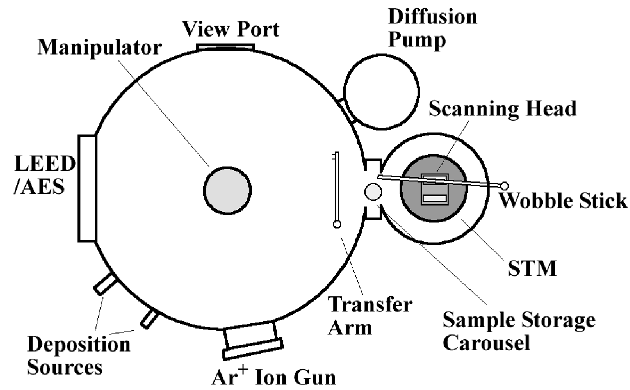

Figure 2.8: Schematic diagram of the STM 1 system. The STM is housed in a UHV side chamber attached to a UHV sample preparation chamber equipped with LEED, AES and deposition sources.

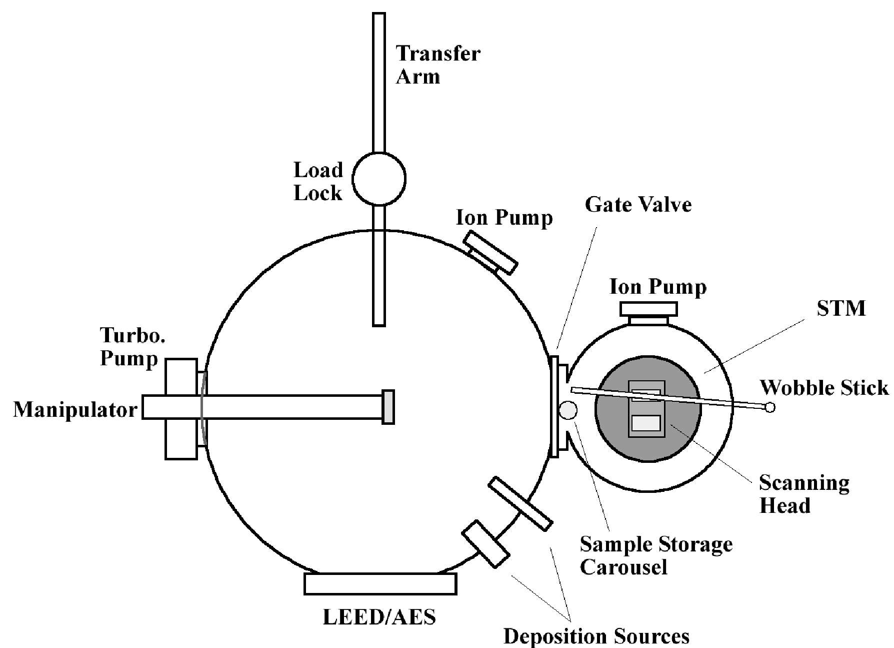

Figure 2.9: Schematic diagram of AFM/STM systems used. The UHV STM side chamber may be isolated from the main UHV sample preparation chamber. Samples may be quickly exchanged in and out of the system using a load lock

The entire UHV system is vibrationally isolated by mounting on three tyre inner tubes and housed within a purpose built hut in the laboratory, to ensure mechanical stability whilst the STM is in operation. The STM stage itself magnetically damped *in vacu* to further reduce vibrations.

The second instrument is a newer Omicron AFM/STM. It is also housed in an UHV side chamber attached to an UHV preparation chamber (Figure 2.9). The preparation chamber again offers LEED, AES, ion bombardment and sample heating. Samples may be transferred from the preparation chamber to the STM by means of a manipulator and wobble stick. The STM chamber may be isolated from the preparation chamber by means of a gate valve during sample preparation, as it is independently pumped by an ion pump. The main chamber is pumped by a combination of a second ion pump and a rotary backed turbomolecular pump. The base pressure achieved after bakeout is in the region of 1×10^{-10} mbar. The system also has a vacuum load lock to allow expedient sample entry and removal and a sample storage carousel within the STM chamber.

The AFM/STM is of a similar design to the STM 1 but with additional parts to facilitate AFM. The main difference between the two instruments is that where the STM 1 scanning is driven by three piezoelectric tubes, in the AFM/STM a single piezoelectric tube produces the motion in all three axis. Also it is the sample, rather than the tip itself, which is moved in the scanning process. The system is controlled by an interface to a PC. The system is again vibrationally isolated. Both the STM 1 instrument and the AFM/STM have routinely achieved atomic resolution of clean semiconductor surfaces.

2.3 Low Energy Electron Diffraction

One of the most widely used techniques in surface physics is that of LEED [20-22]. LEED, as the name suggests, involves the diffraction of electrons from the surface. A beam of electrons with energy in the region of ~20–300 eV is made to fall onto the sample normal to the surface. At this energy range the de Broglie

wavelength of the electrons is comparable with atomic spacings.

The basic principle underlying LEED may then be seen by considering the simple one dimensional case, Figure 2.10. With the electron beam normal to the one dimensional array there will occur constructive interference of backscattered electrons when the Bragg condition is met,

$$a \sin(\theta) = n\lambda \tag{2.8}$$

where θ is the backscattering angle, a the interatomic spacing, n an integer and λ is the electron wavelength given by

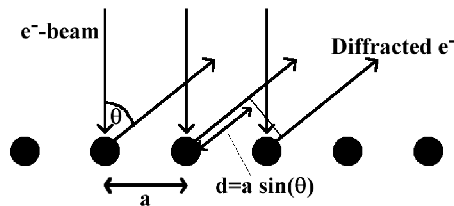

Figure 2.10: Simple diffraction in 1D. Constructive interference occurs when the Bragg condition is met, i.e. path difference d=nλ, λ being the electron wavelength and n=...-2,-1,0,1,2,3,...

$$\lambda = \frac{h}{(2m.e.V)^{1/2}} \tag{2.9}$$

Extending to two dimensions constructive interference will occur when both $n_a\lambda = a \sin(\theta_a)$ and $n_b\lambda = b \sin(\theta_b)$, a and b being the primitive interatomic spacings. This may be most clearly seen by considering the familiar Ewald sphere (Figure 2.11). In the 2D case each 2D lattice point is associated with a rod normal to the surface. The Bragg condition is met when $\mathbf{k_i} - \mathbf{k_s}$ is equal to a vector of the 2D reciprocal lattice, **g**, where $\mathbf{k_i}$ and $\mathbf{k_s}$ are the wave vectors of the incident and scattered electron, respectively. As can be seen from Figure 2.11 this occurs when the sphere crosses a reciprocal lattice rod.

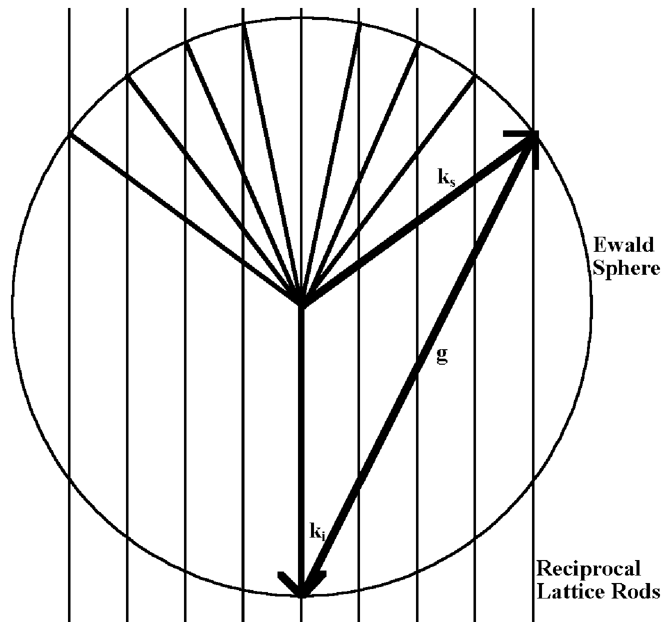

Figure 2.11: The Ewald sphere for elastic scattering in 2D. The bragg condition $\boldsymbol{k_i}-\boldsymbol{k_s}=\boldsymbol{g}$ *is met whenever the sphere crosses a reciprocal lattice rod.*

This results in set of rods in a two dimensional array. By observing across these rods a set of points is seen (see Figure 2.12 for an example). In two dimensions the LEED pattern is therefore an image of the surface reciprocal net.

The LEED pattern obtained reflects the surface atomic arrangement; the pattern of spots is dependent on the surface reconstruction present (if any) and the spacing between spots as a function of electron energy inversely relates to the real space atomic spacings. Determining atomic structure from LEED is far from straight forward. The electrons scatter from not only the first purely two dimensional layer but also deeper layers and also undergo multiple elastic scattering. The simple kinematic theory outlined above is therefore not sufficient to describe the scattering.

Original in colour

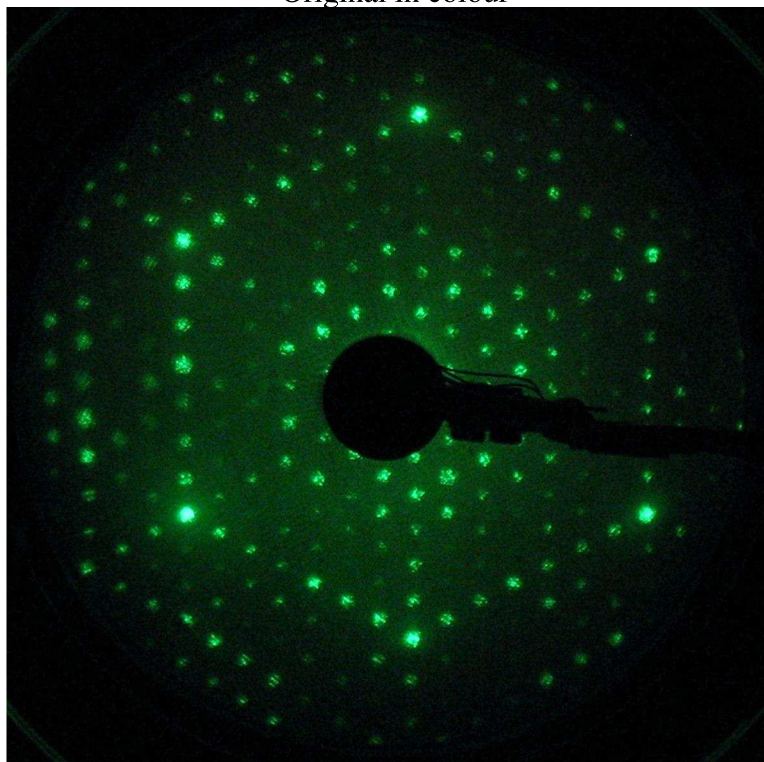

Figure 2.12: An example LEED pattern [24], showing the diffraction pattern from the clean Si (111) 7 × 7 surface with incident electron energy of 40 eV. Note that the periodicity of the surface is immediately apparent.

It is possible to use LEED in a more quantitative manner by observing the intensity of a spot as a function of the incident electron energy to give an I(V) curve [23]. Such a practice can allow the surface structure to be fully determined using LEED but the process is complicated and requires computer simulation of trial structures. It is much more usual to use LEED as a diagnostic tool to indicate the reconstruction and quality of a surface prior to the use of some other technique.

A typical LEED apparatus is shown schematically in Figure 2.13. The grids G1, G2 and G3 and the screen are concentric hemispheres centred around the sample. Diffracted beams are accelerated between the grid G1 and the screen in order to have enough energy to cause a fluorescence at the screen. The grids G2 and G3

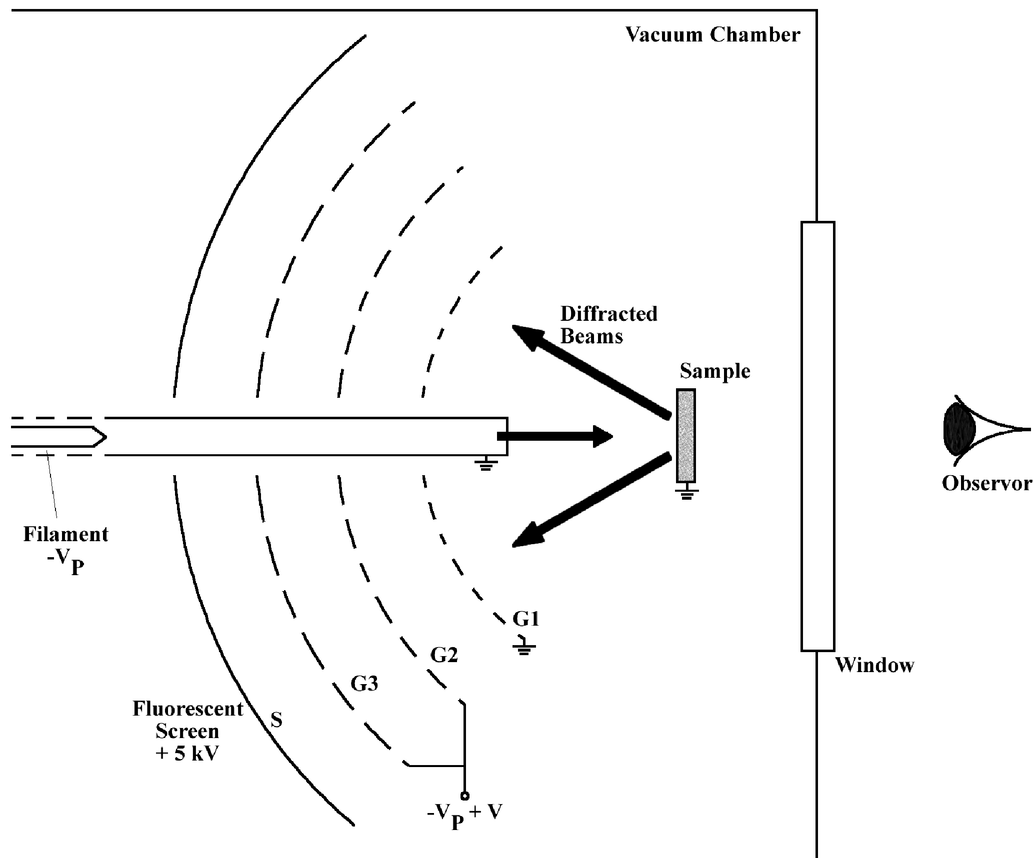

Figure 2.13: Typical LEED apparatus. Electrons are diffracted from the sample and accelerated between the grid G1 and the fluorescent screen. The grids G2 and G3 filter out the lower energy, inelastically scattered electrons to reduce the background. It is often the case that the fluorescent screen is deposited on a window so that the pattern may be viewed through the glass to avoid the problems with the screen being obscured by the sample mountings.

act to filter out the lower energy inelastically scattered electrons which would contribute nothing but a diffuse background to the LEED pattern. Often the fluorescent screen is deposited on a glass section allowing the diffraction pattern to be observed through the glass and screen in order to avoid the problems of the sample mounting arrangement obscuring the screen. This arrangement is known as a “reverse view” LEED.

References

1. P. Bailey, T. C. Q. Noakes and D. P. Woodruff, *Surf. Sci.* **426** 358 (1999)

2. D. Brown, T. C. Q. Noakes, D. P. Woodruff, P. Bailey and Y. Le Goaziou, *J. Phys. Condens. Matter* **11** 1889 (1999)

3. G. Binnig, H. Rohrer, Ch. Gerber and E. Weibel, *Phys. Rev. Lett.* **49** 57 (1982)

4. G. Binnig and H. Rohrer, *Surf. Sci.* **126** 236 (1983)

5. S. F. Alvarado, *Surf. Rev. Lett.* **2** 607 (1995)

6. P. A. Bennett and H. von Känel, *J. Phys. D: Appl. Phys.* **32** R71 (1999)

7. Ph. Avouris and I. -W. Lyo, *Studying surface chemistry atom-by-atom using the scanning tunneling microscope*, in *Chemistry and Physics of Solid Surfaces*, p. 371, Springer-Verlag: Berlin (1990)

8. R. J. Hamers, *STM on Semiconductors*, in *Scanning Tunneling Microscopy I*, H. J. Guntherodt & R. Wiesendanger, (Eds.) Springer-Verlag: Berlin (1992)

9. R. Wiesendanger, *Scanning probe microscopy and spectroscopy : methods and applications*, Cambridge University Press 637 (1994)

10. W. D. Schneider, *Surf. Sci.* **514** 74 (2002)

11. C. J. Chen, *J. Vac. Sci. Technol. A* **6** 319 (1988)

12. C. J. Chen, *Phys. Rev. Lett.* **65** 448 (1990)

13. J. Tersoff and D. R. Hamann, *Phys. Rev. B* **31** 805 (1985)

14. J. Tersoff and D. R. Hamann, *Phys. Rev. Lett.* **50** 1998 (1983)

15. J. Bardeen, *Phys. Rev. Lett.* **6** 57 (1961)

16. Ph. Avouris and R. Wolkow, *Phys. Rev. B* **39** 5091 (1989)

17. R. M. Tromp, R. J. Hamers and J. E. Demuth, *Phys. Rev. B* **34** 1388 (1986)

18. N. D. Lang, *Phys. Rev. B* **34** 5947 (1986)

19. S. P. Tear, *Scannning Probe Spectroscopies*, in *Spectroscopy for Surface Science*, p. 121, R. J. H. Clark & R. E. Hester, (Eds.) John Wiley & Sons (1998)

20. M. Prutton, *Introduction to Surface Physics*, Oxford University Press (1994)

21. D. P. Woodruff and T. A. Delchar, *Modern Techniques of Surface Science*, Cambridge University Press (1986)

22. A. Zangwill, *Physics at Surfaces*, Cambridge University Press (1988)

23. J. B. Pendry, *Low Energy Electron Diffraction: The Theory and Its Application to Determination of Surface Structure*, Academic Press (1974)

24. Courtesy of E. W. Perkins, *Unpublished* (2005)

Chapter 3
Medium Energy Ion Scattering

3.1 Introduction

Medium energy ion scattering is a refinement of the perhaps better known technique of Rutherford back scattering but offers improved energy and angular resolution [1-3]. This allows MEIS to achieve much higher depth resolution as well as forming an ideal tool for the study of surface and near surface structure. The technique has been successfully applied to a number of systems [4-18]. MEIS is closely related to the techniques of LEIS and HEIS [1, 3, 19, 20]. In all these techniques energetic ions (in the case of MEIS usually H^+, He^+ or Li^+) are made to impact the surface under investigation and the scattered ions are detected. MEIS has advantages over both LEIS and HEIS when applied to studies of surfaces. The energy of the ions involved (~100 – 500 keV) are lower than those of HEIS (which are typically ≥1 MeV). The main advantage of this is that the shadow cone radius (see below) is larger, and hence the technique is more surface sensitive. The lower energies also allow for improved energy resolution when detecting the scattered ions, which equates to better depth resolution. Despite these differences HEIS and MEIS are extremely similar, and the physics underlying one technique may be applied to the other. LEIS, on the other hand, employs ions of much lower energy (a few keV). LEIS suffers from neutralization effects of the incident ions. Also at such low energies the scattering potential is not well known, unlike the case in MEIS and HEIS. The low energy also makes the technique extremely surface sensitive, which may be advantageous but might also be a hindrance in the study of near surface buried interfaces. LEIS does have the further advantage that it does not require the dedicated facilities necessitated by MEIS and HEIS and can indeed be performed in a standard laboratory.

MEIS also has advantages over other techniques such as LEED, mainly that it produces data in real space. Also, as the scattering is kinematic, the data reflects real atomic positions, which is not necessarily the case with other real space imaging techniques such as STM. MEIS also has the advantage over STM in that it can provide information about relatively deep layers rather than just the surface or very near surface region. If the elements present are separated enough in terms of mass then the ions scattered from each can be resolved. This can greatly aid in the interpretation of the MEIS data as shall be seen in later chapters.

3.2 The Technique of MEIS

As the scattered ions have energies of around 100 keV their speed is much greater than that of the atom's movement due to crystal phonon vibrations, so the ions essentially see a frozen snapshot of the crystal. This allows the scattering to be considered as a sequence of kinematic scattering events between ion and crystal atomic nucleus [3, 19, 21].

3.2.1 Shadowing and Blocking

MEIS generally gains its surface sensitivity from the practice of "shadowing". The ionic beam is aligned along a major crystallographic direction (in practice the crystal is rotated about the beam). This shadows atoms deeper in the crystal, further along the "row", as shown in Figure 3.1.

The shadowed volume forms a cone, the radius of which increases with distance from the shadowing atom. For a Coulomb potential this radius is given by

$$R = 2\sqrt{\frac{Z_1 Z_2 e^2 l}{E}} \tag{3.1}$$

where Z_1 and Z_2 are the atomic numbers of ion and target, E is the ion energy and l is the distance from the atom. While equation 3.1 gives an estimate of the size

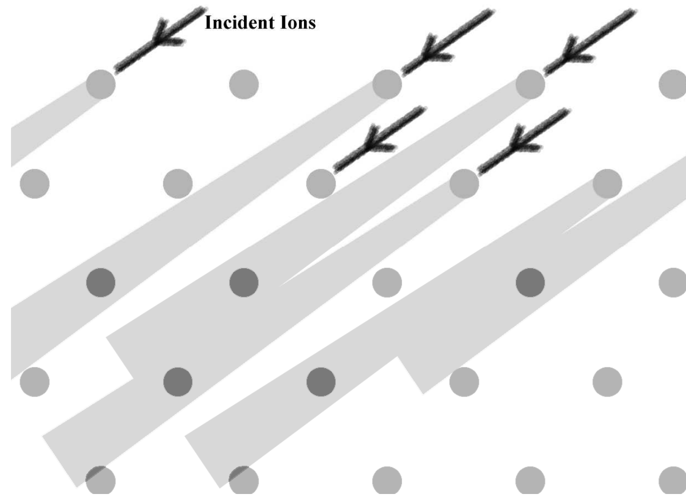

Figure 3.1: Shadowing. By aligning the ion beam along a low index crystallographic direction, the atoms deeper in the crystal are effectively shadowed from the beam.

of the blocking cone it neglects screening of nuclear charge. A more accurate description can be given by the Molière approximation [3, 21]. The radius of the shadow cone then becomes

$$R_M = \xi R \tag{3.2}$$

ξ is the screening potential, which takes a value less than one.

Shadowing has the overall effect that the illumination of the crystal is restricted to a certain depth, although thermal vibrations mean that the shadowing is not ideal and deeper layers do provide some contribution to the backscattered yield. This means that the scattered ions are surface sensitive, with the added advantage that buried interfaces close to the surface can still be probed. Careful selection of scattering geometry can therefore be used to dictate the number of layers exposed.

Although shadowing is useful, further information about the crystal under investigation can be gained by the use of “double alignment”. This essentially uses the same technique as shadowing but to produce blocking of the scattered

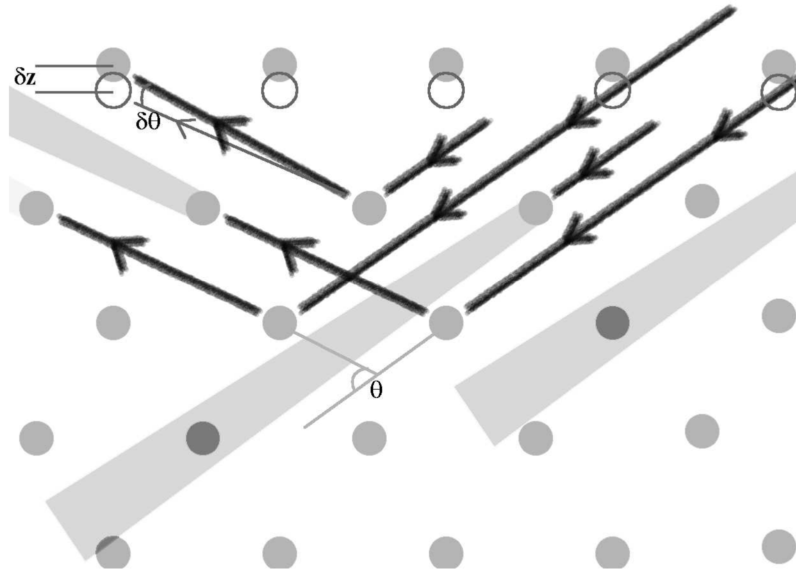

Figure 3.2: Blocking. Scattered ions are blocked in their path back out of the crystal by atoms closer to the surface in a process analogous to the initial blocking. A shift in atomic position results in a shift in the angular position of a blocking feature.

ions (i.e. scattered ions are detected around another low index direction). There is then a drop in scattering yield at characteristic angles where the scattered beamintersects atoms on its way out of the crystal, as demonstrated in Figure 3.2.

A relaxation of the surface layer will then produce a change in the scattering angle of a blocking feature as Figure 3.2 shows. Additional blocking features may also be present due to reduced shadowing of deeper layers. This means that detecting the scattering yield as a function of angle gives real space geometrical information regarding the crystal atomic positions.

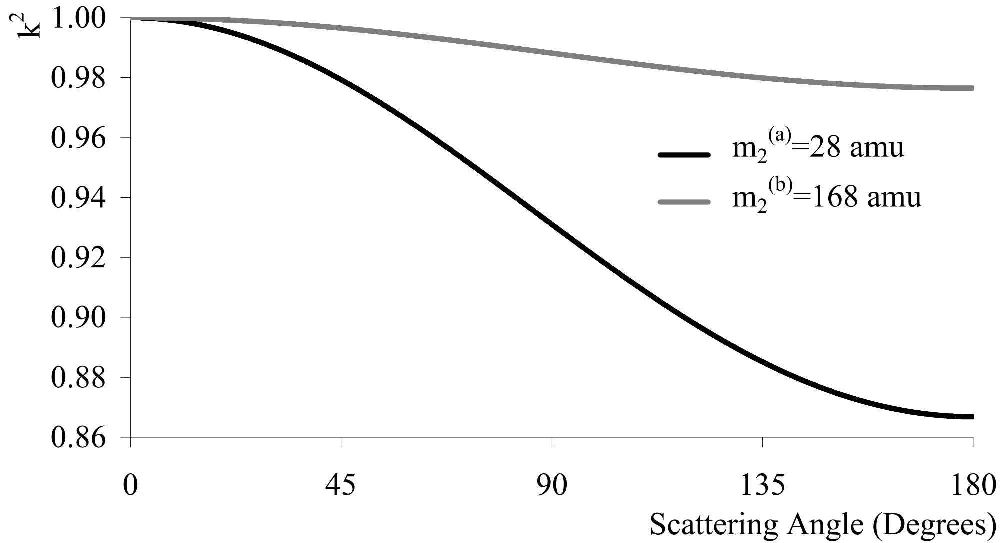

Figure 3.1: The kinematic factor k^2 as a function of scattering angle for two target masses of 28 amu and 168 amu, calculated for the case of H^+ ions.

3.2.2 *Kinematic Scattering*

As mentioned above, the scattering of the ion from an atomic nucleus within the crystal can be treated as a kinematic event. Considering elastic scattering between two bodies, an ion with initial energy E_0 and mass m_1 scattered from a target of mass m_2 over a scattering angle θ (see Figure 3.2), will scatter with energy given by

$$E = \left[\frac{\left(m_2^2 - m_1^2 \sin^2 \theta\right)^{1/2} + m_1 \cos\theta}{m_1 + m_2} \right]^2 E_0 = k^2 E_0 \qquad (3.3)$$

k^2 is known as the kinetic energy loss factor and it has important consequences for MEIS. A plot of k^2 as a function of scattering angle in the case of H^+ ions is shown in Figure 3.3 for two different target masses, $m_2^{(a)}$ and $m_2^{(b)}$. The kinematic factor for the two target masses becomes increasingly different with increasing scattering angle. In practice this means that for sufficiently high scattering angles MEIS has the power to resolve elements of different mass

Original in colour

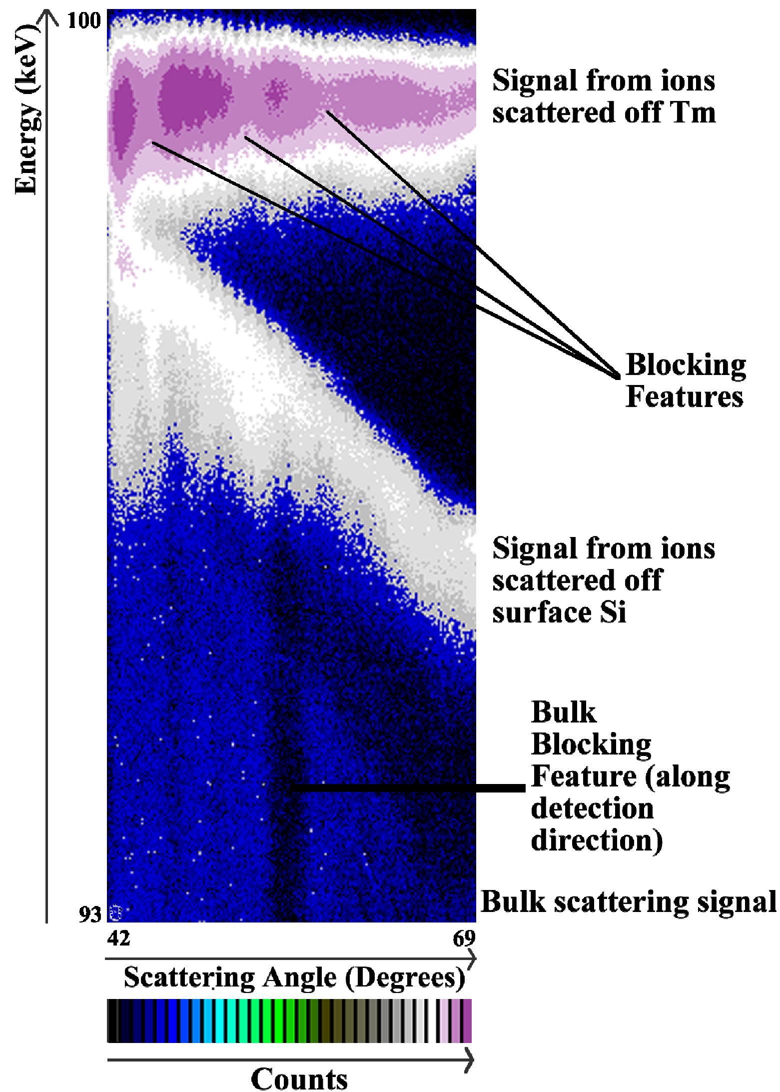

Figure 3.4: An example MEIS spectra (taken from the Tm 2D silicide system, see Chapter 4 for details). This spectrum demonstrates many of the features of a typical MEIS spectrum. The signals from scattering from the Si and Tm are well separated due to the mass difference between the two elements. The Tm scattering signal shows the characteristic fall in counts at increasing scattering angle due to the Rutherford scattering cross-section. The drop in energy with increasing scattering angle is most evident in the Si scattering signal. The Tm scattering signal shows clear evidence of ions being blocked at specific scattering angles. The detection around a major crystallographic direction is evidenced by the bulk blocking feature.

within the crystal. Also, for a given mass, k^2 decreases with increasing scattering angle. This results in ions scattered through higher angles having lower energies. Both of these effects are shown in the example MEIS spectrum, Figure 3.4.

Another factor affecting the scattering data from a MEIS experiment is the fall off in the number of counts with increasing scattering angle. This is a consequence of the Rutherford scattering cross-section, $d\sigma/d\Omega$. The scattered ion flux I over a solid angle $\Delta\Omega$ is given by

$$I = NQ\left(\frac{d\sigma}{d\Omega}\right)\Delta\Omega \tag{3.4}$$

where for the incident ion flux Q, N is the number of atoms contributing to the backscattering. The Rutherford scattering cross-section is given by

$$\frac{d\sigma}{d\Omega} = F\left[\frac{Z_1 Z_2 e^2}{4E\sin^2(\theta/2)}\right]^2 g(\theta, M_1, M_2) \tag{3.5}$$

F is a factor to correct for screening of the target nucleus by electrons, Z_1 and Z_2 are the ion and target atomic numbers, E is the incident energy and $g(\theta, M_1, M_2)$ is a transformation from the centre of mass to laboratory frame.

Equations 3.4 and 3.5 shows that there is a strong dependence in the scattered ion flux with scattering angle. The equations also show that MEIS is more sensitive to heavier elements, as the Rutherford scattering cross-section, and hence detected ion flux, is proportional to the square of the atomic number. Again this can be seen in Figure 3.4.

A final factor when considering MEIS spectra is the energy loss due to inelastic scattering between the ion and electrons. The rate of this energy loss is known as the stopping power. The stopping power depends on the material and the ion energy, which of course decreases due to the inelastic collisions as the ion moves through the crystal. The stopping power is therefore not constant as the ion moves through the sample. However, in MEIS the layers are normally thin

enough and inelastic loses small enough that the stopping power can be taken to be constant before backscattering and then taken to be a different constant after the backscattering event. Taking this surface approximation that backscattering occurs close to the surface and inelastic losses are therefore small,

$$\left(\frac{dE}{dr}\right)_{E_{in}} = \left(\frac{dE}{dr}\right)_{E_0} \tag{3.6}$$

and

$$\left(\frac{dE}{dr}\right)_{E_{out}} = \left(\frac{dE}{dr}\right)_{k^2E_0} \tag{3.7}$$

The inelastic energy loss per unit length normal to the surface is given by

$$\frac{dE}{dz} = \left[\frac{k^2}{\cos\theta_1}\left(\frac{dE}{dr}\right)_{E_0} + \frac{1}{\cos\theta_2}\left(\frac{dE}{dr}\right)_{k^2E_0}\right] \tag{3.8}$$

where θ_1 and θ_2 are as defined in Figure 3.6.

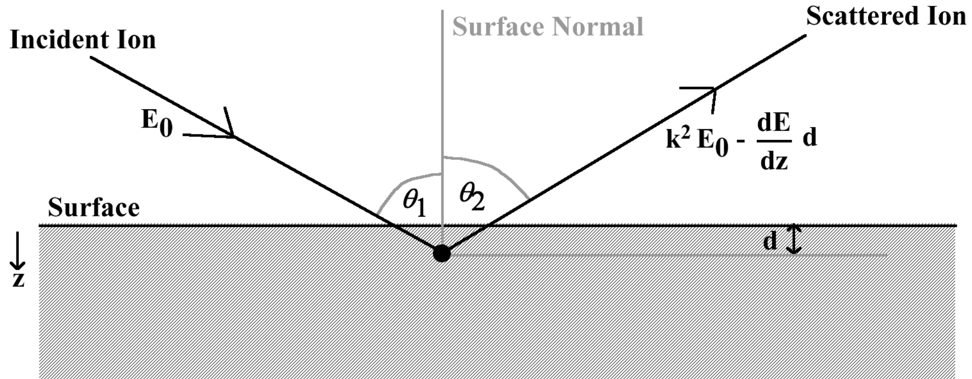

Figure 3.6: The energy loss due to inelastic scattering becomes greater the deeper the ion penetrates. An ion entering the crystal with energy E_0 and being scattered at a depth d from the surface exits with energy given by Equation 3.9.

Therefore the energy of an ion scattered at a depth d will be

$$E = k^2E_0 - \left[\frac{k^2 d}{\cos\theta_1}\left(\frac{dE}{dr}\right)_{E_0} + \frac{d}{\cos\theta_2}\left(\frac{dE}{dr}\right)_{k^2E_0} \right] \qquad (3.9)$$

Equation 3.9 reveals that the energy scale is therefore a depth scale, as well as being a mass scale due to the elastic scattering. This means MEIS can also be used as a powerful depth profiling technique as well as for structural determination.

MEIS data may therefore be considered in two ways. In the first the data is considered as a function of the energy of the scattered ions integrated over a given angular range. This acts as both a mass and depth scale. Second the data may be considered as a function of angle, the number of counts being integrated over a given energy range. This gives direct geometric information regarding the structure of the surface layers. Within this plot of counts as a function of angle there will be a dip in counts at scattering angles where ions have been blocked by surface atoms. The angular width of these dips is given by [1]:

$$\psi = 2\left(\frac{nAc}{Es^n}\right)^{1/(n+1)}\left(1+\frac{1}{n}\right) \text{ radians} \qquad (3.10)$$

Here s is the distance between the atom which scattered the ion and the atom which blocked the ion, E is the ion energy given by Equation (3.3), n is the power of the potential, A is the potential parameter and the factor c is given by

$$c = \sqrt{\pi}\,\frac{\Gamma(1/2n + 1/2)}{\Gamma(1/2n)} \qquad (3.11)$$

For a Coulomb potential Equation (3.11) reduces to

$$\psi = 4\left(\frac{A}{Es}\right)^{1/2} \qquad (3.12)$$

$$A = \frac{Z_1 Z_2 e^2}{4\pi\varepsilon_0} \qquad (3.13)$$

Therefore the typical width of a blocking dip is a few degrees.

3.3 Simulation of Scattering Curves

Although it is possible to directly interpret MEIS data as described above, for a true quantitative structural analysis it is desirable to simulate the scattering of ions from a number of trial structures and compare these simulations with experiment. If nothing else then simple geometrical considerations, whilst providing a good starting point, neglect the effect of lattice vibrations which may introduce additional scattering as deeper layers are imperfectly shadowed. There may also be edge effects around the shadowing cones which can enhance the scattering yield at particular angles. Monte Carlo simulations are performed using a FORTRAN computer code known as VEGAS, developed by the FOM Institute [2, 19, 21, 22]. A brief description of the method by which the scattering is simulated is given here.

3.3.1 Hitting and Detection Probabilities

As mentioned above, the ions involved in MEIS are travelling with a speed approximately three orders of magnitude faster than the lattice vibrations of the atoms in the crystal, which allows a simple snapshot of the sample to be considered, the atoms “frozen” in their thermally displaced positions. The trajectory of the ion can then be modelled as a series of straight line segments between deflections.

Figure 3.6 below shows the basic double alignment situation. The ion enters the crystal parallel to the z_1-axis and passes a number of atoms before scattering from atom A. It then passes a number of atoms, exiting the crystal parallel to the z_2-axis. Now if the intersection of ion beam and atom A at position $\mathbf{r_a}$ has

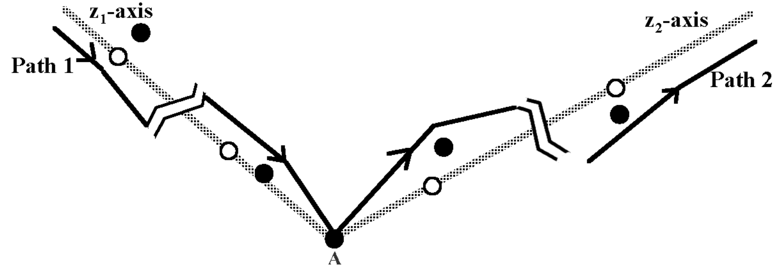

Figure 3.6: Basic double alignment scattering. Open circles indicate equilibrium positions of atoms, filled circles the thermally displaced positions in the crystal snapshot. The ion enters parallel to the z_1-axis, scatters from atom A and exits parallel to the z_2-axis.

probability $P^1(\mathbf{r_a})$, and the probability of the ion being emitted from $\mathbf{r_a}$ and being reaching the detector is $P^2(\mathbf{r_a})$, then the double alignment probability of scattering from atom A at $\mathbf{r_a}$ being detected is given by

$$P_a^{DA} = \int P^1(\mathbf{r_a})G_a(\mathbf{r_a})P^2(\mathbf{r_a})d\mathbf{r_a} \tag{3.14}$$

$G_a(\mathbf{r_a})$ being the Gaussian probability density for the thermal displacement of atom A.

Hitting and detection probabilities are given by

$$P_a^1 = \int P^1(\mathbf{r_a})G_a(\mathbf{r_a})d\mathbf{r_a} \tag{3.15}$$

and

$$P_a^2 = \int P^2(\mathbf{r_a})G_a(\mathbf{r_a})d\mathbf{r_a} \tag{3.16}$$

respectively. Note that equation (3.16) arises due to the fact that the ion scattering is time reversible. i.e. the probability of detecting the ion scattered from atom A along the z_2-axis is equal to the probability of an ion entering the crystal along the z_2-axis being scattered from atom A.

The double alignment probability can be very well approximated by

$$P_a^{DA} \approx P_a^1 P_a^2 \tag{3.17}$$

The hitting and detection probabilities can therefore be calculated independently and multiplied together to give the total double alignment probability.

3.3.2 Calculation of Probabilities: The Standard Method

Two methods are described in the literature for the calculation of the hitting and detection probabilities [21, 23]. They are shown by Tromp and van der Veen [21] to be equivalent.

Figure 3.7 shows the scheme used in the so called standard method, originally due to Barrett [23]. The ion enters at position $\mathbf{r_0}(\mathbf{x},\mathbf{y})$ and is subsequently scattered by atoms located at $\mathbf{r_1}'$, $\mathbf{r_2}'$, ..., $\mathbf{r_n}'$. A collision occurs if the atom in plane n is located at $\mathbf{r_0} + \mathbf{\Delta n}$. The probability density for such a track through the planes 1,...,n is given by

$$p(\mathbf{r}_0) = G_i(\mathbf{r_0} + \Delta\mathbf{n}) \prod_{j=1}^{n-1} G_j(\mathbf{r_j}') \tag{3.18}$$

Integrating over all possible values of $\mathbf{r_0}$ and sets of $\{\mathbf{r_1}', \mathbf{r_2}', ..., \mathbf{r_{n-1}}'\}$ gives

$$P_n = \int ... \int G_n(\mathbf{r_0} + \Delta\mathbf{n}) \left[\prod_{j=1}^{n-1} G_j(\mathbf{r_0} + \mathbf{r}_j) d\mathbf{r}_j \right] d\mathbf{r_0} \tag{3.19}$$

having substituted $\mathbf{r_j}' = \mathbf{r_0} + \mathbf{r_j}$ and $d\mathbf{r_j}' = d\mathbf{r_j}$ as integration over $\mathbf{r_j}$ is performed at constant $\mathbf{r_0}$.

This integral has 2n integration factors and so must be solved numerically. Random values of $\mathbf{r_0}$ are chosen uniformly from a sufficiently broad area and the $\{\mathbf{r_j}\}$ chosen quasi-randomly from the G_j of the atoms. The track is then

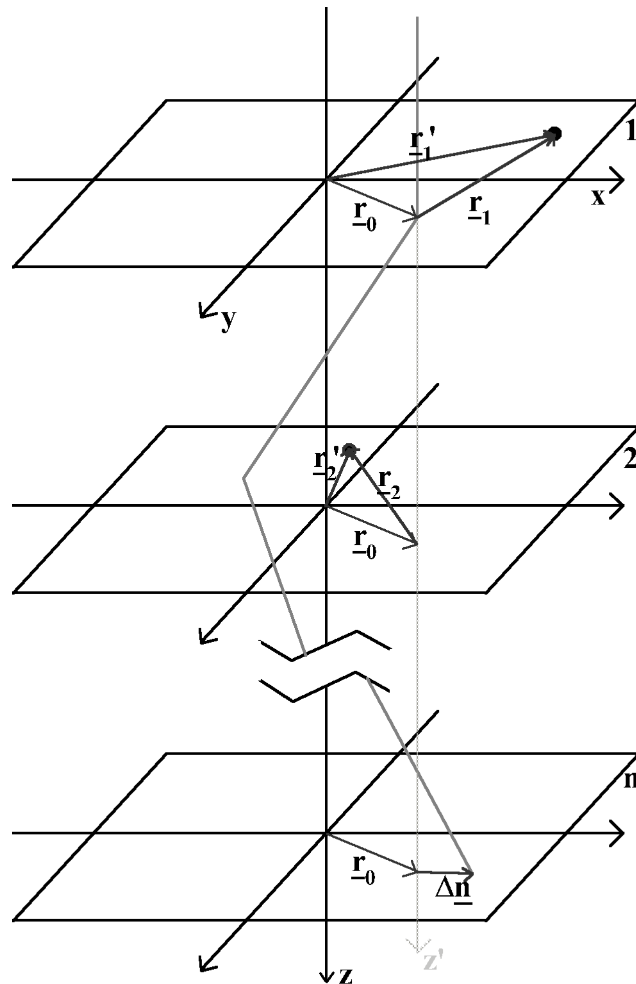

Figure 3.7: Schematic of the standard scheme for determining hitting probabilities. The ion enters at $\boldsymbol{r_0}$ *and scatters from each atom in turn before colliding with the atom located at* $\boldsymbol{r_0} + \boldsymbol{\Delta n}$*. Note the z′-axis is the z-axis of the Tromp and van der Veen method.*

calculated and the probability density for a nuclear encounter, $G_n(\mathbf{r_0} + \mathbf{\Delta n})$ is found. This is repeated for many ion tracks to give p_n after appropriate normalisation.

3.3.3 Calculation of Probabilities: Tromp and van der Veen's Method

The method proposed by Tromp and van der Veen [21] is related to that of Barrett by a simple coordinate transformation. There is, however, one important difference. Within the new formalism it is possible to calculate the hitting probabilities of atom i when it is located at a specific $\mathbf{r_i}$, something which is

impossible within the standard formalism. This enables double alignment geometries to be calculated with reasonable efficiency.

Figure 3.8 shows the schematic for the new scheme. The probability that atom i is hit by the ion beam which impinges on the crystal along the z-axis is calculated as follows. The ion is deflected by atoms 1, 2, ..., i-1 at positions $\{\mathbf{r}_1, \mathbf{r}_2, ..., \mathbf{r}_{i-1}\}$ before passing through the ith plane. In general it will not pass through this plane at $\mathbf{r}_i$ but at a position $\boldsymbol{\delta}\mathbf{r}_i$ away. However, only the coordinates of the atoms relative to the incoming ion beam determine the deflection angles and

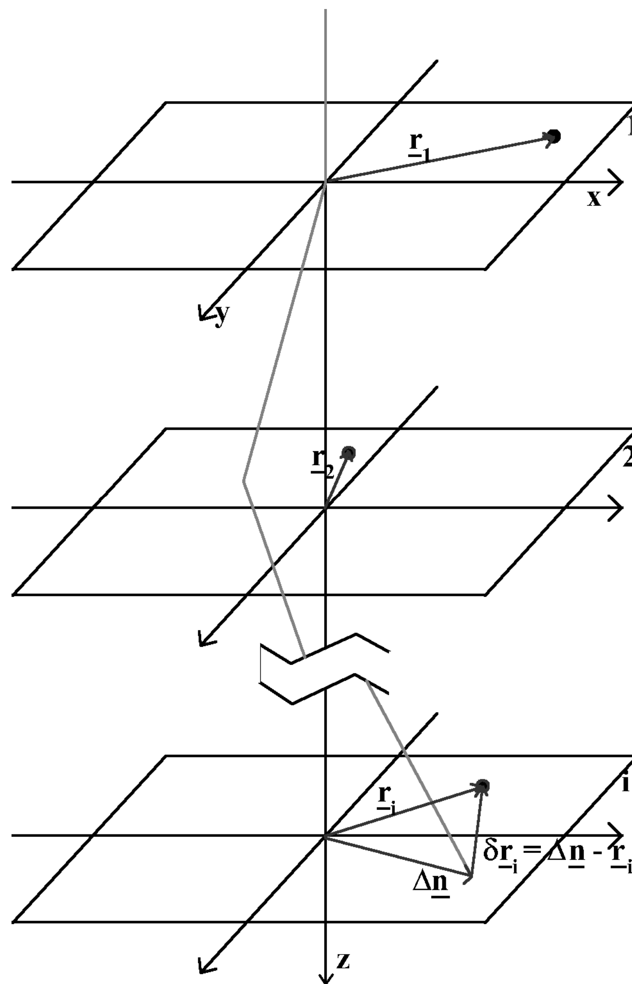

Figure 3.8: Schematic of Tromp and van der Veen's scheme for determining hitting probabilities. The ion enters along the z-axis and is scattered by each atom in turn until passing through the ith layer at $\boldsymbol{\Delta n}$*,* $\boldsymbol{\delta r_i}$ *from the ith atom. This scheme is related to Barrets by a simple coordinate transform (see Figure 3.7).*

hence the position at which the beam passes through plane i. If the atoms were located at $\{\mathbf{r_1} - \boldsymbol{\delta}\mathbf{r_i}, \mathbf{r_2} - \boldsymbol{\delta}\mathbf{r_i}, ..., \mathbf{r_{i-1}} - \boldsymbol{\delta}\mathbf{r_i}\}$ and the beam entered the crystal at $-\boldsymbol{\delta}\mathbf{r_i}$ then it would pass through the ith plane at $\mathbf{r_i} + \boldsymbol{\delta}\mathbf{r_i} - \boldsymbol{\delta}\mathbf{r_i} = \mathbf{r_i}$ and a collision would occur.

The probability density for a collision at point $\mathbf{r_i}$ is therefore given by the probability density for the atoms to occupy not $\{\mathbf{r_1}, \mathbf{r_2}, ..., \mathbf{r_{i-1}}\}$ but $\{\mathbf{r_1} - \boldsymbol{\delta}\mathbf{r_i}, \mathbf{r_2} - \boldsymbol{\delta}\mathbf{r_i}, ..., \mathbf{r_{i-1}} - \boldsymbol{\delta}\mathbf{r_i}\}$.

$$p_i = \prod_{j=1}^{i-1} G_j(\mathbf{r_j} - \delta\mathbf{r_i}) \qquad (3.20)$$

The probability density of hitting atom i at position $\mathbf{r_i}$ is then the integral over all possible positions of the previous i - 1 atoms

$$P_i(\mathbf{r_i}) = \int \prod_{j=1}^{i-1} G_j(\mathbf{r_j} - \delta\mathbf{r_i})d\mathbf{r_j} \qquad (3.21)$$

The hitting probability of atom i is given by integration over all possible positions of atom i

$$P_i = \int G_i(\mathbf{r_i})P_i(\mathbf{r_i})d\mathbf{r_i} \qquad (3.22)$$

This can easily be shown to be equivalent to the standard method. Substituting $\mathbf{r_i}'' = \mathbf{r_i} - \boldsymbol{\Delta}\mathbf{n} = -\boldsymbol{\delta}\mathbf{r_i}$ into equation (3.21) and using $d\mathbf{r_i}'' = d\mathbf{r_i}$ as $\boldsymbol{\Delta}\mathbf{n}$ does not depend on $\mathbf{r_i}$ gives

$$P_i = \int ... \int G_i(\mathbf{r_i}'' + \Delta\mathbf{n})\left[\prod_{j=1}^{i-1} G_j(\mathbf{r_j} + \mathbf{r_i}'')d\mathbf{r_j}\right]d\mathbf{r_i}'' \qquad (3.23)$$

If $\mathbf{r_i}''$ is renamed $\mathbf{r_0}$ then equation (3.23) is seen to be identical to equation (3.19) under the standard method, and the two formalisms are equivalent.

Again integration is performed by Monte Carlo methods. Uniform random values of $\{\mathbf{r_1}, ..., \mathbf{r_{i-1}}\}$ are chosen and the value of $\mathbf{r_i}$ chosen according to the Gaussian probability distribution. The ion track is determined and the probability densities for the shifted positions found. Averaging over many tracks produces the hitting probability.

3.3.4 Connection of Ingoing and Outgoing Ion Tracks

Equation (3.17) makes the approximation that the incoming and outgoing ion tracks are in fact not correlated. In reality of course there is a correlation, both sharing the same thermally displaced position of the scattering atom. Under normal circumstances this approximation does not cause problems. However, if the hitting probabilities are strongly varying with $\mathbf{r_a}$ for positions close to atom a's equilibrium position, then the approximation may result in a slight shift of the angular position of a blocking minima.

The two tracks may be connected by using a combination of the methods of Barrett and Tromp and van der Veen as described in sections 3.3.1 and 3.3.2 respectively. Barrett's method is used for the calculation of the incoming tracks and then the interception with the final plane is used as the position of the target atom in a calculation for the (time reversed) outgoing track using the method of Tromp and van der Veen, causing the two tracks to intersect. This has the disadvantage that Tromp and van der Veen's method results in a large number of ion tracks with low probability because they must be shifted to intersect the scattering position.

In all the work reported in this thesis, simulations of blocking curves do not have ingoing and outgoing tracks connected. The reasoning behind this is two fold. First it is not expected that any significant error should be introduced by this approximation. The approximation is most likely to fail when the scattering atom lies at the edge of a shadow cone, a situation not encountered in this work. Second, from a practical point of view, the portion of the computer codes which allows such a connection does not correctly function as of this writing, so it is not

possible to specify the connection of ingoing and outgoing tracks within the simulations.

3.3.5 Tracking of Ions: The Single Row Approximation

In order to determine the hitting probabilities the ion track (i.e. the sequence of collisions) must be determined. If the shadow cone radius is suitably small enough that scattering between adjacent rows of atoms plays no role (i.e. the shadow cone is smaller than the distance between rows) then the single row approximation may be employed. The ion path is considered as a sequence of small angle deflections along the atomic row, the order of encounters simply being the order of atoms in the row. If the atomic rows are equivalent then periodic boundary conditions may be used.

The single row approximation fails, however, if the ion can scatter between rows. This may occur, for instance, if the ion beam is not aligned, or aligned along a high index direction. Also surface relaxations can cause adjacent rows to be inequivalent so periodic conditions may no longer be applied.

3.3.6 Tracking of Ions: The Complete Crystal Method

To overcome the shortfalls of the single row approximation the VEGAS codes use the more sophisticated complete crystal method. The complete crystal is treated as a slab of the depth to be considered in scattering, constructed of periodically repeated building blocks which have the lateral dimensions of the $n \times m$ unit cell. If necessary two or more unit cells are combined to get a rectangular building block. The hitting probabilities are calculated as described above. The order of collisions is now lost and must be found for each ion individually.

Whilst in principle it would be possible to determine the next collision partner by calculating the distance from the projected ion trajectory to all atoms within the block, this is prohibitively expensive in computational time. Instead an auxiliary

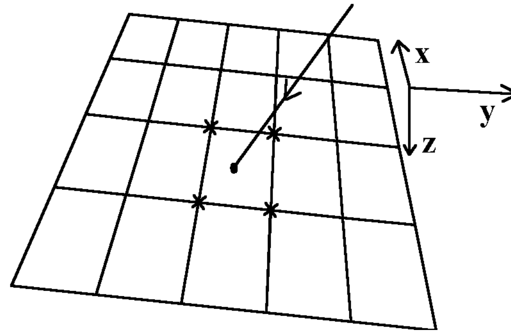

Figure 3.9: In the complete crystal method an auxiliary lattice can be constructed by grouping atoms with (nearly) identical x-, y- or z-coordinates. This can then be used to track the ion through the crystal. As each atom occupies one auxiliary lattice point, and each lattice point contains zero or one atoms, only four auxiliary lattice points need be checked for potential collision partners.

lattice is formed by grouping the atoms within the block into sets with (nearly) identical x-coordinates, (nearly) identical y-coordinates and (nearly) identical z-coordinates. These sets define x-, y- and z-planes, the intersections of which define the points of the rectangular auxiliary lattice. Each auxiliary lattice point is either empty or contains exactly one atom. Each atom within the original block is assigned to exactly one auxiliary lattice point. Now at most four atoms must be considered as potential collision partners at any time.

Suppose that the ion beam is travelling primarily in the z-direction, as shown in Figure 3.9. Its path is constructed by the intersects with consecutive z-planes.

Given a typical nearest neighbour distance of about 2 Å and a typical impact parameter of around 0.5 Å, the ion is close enough to no more than one atom, which means only four lattice points need be considered.

Although it may seem restrictive to have to construct a rectangular auxiliary lattice, this has not been found to be a problem even for quite complex reconstructions [19].

3.3.7 Multiparameter Simulations

When evaluating hitting probabilities by the methods described above the majority of computational time goes into the calculation of the ion trajectories, whilst relatively little is used in evaluating the probabilities. When comparing simulations with experimental data it is often desirable to vary several parameters over a small range of values in order to determine the most appropriate model. This can be achieved in a relatively efficient manner by the realisation that the information regarding the equilibrium positions of the atoms and their thermal vibrations is hidden within the Gaussian distributions G_i. These distributions do not enter into the calculations until after the calculation of the ion trajectories. Therefore one set of ion trajectories may be used to determine the hitting probabilities for a range a slightly different equilibrium positions and thermal vibrations of the atoms without significant increase in computational time. A range of structural models may then be simulated in a so called "multicalc", systematically varying atomic positions and/or vibrations between each model. This greatly accelerates the search for a structural solution, though care must be taken to ensure that parameters are not moved from the starting positions by too extreme an amount and that a sufficiently high number of ions are used. Experience has shown that an atomic shift of no more than ± 0.3 Å and an ingoing/outgoing ion flux of 100000/50000 ions is adequate in most situations.

3.4 Comparison of Simulation with Experimental Data

Angular cross sections through MEIS spectra produce a plot of scattering yield against scattering angle. Geometrical considerations may gave rise to a number of possible trial structures which are then simulated using the VEGAS code implementing the methods described above. The experimental cross sections are corrected for the effects of the Rutherford scattering cross section and the kinematic energy loss factor. The data may also be corrected for angular miscalibration of the TEA position by comparison of bulk blocking features to simulations of scattering from the bulk atoms of the crystal.

Experimental and simulated scattering curves are compared by use of an R-factor. The R-factor which has become standard within the Daresbury community is a chi-squared R-factor

$$R_\chi = \frac{1}{N}\sum_{n=1}^{N}\frac{(Y_n^{sim} - Y_n^{exp})^2}{Y_n^{exp}} \tag{3.24}$$

Y^{exp} and Y^{sim} being the experimental and simulated yields and N the total number of points. A series of macros are available for the Igor Pro [24] software package [25] to perform such comparisons. As there is no calibration of the data to give absolute yields, the experimental data must be empirically scaled to the simulation. Values of R_χ obtained are therefore purely relative and cannot be compared with those obtained from other data sets or other scattering geometries. A further discussion of R-factors, including some problems associated with R_χ, may be found in Chapter 5.

References

1. W. C. Turkenburg, W. Soszka, F. W. Saris, H. H. Kersten and B. G. Colenbrander, *Nuc. Instrum. Meth.* **132** 587 (1976)

2. R. M. Tromp, *Medium Energy Ion Scattering*, in *Practical Surface Analysis*, p. 577, D. Briggs & M. P. Seah, (Eds.) John Wiley & Sons (1992)

3. J. F. van der Veen, *Surf. Sci. Rep.* **5** 199 (1985)

4. P. Quinn, D. Brown, D. P. Woodruff, T. C. Q. Noakes and P. Bailey, *Surf. Sci.* **491** 208 (2001)

5. P. Bailey, T. C. Q. Noakes and D. P. Woodruff, *Surf. Sci.* **426** 358 (1999)

6. D. Brown, T. C. Q. Noakes, D. P. Woodruff, P. Bailey and Y. Le Goaziou, *J. Phys. Condens. Matter* **11** 1889 (1999)

7. D. Brown, P. D. Quinn, D. P. Woodruff, T. C. Q. Noakes and P. Bailey, *Surf. Sci.* **497** 1 (2002)

8. P. Fenter and T. Gustafsson, *Phys. Rev. B* **38** 10197 (1988)

9. D. P. Woodruff, D. Brown, P. D. Quinn, T. C. Q. Noakes and P. Bailey, *Nucl. Instrum. Meth. B* **183** 128 (2001)

10. T. Yasue and T. Koshikawa, *Surf. Sci.* **377-379** 923 (1997)

11. M. Chester and T. Gustafsson, *Surf. Sci.* **256** 135 (1991)

12. M. Copel, T. Gustafsson, W. R. Graham and S. M. Yalisove, *Phys. Rev. B* **33** 8110 (1986)

13. B. W. Busche and T. Gustafsson, *Phys. Rev. B* **61** 16097 (2000)

14. S. M. Yalisove, W. R. Graham, E. D. Adams, M. Copel and T. Gustafsson, *Surf. Sci.* **171** 400 (1986)

15. T. Nishimura, A. Ikeda, H. Namba and Y. Kido, *Surf. Sci.* **411** L834 (1998)

16. R. L. Headrick and W. R. Graham, *Phys. Rev. B* **37** 1051 (1988)

17. J. V. Barth and D. E. Fowler, *Phys. Rev. B* **55** 1528 (1995)

18. P. Haberle and T. Gustafsson, *Phys. Rev. B* **40** 8218 (1989)

19. J. W. M. Frenken, R. M. Tromp and J. F. van der Veen, *Nucl. Instrum. Meth. B* **17** 334 (1986)

20. I. Stensgaard, R. Feidenhans'l and J. E. Sorensen, *Surf. Sci.* **128** 281 (1983)

21. R. M. Tromp and J. F. van der Veen, *Surf. Sci.* **133** 159 (1983)

22. VEGAS, *FOM Institute*

23. J. H. Barrett, *Phys. Rev. B* **3** 1527 (1973)

24. Igor Pro, *WaveMetrics Inc.*

25. Igor Pro MEIS Macros, P. Bailey, *Daresbury MEIS Facility*

Chapter 4
MEIS Investigation of Thulium Silicide

4.1 Introduction

As described in Chapter 1, two-dimensional rare earth silicides have attracted much attention in recent years, with numerous studies being published. The electronic similarity of all trivalent rare earth metals leads to an expectation that they will all form such structures, as has already been seen to be the case for a large number. The general structure of such silicides is shown in Figure 4.1. The number of structural studies has led to some speculation of a possible trend in structural parameters across the rare earth series (see Chapter 5 for further discussion of such trends). Tm lies towards one end of this series, being one of the heavier trivalent rare earths. Although several [1-3] studies of thicker Tm silicides have been reported there is no study of a two-dimensional Tm silicide. A study of Tm silicide in the monolayer regime may therefore further reveal any structural trend in the series as well as confirming another rare earth which might be used to form such structures in technological applications. Initial investigations [4] suggested that Tm does indeed form such a silicide but seemed to show a discrepancy with the expected trend, which led to the careful medium energy ion scattering study described here. The technique is ideally suited to quantitative structural investigations of these rare earth silicides.

4.2 Experimental Details

All samples were prepared *in situ* at the Daresbury Laboratory MEIS Facility (see Chapter 2 for details of the facility) under UHV conditions with a base pressure of around 1×10^{-10} mbar. Si (111) samples, approximately 10×10 mm^2, were cut from lightly doped 100 Ω cm, *n*-type wafers. The samples were cleaned by repeated e$^-$-beam rapid heating to 1200 ˚C for approximately one minute

Original in colour

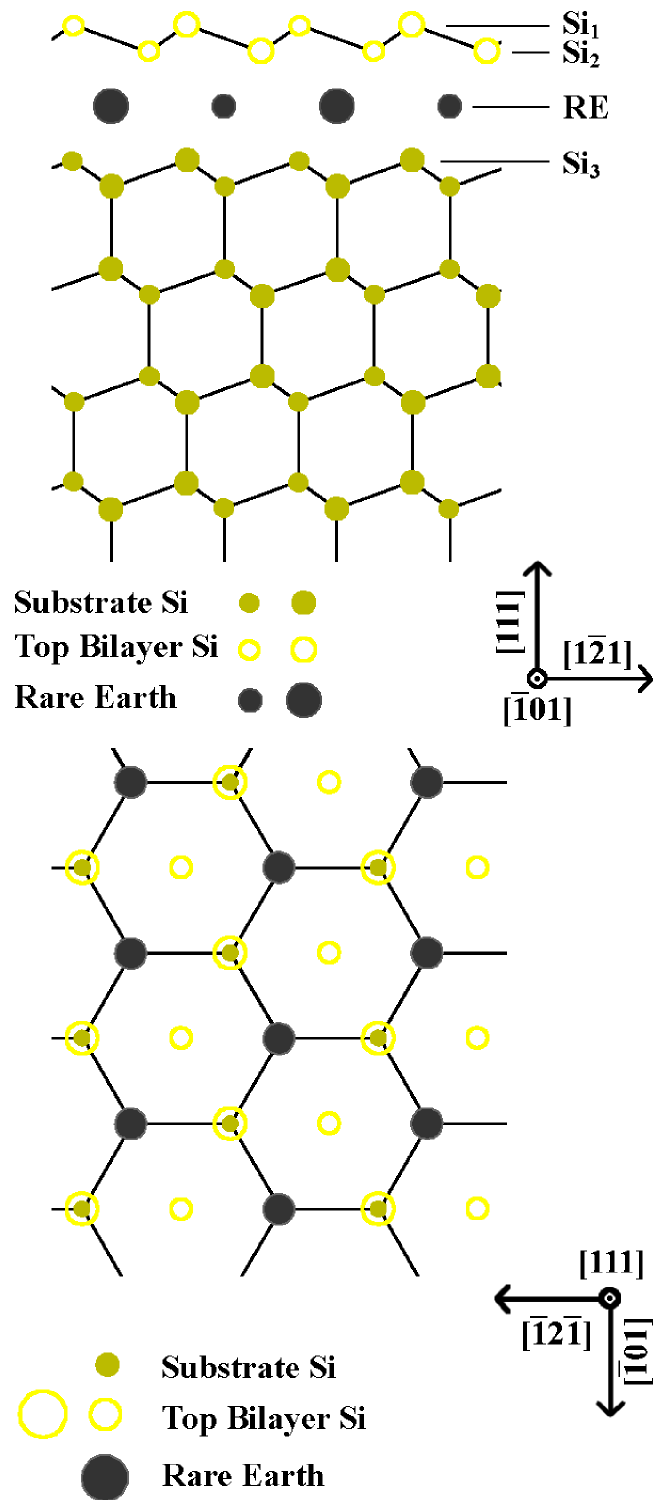

Figure 4.1: Structure of 2D rare earth silicides. The RE forms a single atomic layer located in T4 sites above the bulk Si. The silicide is terminated by a bulk-like Si bilayer (Si_1 and Si_2) which is rotated by 180° with respect to the bulk. a) side view, b) the view along the surface normal (i.e. top view).

followed by slow (<100 ˚C min^{-1}) cool down to room temperature. Sample temperature was monitored using an infra red pyrometer. The cleanliness of the Si (111) samples was confirmed by the presence of a sharp 7 × 7 LEED pattern. Auger electron spectroscopy also confirmed a lack of surface contamination by such impurities such as oxygen and carbon.

Tm was deposited onto the clean, newly prepared 7 × 7 surface by evaporation from a tungsten boat arrangement of an in house design. The samples were at room temperature during the deposition. The pressure during Tm evaporation was less than 1 × 10^{-9} mbar. The rate of Tm evaporation was approximately 6 min/ML. Again AES showed no surface contamination after Tm deposition. LEED of an as deposited sample produced only a diffuse pattern with no evidence of order. The samples were e^{-}-beam annealed to approximately 500 ˚C (as measured using the infra red pyrometer) for ten minutes and allowed to cool to room temperature. A sharp 1 × 1 LEED pattern was taken as indicating that an ordered surface reconstruction had successfully formed.

Samples were transferred under UHV conditions into the scattering chamber where they were placed on the precision goniometer in front of the incoming ion beam. The ion beam consisted of 100 keV H^{+} ions. The sample was aligned so that the beam was incident along a low index crystallographic direction, and scattered ions were detected around another low index direction in double alignment experiments. Two such scattering geometries were utilised, namely [$\bar{1}$ 00] incidence direction, with the detection around the [$\bar{1}$ 11] direction and the time reversed path of this (hereafter referred to as [$\bar{1}$ 00]/[$\bar{1}$ 11] and [1$\bar{1}$ $\bar{1}$]/[100]). These geometries are illustrated in Figure 4.2. The MEIS data could be used to further confirm the cleanliness of the sample, and the clear blocking dips in the angular cross section confirmed an ordered surface reconstruction. Complete data sets were collected with a beam dose of 10^{16} ions cm^{-2}, the beam size was approximately 0.5 mm × 1 mm normal to the beam. The samples were systematically moved in the z-direction (i.e. while maintaining the double

Original in colour

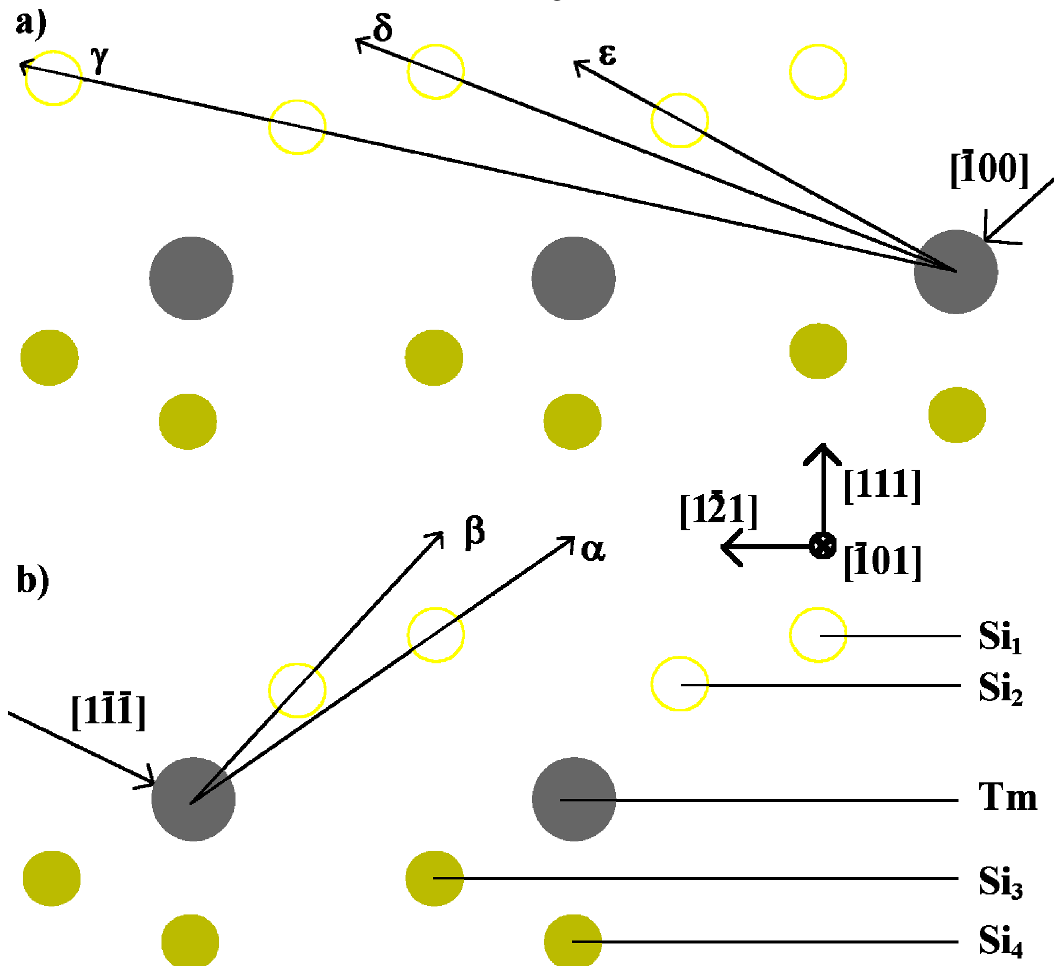

Figure 4.2: The origin of the blocking dips in the Tm signal in the two scattering geometries indicated. a) $[\bar{1}00]/[\bar{1}11]$ b) $[1\bar{1}\bar{1}]/[100]$. The arrows indicate the origin of the blocking features labelled in Figure 4.5. Refer to Figure 4.1 for further details of the structure (note that in this figure only those atoms within the scattering plane are shown). Notice that ε depends only on Si_2.

alignment scattering orientation) between data sets in order to minimise sample damage.

Original in colour

.

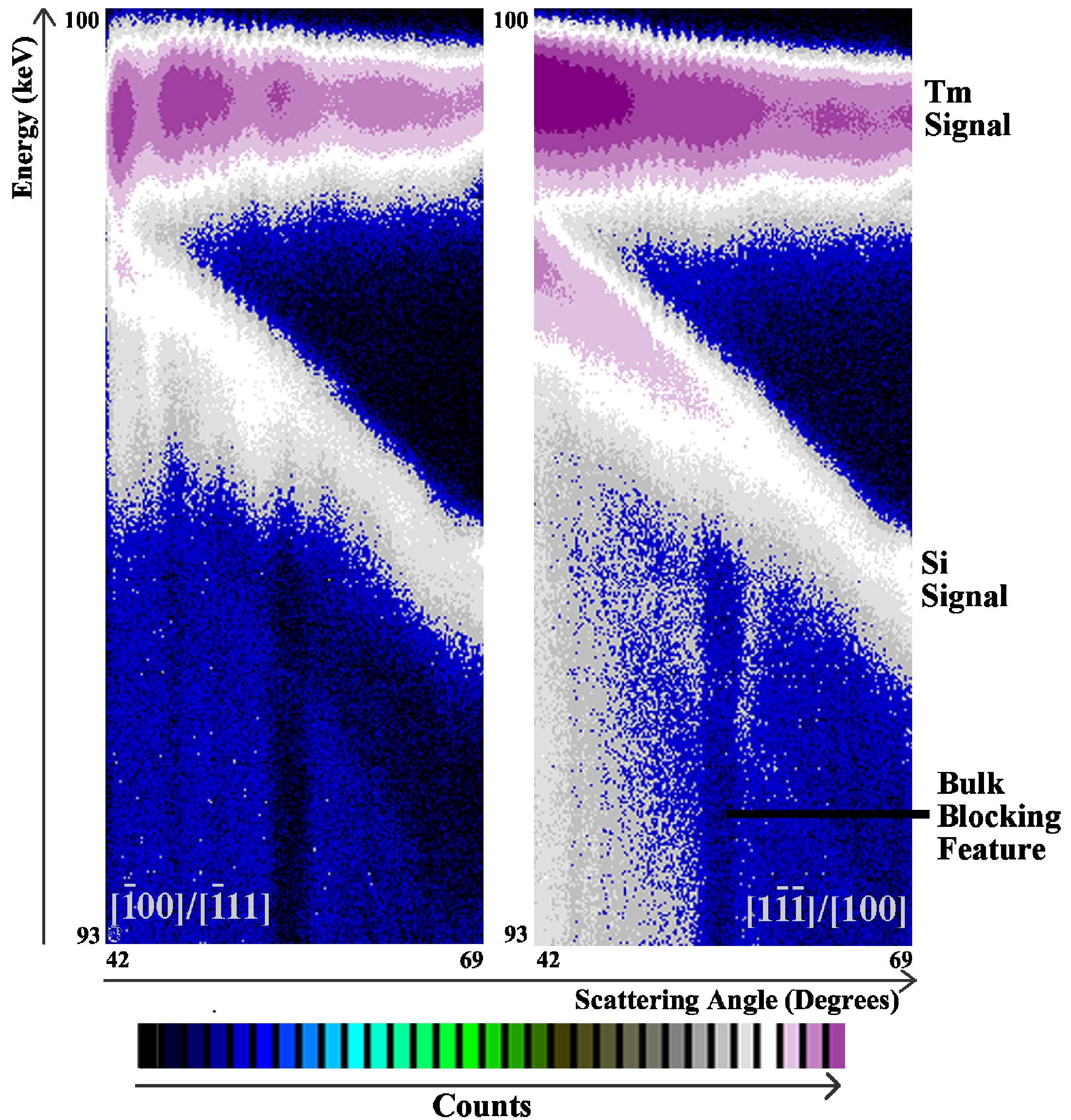

Figure 4.3: Typical MEIS spectra from the Tm silicide for the two experimental geometries employed (left [$\bar{1}$ 00]/[$\bar{1}$ 11]; right [1$\bar{1}$ $\bar{1}$]/[100]). The separation of the Tm and Si signals, and the bulk blocking features are all clearly visible. The Tm signal shows decreased intensity at scattering angles at which blocking has occurred.

4.3 Results and Discussion

4.3.1 Experimental Results and Analysis

Typical MEIS spectra for the two scattering geometries are shown in Figure 4.3. In both cases the signal from ions scattered from the Tm can be clearly resolved from that of those scattered from the Si, as indicated. This is due to kinematic effects as discussed in Chapter 3. Ions scattered with lower energies have been scattered from the bulk Si. The blocking feature along the detection direction in this bulk signal can be seen, and is a useful calibration tool. Even within these raw MEIS spectra, a reduction in counts at certain scattering angles can be seen within the Tm signal, indicating angles at which the scattered ions have been blocked.

The MEIS spectra were analysed by first integrating the number of scattered ions as a function of angle over an energy range corresponding to those ions scattered from bulk Si. This angular cross section thus encompassed the bulk blocking features. Comparison of these cross sections to Monte Carlo computer simulations of scattering from bulk terminated Si allowed the position of the bulk blocking features to be fitted and hence any mechanical offset in the analyser position to be corrected for. An example of such a comparison is shown in Figure 4.4. Note that here it is the fitting of the bulk blocking feature (in the direction around which ions are being detected), especially in terms of angular position, which is particularly important, as this gives the mechanical offset of the analyser. These bulk blocking features are labelled in Figure 4.4. The fact that the simulated surface is bulk terminated Si, which is obviously not the experimental case, results in some features in the simulated scattering curve (such as those around 43–46° in the $[\bar{1}00]/[\bar{1}11]$ geometry) which are not clearly evident in the experimental data. Conversely the ordered overlayer above the bulk silicon may cause weak blocking features in the experimental data or otherwise affect the scattering curve in a way not reproduced by the simulation. Such effects are responsible for the experimental features seen around 43–47° in

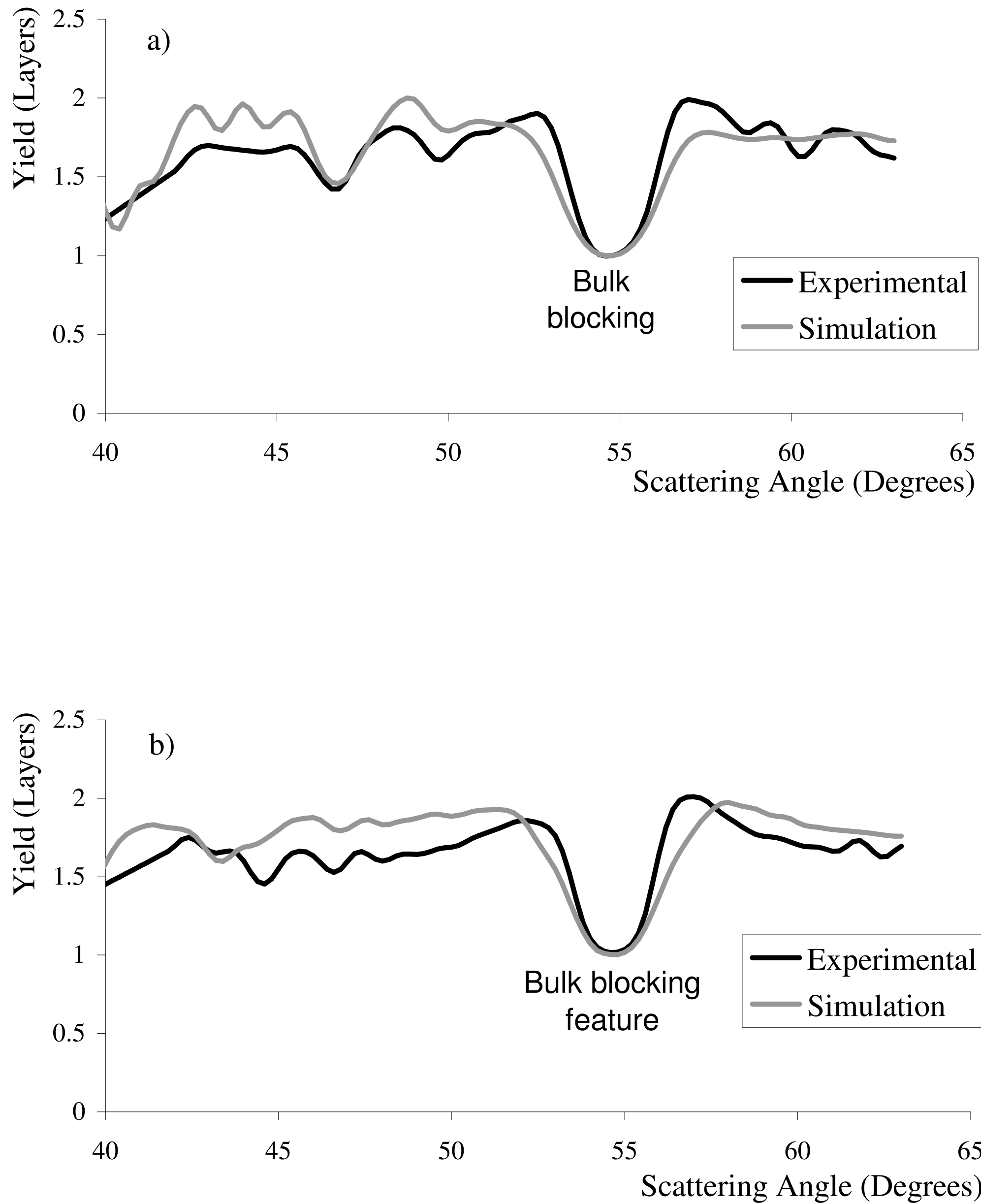

Figure 4.4: The comparison of a simulation of bulk terminated Si (111) to the experimental angular cross section through the bulk scattered ion signal, with angular offset applied. Matching the postition of the bulk blocking feature allows the angular scale to be calibrated correcting for any mechanical offset of the analyser. (a) [$\bar{1}$ 00]/[$\bar{1}$ 11] (b) [1$\bar{1}$ $\bar{1}$]/[100].

the [$1\bar{1}\bar{1}$]/[100], for instance. The experimental data also exhibits further small fluctuations due to noise.

The signal from ions scattered from the Tm was also integrated as a function of scattering angle. The scattering yields from similar data sets were summed to improve the signal to noise ratio. These angular projections were then corrected for the mechanical offset determined from the above bulk fitting as well as for the kinetic energy loss factor (the so called "k^2 correction"). A final correction was applied to remove the effect of the fall off in counts due to the Rutherford scattering cross section. The corrected Tm signal cross sections for the two geometries are shown in Figure 4.5. For comparison purposes the corrected cross section from the Ho signal from a 2D Ho silicide [5] is also shown. The similarity in blocking dip position, size and shape clearly indicate that the Tm silicide has a very similar structure to the Ho silicide, as was expected due to the number of trivalent rare earth metals previously seen to form such two-dimensional silicides. Note that the main blocking features labelled α–ε and the overall shape of the curves are the most important features in terms of structural information and smaller fluctuations within the scattering curves are mainly due to noise.

4.3.2 Computer Simulations

The similarity of Ho and Tm blocking curves suggested that a 2D Tm silicide had indeed formed. In order to confirm this and to fully determine the surface structure of the Tm 2D silicide a series of Monte Carlo computer simulations were performed for each double alignment geometry, using the VEGAS code [6]. The known structure of the two dimensional Ho silicide [5] was taken as a starting structure for these simulations, the Ho being replaced by Tm. Within the simulations two parameters were allowed to vary independently; namely the vertical (z-) positions of Si_1 and Si_2 (i.e. the two atoms forming the top, reversed bilayer, see Figure 4.1). The z-positions of these two atoms were varied whilst holding the other atomic positions fixed. This is a useful approach in the MEIS study of 2D silicides: As the Tm forms a single atomic layer below the reversed

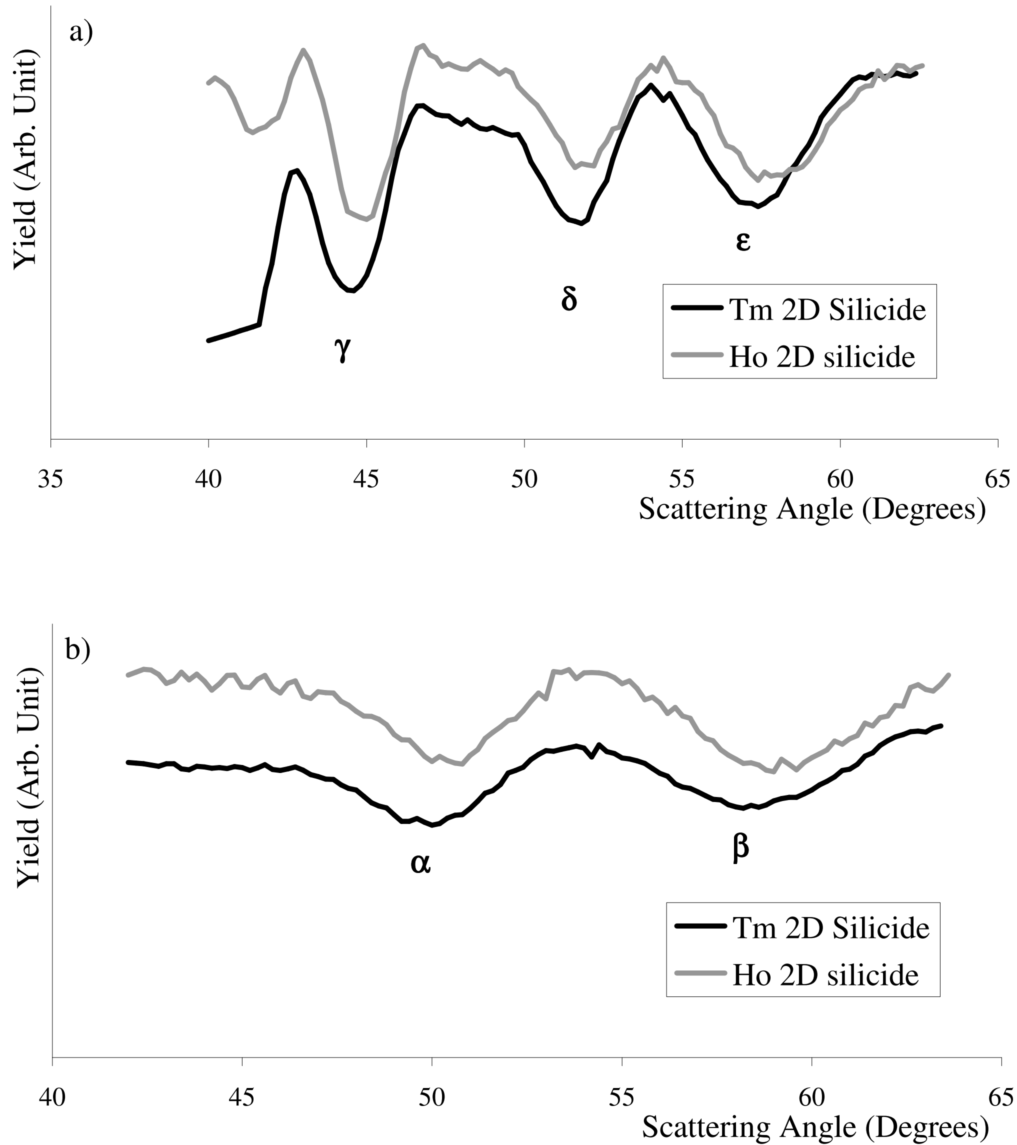

Figure 4.5: The corrected angular cross section through the Tm signal for the (a) [$\bar{1}$ 00]/[$\bar{1}$ 11] geometry and (b) [1$\bar{1}$ $\bar{1}$]/[100] geometry. The curves have been corrected for the angular offset and the fall off in counts due to Rutherford scattering cross section, and scaled to an arbitrary value. Also shown for comparison purposes is the experimental cross section through the Ho signal from a 2D Ho silicide [5]. The similarity of the two curves indicates the structures are very alike, as expected. The small fluctuations within the curves are experimental noise. The labelling of blocking dips refers to Figure 4.2.

bilayer, but above the other, bulk like Si layers, it is only these two top atoms which contribute to blocking features in the Tm signal. Indeed geometrical considerations (Figure 4.2) show that some blocking dips are due to scattered ions being blocked only by Si_1 atoms or only by Si_2 atoms.

Initially the thermal vibrations of the atoms were estimated from the Debye temperatures [7] for Si and Tm (giving rms vibrational amplitudes of 0.085 Å and 0.080 Å respectively). The thermal vibrations of the top two atoms forming the reversed bilayer were enhanced by a factor of √2 over the bulk values.

Comparison between the simulations and experiment was performed by allowing the experimental counts to be freely scaled to the simulation yield. Experiment and simulation were then compared using the χ^2 R-factor

$$R_\chi = \frac{1}{N}\sum_{n=1}^{N}\frac{\left(I_{exp} - I_{sim}\right)^2}{I_{exp}} \qquad (4.1)$$

where I_{exp} and I_{sim} are the scaled experimental and simulation scattering yields, respectively. This has the advantage that its statistical basis gives a ready estimate of the error in the derived value for each structural parameter a_j, given by

$$\sigma_j^2 = 2/(\partial^2\chi/\partial^2 a_j) \qquad (4.2)$$

R-factors from all available geometries were combined to give an overall best fit. Further discussion of R-factors can be found in Chapter 5.

The first simulations consisted of a “multicalc”, performing a wide search of parameter space, varying the positions of Si_1 and Si_2 as described. The atoms were moved independently in 0.02 Å steps in the z-direction (i.e. perpendicular to the surface), over a range of ± 0.20 Å from the starting position. This resulted in 441 structural models for each geometry. The experimental data for each geometry was compared to the appropriate simulations and the R-factors

calculated to produce an "R-factor curve" (a graph of the calculated R-factor versus simulation number). The R-factor curves from each geometry were then combined to produce an overall R-factor curve. The structural model with the minimum overall R-factor was then used as a starting point for further simulations. A set of simulations were performed varying the thermal vibrations of the top two Si atoms and the Tm. The best fit model produced thermal vibrations of 0.12 Å, 0.12 Å and 0.08 Å for Si_1, Si_2 and Tm respectively. Thesethermal vibrations were used in another multicalc around the so far best fit structural model. This sequence of simulations again varied the z-position of Si_1 and Si_2, over a range of ± 0.04 Å and ± 0.02 Å respectively, both in 0.01 Å steps. A final set of simulations around this best fit solution from these simulations confirmed convergence upon that structural model.

The comparison between experiment and simulation for the final best fit model is shown in Figure 4.7. The structural parameters for this model are listed in Table 4.1 and shown in Figure 4.6

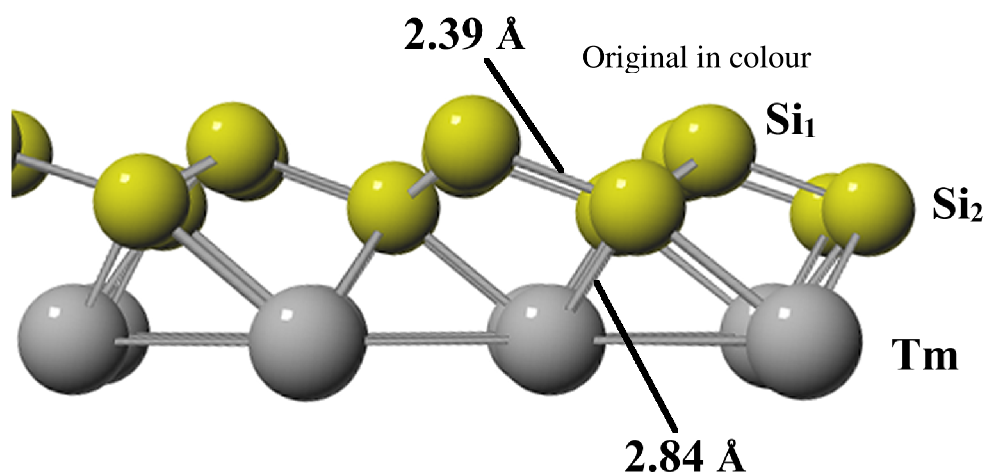

Figure 4.6: Ball and stick representation of the Tm 2D silicide surface, showing the bond lengths of Table 4.1.

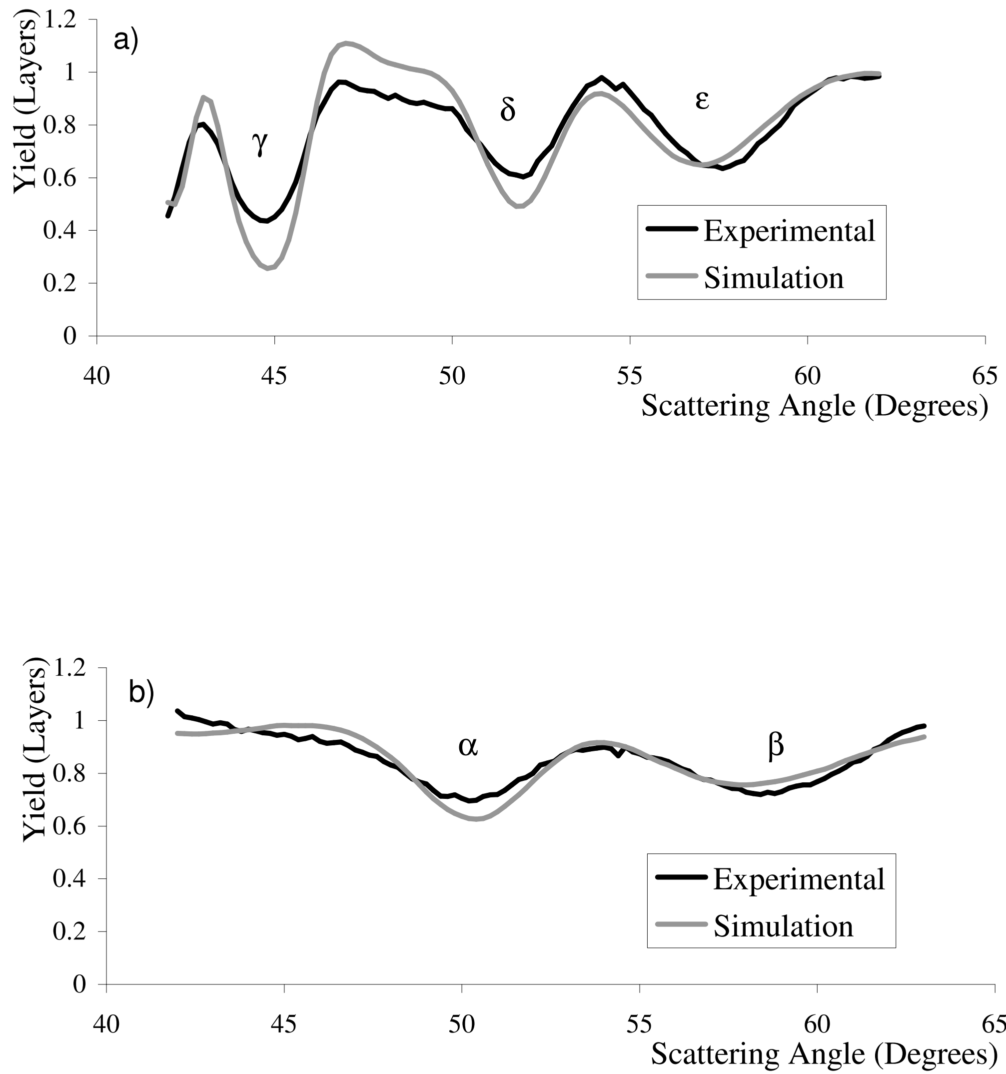

Figure 4.7: Comparison between experimental data and the simulated scattering curve for the initial structural solution for 2D Tm silicide (note that for ease of display the curves have been corrected for the fall off in counts due to the Rutherford scattering cross-section). The experimental data has been freely scaled to the simulation. (a) [$\bar{1}$ 00]/[$\bar{1}$ 11] (b) [1$\bar{1}$ $\bar{1}$]/[100]. The labelling of blocking dips refers to Figure 4.2. Note the poor match of the 57° (ε) blocking feature in the [$\bar{1}$ 00]/[$\bar{1}$ 11] geometry.

	Si_1–Tm (Å)	Si_2–Tm (Å)	Si_1–Si_2 (Å)
Vertical Distance	2.67 ± 0.02	1.77 ± 0.03	0.90 ± 0.03
Bond Length	N/A	2.84 ± 0.02	2.39 ± 0.02

Table 4.1: Structural parameters for the initial best model for the Tm silicide under discussion. The Si_1–Tm bond length is thought to be underestimated while the Si_1–Si_2 bond length is overestimated.

4.3.3 Re-examination of Best Fit Model

An examination of Figure 4.7 (a) shows that the blocking feature at around 57˚ is not particularly well fitted. Visual inspection of the comparison of experimental data and the structural models showed that some, at least quantitatively, fitted this dip more accurately whilst maintaining a comparable match to the rest of the data. As Figure 4.2 shows, the 57˚ blocking dip (labelled ε) is due purely to blocking of scattered ions by Si_2 atoms. Its position therefore directly relates to the atomic position of Si_2. Any failing of the fitting process which results in a solution being selected which is apparently not the best fit, as observed here, is therefore cause for concern.

Further investigation revealed that the depth of the lower blocking dip, at ~45˚ (γ in Figure 4.2), was having an unduly large influence on the R-factor, causing a failure to correctly fit the higher angle dip. Further discussion and justification for this conclusion may be found in the next chapter.

In light of the above discovery, the R-factor for the [$\bar{1}$ 00]/[$\bar{1}$ 11] geometry was recalculated, excluding the lower γ dip from the calculation (essentially the data for this geometry was cut off below about 47˚. However, the main structural information is contained within the angular position of the dip. The γ dip is due to both Si_1 and Si_2. These atoms cause the other two dips in this geometry, so the positional information is contained within the remaining portion of data. This procedure was therefore felt to be justified in an effort to improve the high angle dip fit and therefore the accuracy of the Si_2 position). This led to a new best fit structural model, shown in Figure 4.8. It may be noted that the ~57˚ dip is now

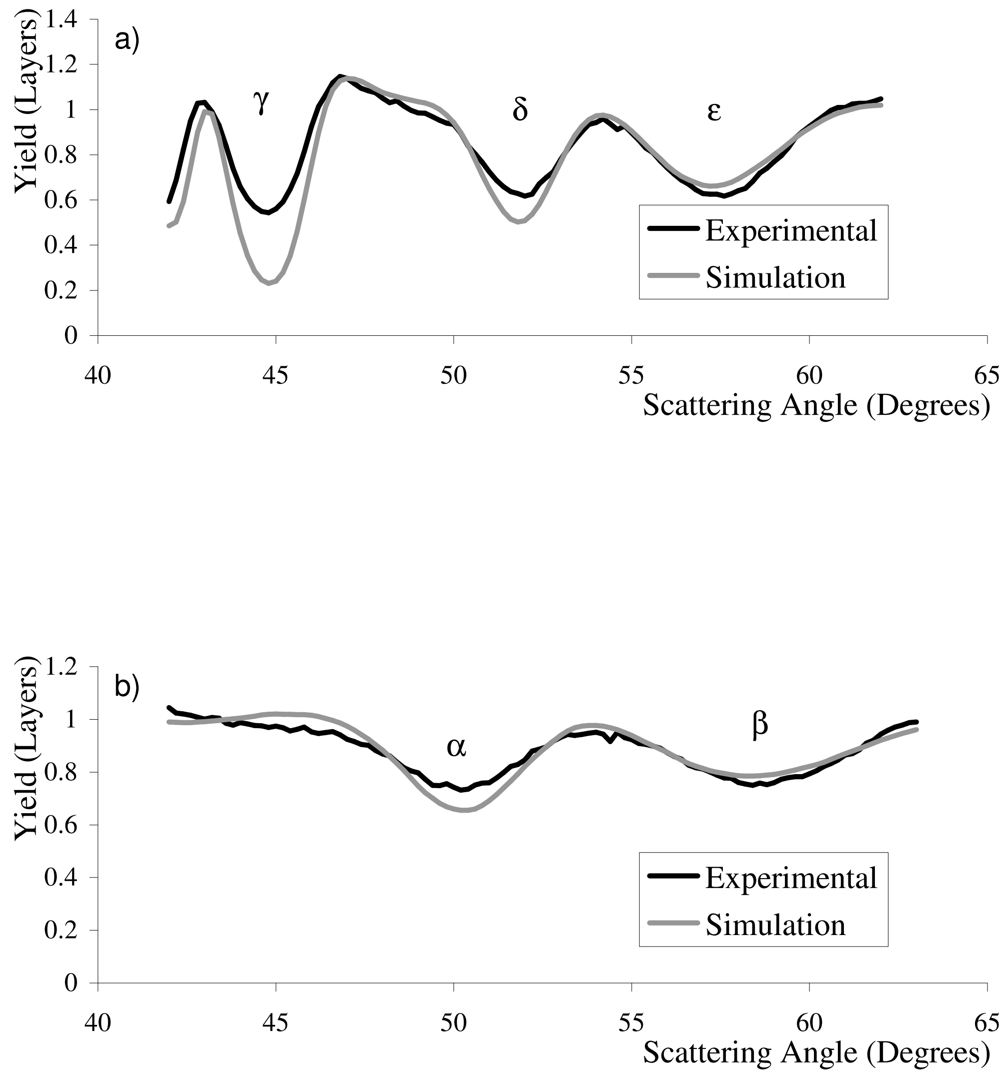

Figure 4.8: Comparison between experimental data and the simulated scattering curve for the final model for two-dimensional Tm silicide (again corrected for Rutherford scattering cross-section). The experimental yield is freely scaled to the simulation. (a) [$\bar{1}$ 00]/[$\bar{1}$ 11] (b) [1$\bar{1}$ $\bar{1}$]/[100]. The ~57° (ε) dip position is now visually a better fit.

	Si_1–Tm (Å)	Si_2–Tm (Å)	Si_1–Si_2 (Å)
Vertical Distance	2.66 ± 0.02	1.80 ± 0.02	0.86 ± 0.03
Bond Length	N/A	2.86 ± 0.02	2.38 ± 0.02

Table 4.2: Structural parameters for the final model for 2D Tm silicide.

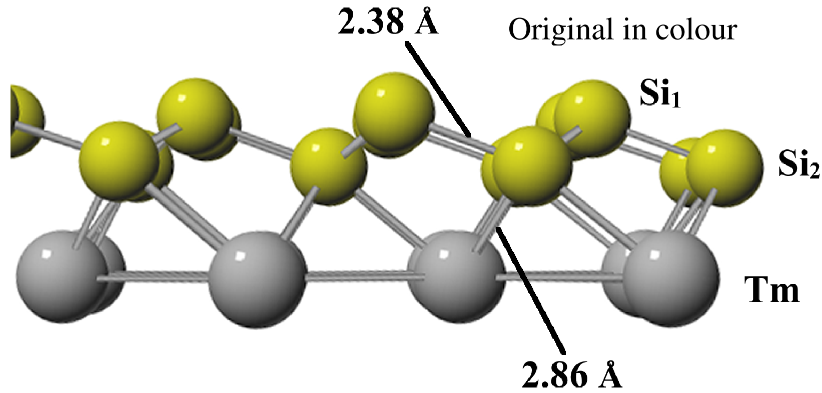

Figure 4.9: Ball and stick representation of the Tm 2D silicide surface, showing the bond lengths of Table 4.2.

visually much better fitted whilst other features seem to be reproduced as comparatively well as before. The structural parameters for this final model are given in Table 4.2 and shown in Figure 4.9.

The re-examination of the model fitting process has resulted in an upward movement of Si_2 compared with the initial result. It should also be noted that the two structures derived are within experimental error of each other. The structural parameters determined are comparable to those known for other two-dimensional rare-earth silicides [5, 8-13]. The Si–Si bond of the top bilayer represents a slight expansion compared with the bulk Si value of 2.35 Å whereas the Si–Tm bond length represents a significant contraction from the bulk value of 2.98 Å. Further discussion of the relationship between these structural parameters and those of other 2D silicides may be found in the next chapter.

The quantitative fit of the simulated scattering curve to the experimental data has been improved by the procedure described above. However, a close examination of the multiple simulations reveals it is still possible to achieve a slightly better

qualitative fit. By closely comparing the angular position of the minima of the major blocking dips in the experimental data and simulations, a further structural model was arrived at (in this procedure it was noted that from geometrical considerations the δ and ε dips are essentially independent of one another, as are the α and β dips, so each could be fitted separately. The change in structural model actually has very little affect on the angular position of the γ dip, which was therefore to some extent neglected) . The data–simulation comparison for this model is shown in Figure 4.10. The structural parameters are summarised in Table 4.3. It is difficult to estimate an error from such a subjective “by eye” fitting procedure. Those quoted are based on a consideration of the step size in the change of each parameter within the simulations and a subjective judgement as to when the fit becomes poor. Although the position of the Si_2 atoms differs slightly between the best by eye fit and the refined structural solution, the bond lengths are identical to within the precision possible with this technique. Further discussion of “by eye” fitting of 2D silicide models for other rare earth metals may be found in the next chapter.

4.4 Conclusion

It has been seen that depositing one monolayer of Tm onto the clean Si (111) 7×7 reconstruction and annealing to around 500 ˚C produces a reconstruction of the surface. This reconstruction results in a 1×1 LEED pattern. Medium energy ion scattering data have been taken from the surface and a structural analysis performed. The structure is seen to be extremely similar to that of other “two-dimensional “ rare earth silicides, as was expected. The structural analysis has shown some possible failings in the reliance upon the χ^2 R-factor for guidance in comparing experimental data to simulations of multiple trial models. These problems are discussed more fully in the next chapter. Despite this, Monte Carlo simulations of ion scattering from the final model show good agreement with the experimental data for both scattering geometries used. A structural model has been proposed based upon this.

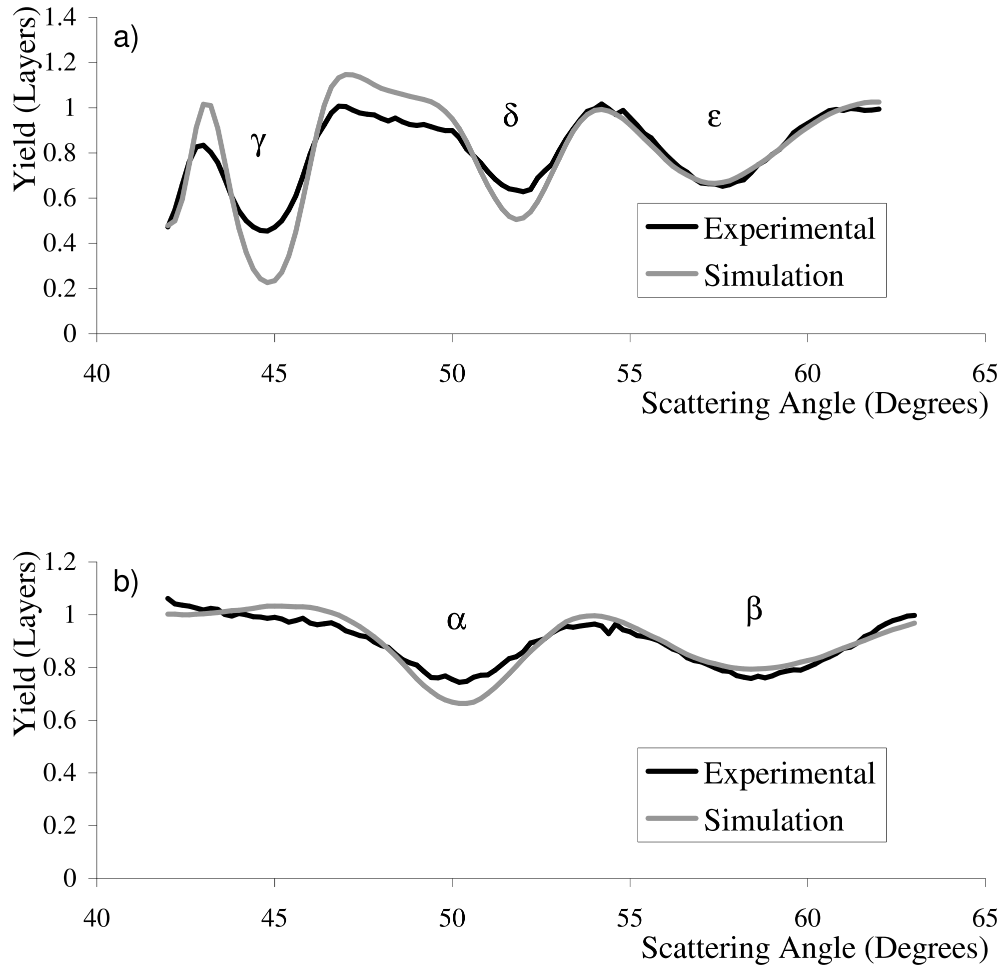

Figure 4.10: Comparison between experimental data and simulation for the "by eye" fit, corrected for Rutherford scattering cross-section. (a) [$\bar{1}$ 00]/[$\bar{1}$ 11] (b) [1$\bar{1}$ $\bar{1}$]/[100]. The ~57° (ε) dip position has been further improved.

	Si_1–Tm (Å)	Si_2–Tm (Å)	Si_1–Si_2 (Å)
Vertical Distance	2.66 ± 0.03	1.81 ± 0.04	0.85 ± 0.04
Bond Length	N/A	2.86 ± 0.02	2.38 ± 0.02

Table 4.3: Structural parameters determined from a "by eye" fit.

References

1. J. A. Knapp and S. T. Picraux, *Appl. Phys. Lett.* **48** 466 (1986)

2. A. Travlos, N. Salamouras and N. Boukos, *J. Appl. Phys.* **81** 1217 (1997)

3. C. Wigren, J. N. Andersen, R. Nyholm and U. O. Karlsson, *J. Vac. Sci. Technol. A* **11** 2665 (1993)

4. D. P. Spence and S. P. Tear, *Personal Communication* (2001)

5. D. J. Spence, S. P. Tear, T. C. Q. Noakes and P. Bailey, *Phys. Rev. B* **61** 5707 (2000)

6. VEGAS, *FOM Institute*

7. D. P. Woodruff and T. A. Delchar, *Modern Techniques of Surface Science*, Cambridge University Press (1986)

8. M. H. Tuilier, P. Wetzel, C. Pirri, D. Bolmont and G. Gewinner, *Phys. Rev. B* **50** 2333 (1994)

9. C. Bonet, D. J. Spence and S. P. Tear, *Surf. Sci.* **504** 183 (2002)

10. C. Rogero, C. Polop, L. Magaud, J. L. Sacedón, P. L. de Andrés and J. A. Martín-Gago, *Phys. Rev. B* **66** 235421 (2002)

11. D. J. Spence, T. C. Q. Noakes, P. Bailey and S. P. Tear, *Surf. Sci.* **512** 61 (2002)

12. M. Lohmeier, W. J. Huisman, G. ter Horst, P. M. Zagwijn, E. Vlieg, C. L. Nicklin and T. S. Turner, *Phys. Rev. B* **54** 2004 (1996)

13. H. Kitayama, S. P. Tear, D. J. Spence and T. Urano, *Surf. Sci.* **482-485** 1481 (2001)

Chapter 5
Structural Trends and the Influence of R-factors

5.1 Introduction

As mentioned in Chapter 4, a large number of studies of rare earth two dimensional silicides have now been published. This gives the opportunity to study the structural parameters (i.e. the RE–Si and Si–Si bond lengths) as a function of the rare earth. By doing so it may be possible to establish structural trends and similarities across the lanthanide series.

An examination of bulk rare earth silicides and the rare earth metals themselves reveals that one might well expect a trend to be apparent in some of the structural parameters of the 2D silicides. The Si–RE bond length in bulk rare earth silicides, $RESi_{\sim 1.7}$, has been shown to decrease as the mass of the rare earth increases [1]. Within the rare earth metals themselves there is a trend towards a decreasing atomic radius across the series [2]. These trends are summarised in Figure 5.1.

The trends mentioned above might suggest that a trend would be observed in the bond lengths of 2D RE silicides. On the other hand, the two dimensional rare earth silicides are known to be electronically similar [3-6]. As the Si_1–Si_2 bond essentially just involves charge transfer from the RE, it might therefore be expected that this bond will remain fairly constant across the series. An examination of any trends it is possible to derive from published results and re-examination of data is presented below.

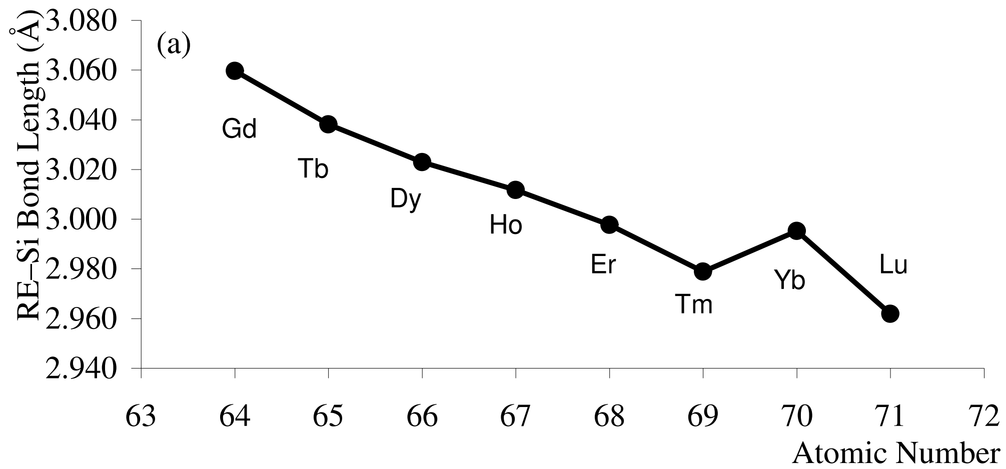

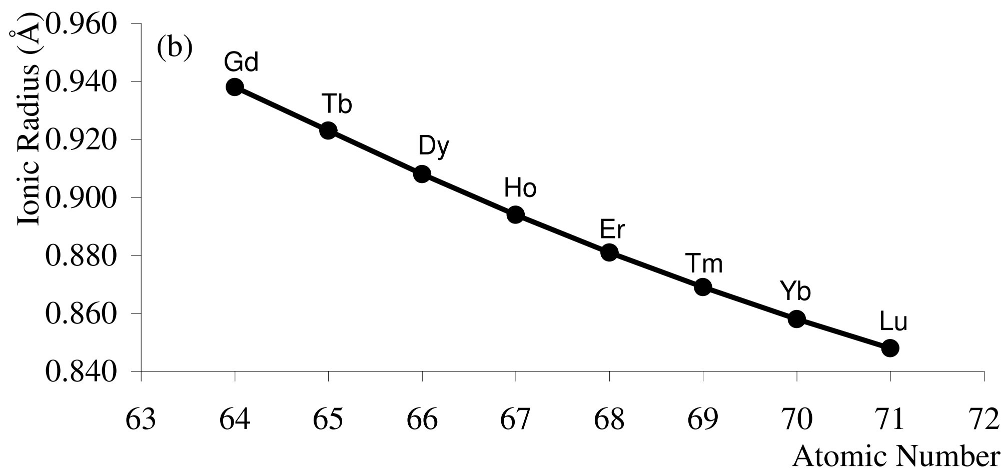

Figure 5.1: (a) RE–Si bond lengths in bulk rare earth silicides. (b) Ionic radii of rare earth metals. Both show a decreasing trend across the series.

5.2 A Possible Trend

Spence *et al*. [7] have previously mentioned the possibility of a trend in the structural parameters of 2D rare earth silicides. At the time there was only a limited set of data, crystallographic information being available for only the 2D silicides of Ho, Dy and Er. Table 5.1 collates all published crystallographic data for 2D RE silicides to date. As can be seen the data set available has been increased to include most trivalent rare earths.

As most of the studies have been by means of MEIS it is informative to directly compare the results from these studies. This also avoids any systematic variations due to the differences between techniques. Figure 5.2 and Figure 5.3 show a comparison of the experimental RE signals from MEIS double alignment scattering experiments for all the RE studies in which the author had access to the data, including the Tm 2D silicide described in the previous chapter. The scattering curves have been corrected for mechanical offset of the analyser and for the Rutherford scattering cross section as described

Rare Earth	Vertical Distance (Å)			Bond Length (Å)		Technique
	Si_1-Si_2	Si_2-RE	Si_1-RE	Si_1-Si_2	Si_2-RE	
Y [8]	0.79 ± 0.04	1.85 ± 0.04	2.64 ± 0.06	2.35 ± 0.01	2.89 ± 0.03	LEED
Y [8]	0.74	1.77	2.51	2.34	2.84	DFT
Gd [9]	0.90 ± 0.02	1.86 ± 0.02	2.76 ± 0.02	2.39 ± 0.01	2.89 ± 0.01	MEIS
Dy [7]	0.85 ± 0.04	1.83 ± 0.03	2.68 ± 0.03	2.37 ± 0.02	2.87 ± 0.03	MEIS
Dy [10]	0.79 ± 0.03	1.90 ± 0.03	2.69 ± 0.04	2.35 ± 0.01	2.92 ± 0.02	LEED
Ho [11]	0.88 ± 0.04	1.80 ± 0.03	2.68 ± 0.03	2.39 ± 0.03	2.86± 0.03	MEIS
Ho [12]	0.82	1.88	2.70	2.36	2.91	LEED
Er [11]	0.92 ± 0.04	1.77 ± 0.03	2.69 ± 0.03	2.40 ± 0.03	2.83 ± 0.03	MEIS
Er [13]	0.82 ± 0.08	1.78 ± 0.08	2.60 ± 0.08	2.36 ± 0.03	2.84 ± 0.05	SXRD
Er [13]	0.80 ± 0.06	1.82 ± 0.06	2.62 ± 0.05	2.36 ± 0.02	2.87 ± 0.04	MEIS
Er [14]	0.90 ± 0.14	1.80 ± 0.10	2.70 ± 0.10	2.39 ± 0.05	2.86 ± 0.06	AED
Er [15]	0.78 ± 0.07	1.92 ± 0.05	2.70 ± 0.05	2.35 ± 0.02	2.93 ± 0.05	SEXAFS
Tm (This work)	0.86 ± 0.04	1.80 ± 0.03	2.66 ± 0.03	2.38 ± 0.02	2.86 ± 0.02	MEIS

Table 5.1: Published structural results for two-dimensional rare earth silicides. Refer to Figure 4.1 for atomic labels. Techniques other than MEIS show a longer Si_2–RE bond length for a given rare earth.

Original in colour

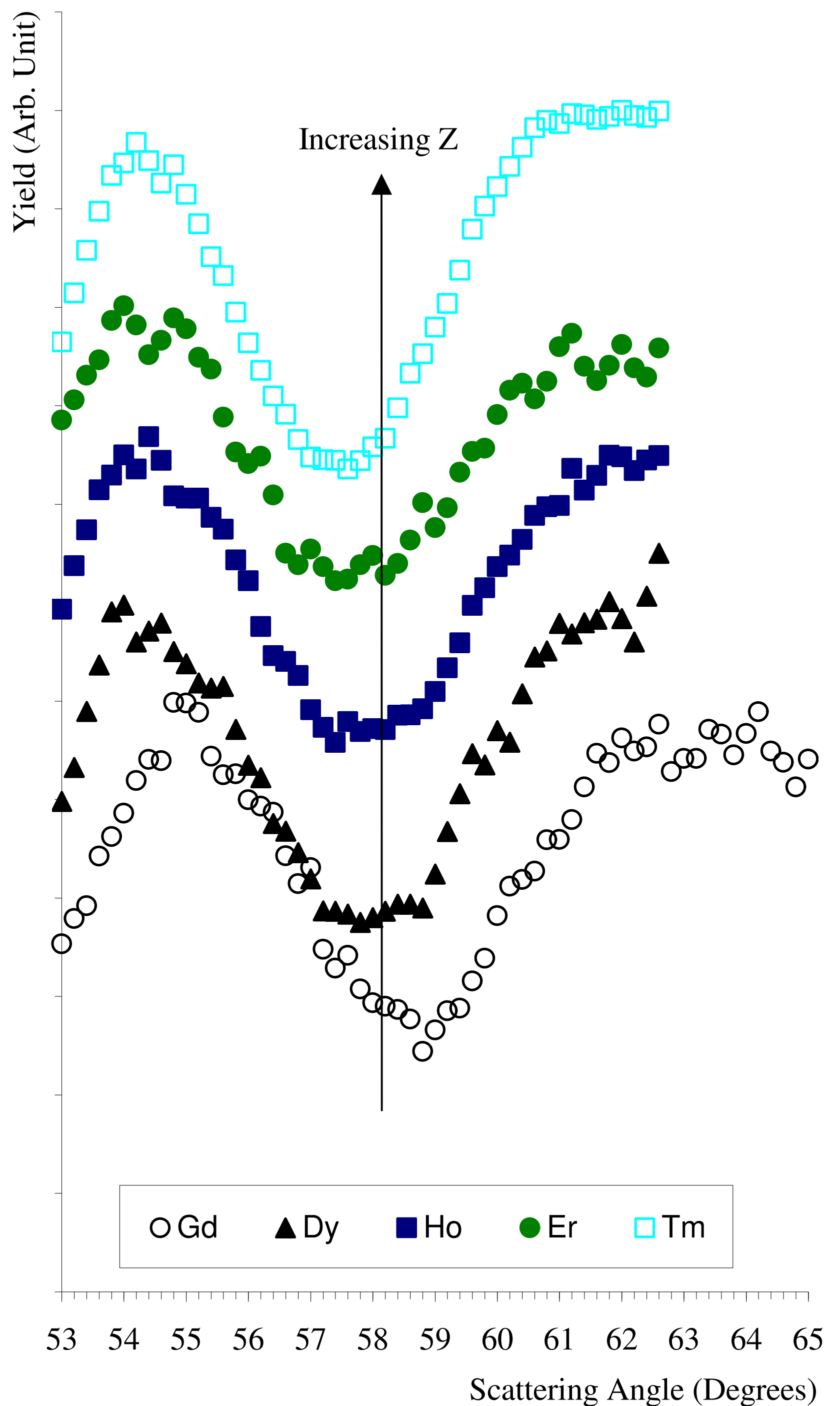

Figure 5.2: Comparison of experimental MEIS scattering curves for 2D rare earth silicides. This feature is due to the blocking of scattered ions by the Si_2 atoms and directly reflects the Si_2–RE bond length (the blocking dip labelled ε in the previous Chapter). Curves have been scaled to an arbitrary yield and then offset for clarity.

Original in colour

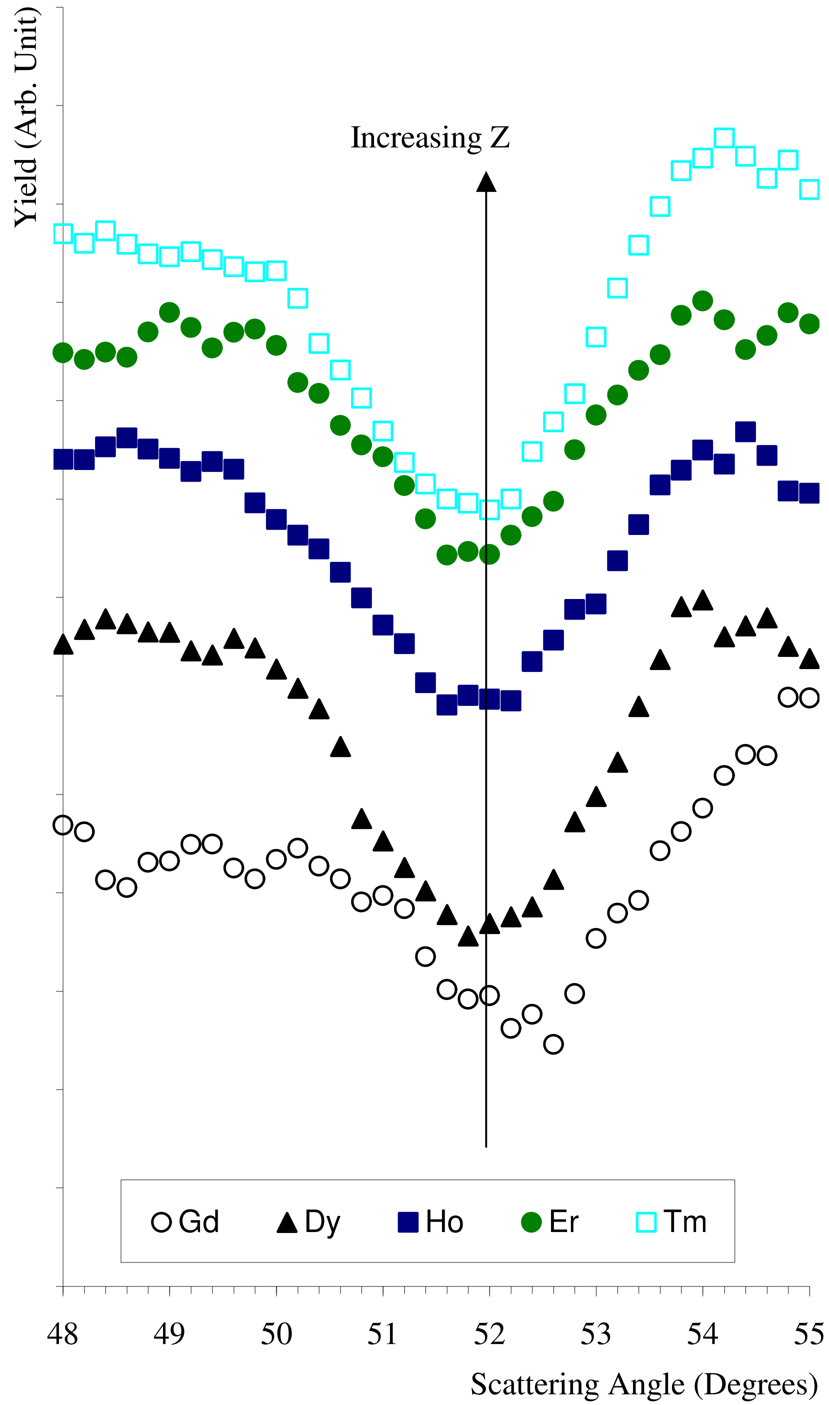

Figure 5.3: Comparison of experimental MEIS data for 2D rare earth silicides. The blocking dip shown is due to blocking of scattered ions by the Si_1 atoms (the blocking dip labelled δ in the previous Chapter). Curves have been scaled to a common arbitrary yield and then offset for clarity.

in Chapter 4. The curves have been scaled to a common yield, then each has been offset by a fixed amount for clarity. The blocking dip shown in Figure 5.2 is caused by scattered ions being blocked by the Si_2 atoms (refer to Chapter 4 for atomic labels). There is a clear trend in the angular position of the blocking dip as the rare earth mass increases. This shift in blocking dip position represents a change in the Si_2–RE vertical distance and therefore a change in the bond length. The decreasing scattering angle with increasing atomic number corresponds to a decreasing bond length. This trend is partially evident in the published data (highlighted results in Table 5.1). The Tm result shows a discrepancy with the trend, which is discussed below. Figure 5.3 shows the blocking dip caused by scattered ions being blocked by the Si_1 atoms. The position of this blocking feature is therefore indirectly related to the Si_1–Si_2 bond length.

5.3 The Possible Influence of the R-factor

As mentioned above, the results from the Tm data presented in the previous chapter do not fit with the trend seen in the structural parameters of other known 2D rare earth silicides. It may also be recalled from the previous chapter that the initial results for the Tm silicide were revised due to the R-factor analysis being overly influenced by one blocking feature. This caused the initially arrived at Si_2–Tm bond length to be revised upwards. If such an effect were present in the other 2D silicides then the Tm data may be found to match the trend in bond lengths.

Further indication that the previous MEIS results for 2D rare earth silicides may have been unduly influenced by the R-factor comes from a simple geometric consideration of the scattering angle at which the blocking dip occurs. A simple calculation based only on the scattering geometry leads to the Si_2–RE bond lengths given in Table 5.2. The published results described in Table 5.1 are shown for comparison. This calculation suggests that the published result for all but the Si_2–Tm bond length is actually too small (though the errors in the geometric calculation are of course quite large, there is a consistent indication of

Rare Earth	Calculated Si_2–RE Bond Length (Å)	Published Bond Length (Å)
Gd	2.95 ± 0.04	2.89 ± 0.01 [9]
Dy	2.91 ± 0.04	2.87 ± 0.03 [7]
Ho	2.90 ± 0.04	2.86 ± 0.03 [11]
Er	2.90 ± 0.04	2.83 ± 0.03 [11]
Tm	2.87 ± 0.04	2.86 ± 0.02 (This work)

Table 5.2: Bond lengths calculated from purely geometrical considerations (i.e. the measured angular position of the relevant blocking dip). Also shown for comparison are the published bond lengths.

a longer Si_2–RE bond length).

For 2D rare earth silicide systems where both MEIS and another technique have been used to quantitatively study the same system (the LEED studies of Dy [10] and Ho [12] and the various studies of Er [13-16]) the other techniques all indicate a longer Si_2–RE bond length than that obtained from MEIS, again pointing towards the fact that the MEIS analysis is under estimating this value. Note that the Si_1–Si_2 bond length is in general shorter in the other studies than that obtained from MEIS. Due to the nature of the MEIS analysis, which relates the vertical distance of the Si atoms relative to the RE, this is also consistent with the position of Si_2 being incorrectly determined. In effect the position of Si_2 should be higher than indicated by the MEIS studies, which would result in a lengthening of Si_2–Re bond and shortening of Si_1–Si_2 bond.

In the light of the above observations it seems that some further analysis of previously studied 2D rare earth silicides and of R-factors is necessary. The author has performed such an analysis, the results of which are now presented.

5.4 Re-examination of MEIS Structural Results

In Chapter 4 it was seen how a much better qualitative agreement between simulation and experiment could be achieved by excluding the lowest angle blocking dip in the $[\bar{1}00]/[\bar{1}11]$ geometry from the R-factor analysis. In order to

Rare Earth	Revised χ-Squared		By Eye	
	Si_1–Si_2 Bond Length (Å)	Si_2–RE Bond Length (Å)	Si_1–Si_2 Bond Length (Å)	Si_2–RE Bond Length (Å)
Gd	2.36 ± 0.02	2.93 ± 0.02	2.36 ± 0.02	2.93 ± 0.03
Dy	2.36 ± 0.02	2.89 ± 0.02	2.36 ± 0.02	2.90 ± 0.03
Ho	2.37 ± 0.02	2.87 ± 0.02	2.36 ± 0.02	2.90 ± 0.03
Er	2.38 ± 0.02	2.86 ± 0.02	2.37 ± 0.02	2.88 ± 0.03
Tm	2.38 ± 0.02	2.86 ± 0.02	2.38 ± 0.02	2.86 ± 0.03

Table 5.3: Revised structural parameters for 2D rare earth silicides and the corresponding subjective "by eye" fits. A general trend for a decrease in the Si_2–RE bond length with increasing atomic number emerges.

establish that this feature has skewed previous MEIS results to a too low Si_2–RE bond lengths, the data to which the author has access have been reanalysed. A procedure similar to that used for the Tm silicide was used, comparing the existing simulations to the experimental data using a χ^2 R-factor excluding the lowest blocking dip from the calculation of the R-factor. The bond lengths thus obtained are indeed longer than those quoted in the literature. The newly revised structural parameters are given in Table 5.3. A subjective "by eye" fit (in which the angular position major blocking dips minima were subjectively fitted) was also performed, the results of which are also given in Table 5.3. Some confidence in the ability to fit such data by eye may be gained by considering not the bond lengths but the Si_1–RE vertical distances. It is this quantity which is directly measured by the MEIS scattering curves, being given directly by the position of the δ blocking dip. The vertical separation of Si_1–RE for the original published results, the revised results and the by eye fits are shown in Table 5.4. This shows that the fitting of this lower angle blocking dip is not affected by the same issues as the fitting of the higher angle dip (see below for further discussion of these issues) and one may therefore "trust" the R-factor result, which shows almost no change between the published and revised results. The by eye fit is in very good agreement with these results, which demonstrates that it is possible to subjectively fit a blocking dip of this nature. The two blocking dips (δ and ε) are quite similar in form and so it is reasonable to also employ a subjective fitting of

Si_1–RE vertical separation (Å)			
Rare Earth	Published Result	Revised Result	By Eye Fit
Gd	2.76	2.74	2.74
Dy	2.68	2.67	2.66
Ho	2.68	2.67	2.66
Er	2.69	2.67	2.67
Tm	2.66	2.66	2.66

Table 5.4: Vertical separations between the Si_1 and RE atoms as found in the original published results, from a revised study of the data and from fitting by eye. The by eye results show that it is possible to subjectively fit blocking dips of this form.

the higher angle dip. It should be noted that it is once again the unusual independence of the blocking features in question which allows for such objective fitting.

The new bond lengths found by the revised study of the data and the by eye fitting are in better agreement with those derived from other techniques. A clear general trend is evident for the Si_2–RE bond length to decrease as the mass of the rare earth increases. The Si_1–Si_2 bond length remains approximately constant across the series.

5.5 Examining the R-Factor

5.5.1 The Influence of the Low Angle Blocking Dip

The influence of the lowest angle blocking dip within the $[\bar{1}00]/[\bar{1}11]$ geometry in determining the best fit structural solution using a χ^2 R-factor comparison of simulation and experiment is readily demonstrable. Figure 5.4 shows the comparison between simulation and experiment for the structural solution determined using the R-factor (over the entire angular range) in the case of Tm 2D silicide (see Chapter 4 for a discussion of this system). Also shown on the graph is the contribution to the total R-factor from each angular point (0.2° apart). The lowest angle blocking dip can clearly be seen to provide the largest

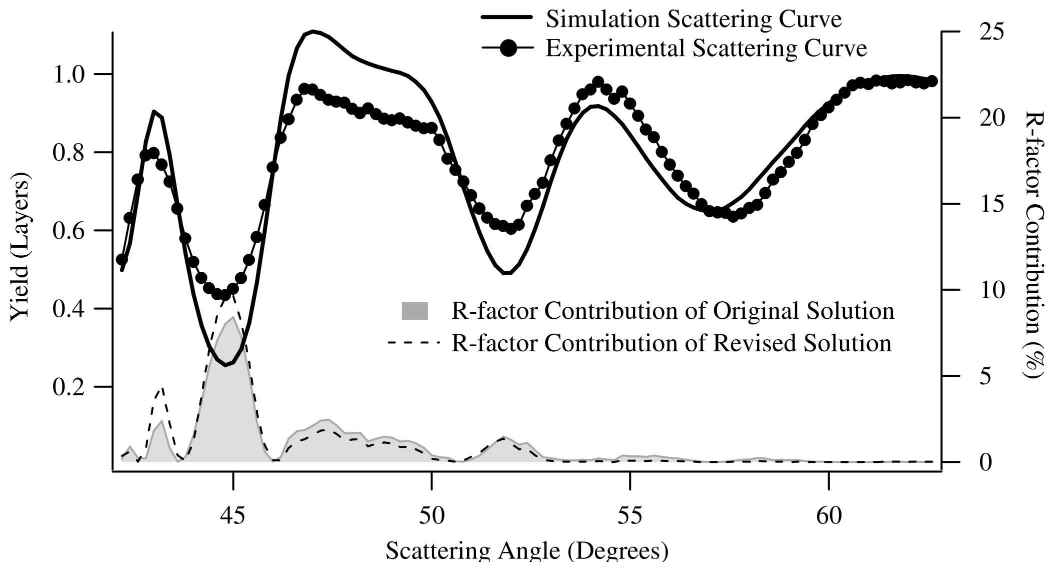

Figure 5.4: Contribution of each point to the total R-factor. Note the significance of the lowest angle dip. The dashed line shows similar contributions for the simulation of the final solution.

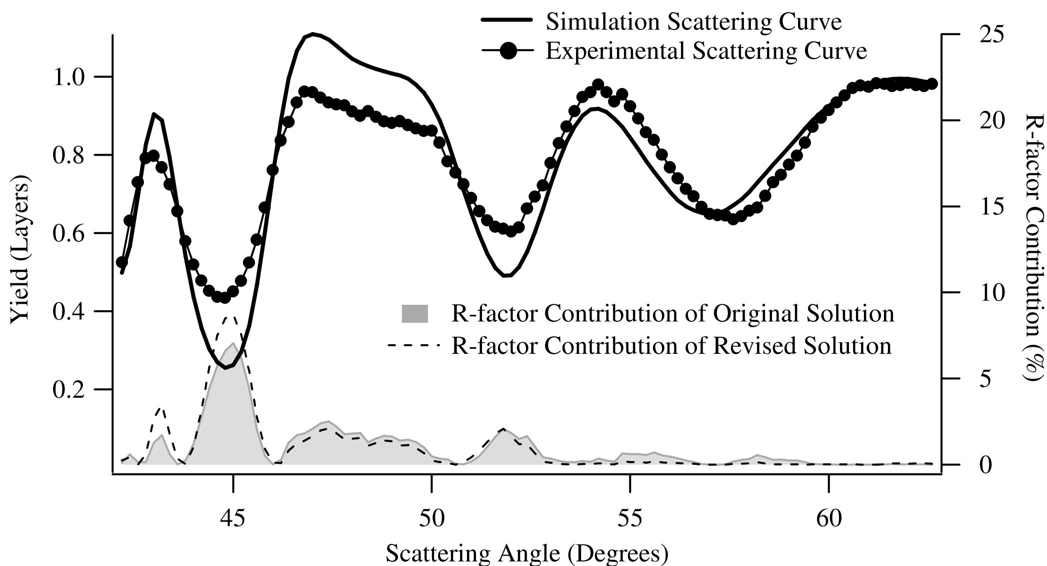

Figure 5.5: Contribution of each point to the total R-factor when the Rutherford scattering cross section is not taken into account. This eliminates the added weight given to lower angles due to the additional number of counts. The depth of the lowest angle dip is still the most important factor.

contribution. Furthermore, the dashed line shows the contribution to the R-factor from each point for the comparison to the simulation of the final solution. This clearly indicates that it is the difference in contribution due to the lowest angle dip which is having the greatest influence.

The χ^2 R-factor, i.e.

$$R_{\chi} = \frac{1}{N}\sum_{n=1}^{N}\frac{\left(Y_{exp} - Y_{sim}\right)^2}{Y_{exp}} \tag{5.1}$$

gives most weight to points at which the yield is highest. When calculating the R-factor the fall off in counts due to the Rutherford scattering cross section is reintroduced. This results in the lower angles having a higher yield than higher angles and thus contributing proportionately more to the R-factor. While there is a good argument that this practice is indeed correct as the original data contained less counts at higher scattering angle and therefore must be less statistically significant at higher angles, it is an obvious exercise to recalculate the R-factor without this correction. This might be expected to reduce the significance of the lowest angle blocking dip and therefore improve the performance of the R-factor.

Such a comparison is shown in Figure 5.5. The structural solution chosen by the R-factor does not change, and the R-factor is still dominated by the lowest angle dip.

In fact the χ^2 R-factor is being influenced by the large difference in simulated and experimental yield around the lowest angle dip. This results in it discounting most of the structural information contained in the position and shape of all the other dips. Eliminating the lowest angle dip from the calculation of the R-factor produces contributions as shown in Figure 5.6.

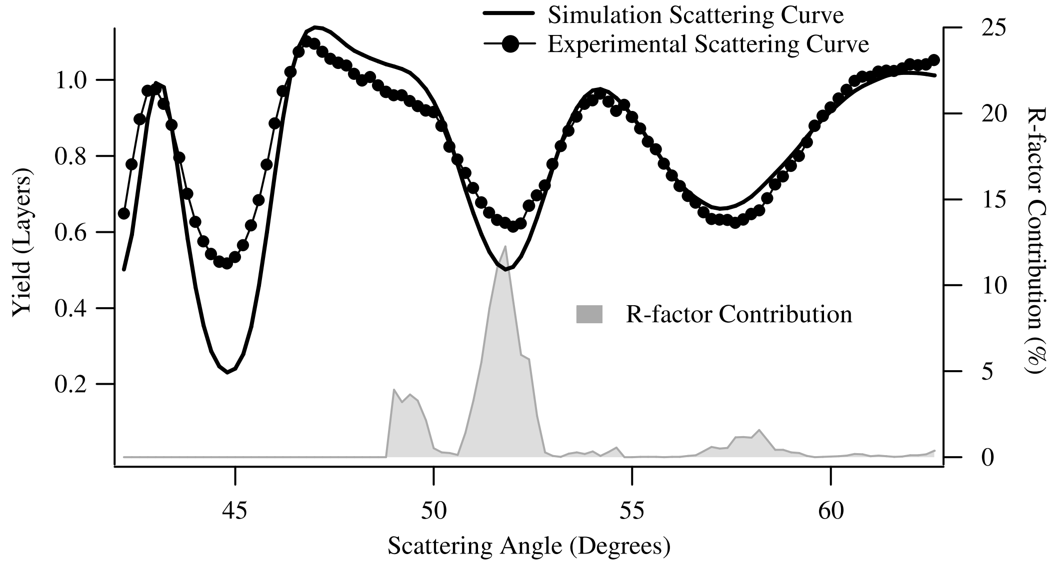

Figure 5.6: Contributions to the R-factor when discounting the lowest angle dip from the calculation of the R-factor. This produces a much better fit to the higher angle dips than that shown in Figure 5.4 and Figure 5.5.

5.5.2 Alternative R-Factors

Numerous R-factors have in the past been applied to the comparison of theoretical and experimental scattering curves in MEIS. Noakes *et al.* [17] have previously compared several different R-factors in determining a structural solution to the Ni(100)c(2 × 2)-O system. They found that for that system at least any of the R-factors could be used to successfully identify a consistent structure. As well as R_χ they examined

$$R_{IS} = \frac{100}{N}\left[\sum_{i=1}^{N}\left(\frac{Y_{exp} - Y_{sim}}{Y_{exp}}\right)^2\right]^{1/2}, \tag{5.2}$$

$$R_P = \frac{\sum_{i=1}^{N}\left(y_{exp} - y_{sim}\right)^2}{\sum_{i=1}^{N}\left(y_{exp}^2 + y_{sim}^2\right)} \tag{5.3}$$

and

$$R_m = \frac{\sum_{i=1}^{N}(\chi_{exp} - \chi_{sim})^2}{\sum_{i=1}^{N}(\chi_{exp}^2 + \chi_{sim}^2)} \tag{5.4}$$

R_{IS} is, like R_χ, sensitive to the absolute yields of the simulated and experimental curves as well as the position of blocking features. R_{IS} and slight variants upon it have been used with some success in a number of MEIS studies [18-21]. R_P, on the other hand, is the Pendry R-factor widely used in LEED [22]. In this R-factor, *y* is the logarithmic derivative of the intensities. Sensitivity to absolute yields is hence completely removed for well separated features and the R-factor is only sensitive to positions.

Finally R_m comes from the field of photoelectron diffraction. It is similar in form to Pendry's R-factor, with the term χ being given by

$$\chi = (Y - Y_0)/Y_0 \tag{5.5}$$

Y_0 being a smooth spline which passes through the curve to be fitted. R_m thus has the advantage of being sensitive to both peak position and the absolute values of the intensity modulations but not to the intensities themselves.

These R-factors have been used to compare the experimental 2D rare earth silicide data to the Monte Carlo simulations. Two other R-factors have also been tested. The first of these is actually Pendry's R-factor but applied to data which has first been "flipped" (i.e. performing the conversion $Y_{flip} = Y_{max} - Y$), hereafter R_{Pflip}. This is more consistent with the type of data with which the R-factor is designed to deal, which is assumed to be a series of Lorenzian peaks. Indeed for some MEIS data this flipping has been seen to produce curves which are visually indistinguishable from those obtained from LEED *I–V*, though in the case of 2D rare earth silicides the effect is less dramatic.

The second R-factor attempts to produce an algorithm close to a naive "by eye" examination. The angular position of the minima within the experimental and simulated scattering curves are found and the R-factor taken to be

$$R_{min} = \sum_{i=1}^{M} \left(\theta_{sim} - \theta_{exp}\right)^2 \qquad (5.6)$$

M being the number of minima found and θ the angle at which the minimum occurs. This is somewhat similar to some R-factors which have been used in LEED, where the energy difference in peak positions was employed [23]. It suffers the same disadvantages, namely a disregard for intensity and ambiguities relating to the number of dips and which simulated dip matches which experimental dip. However, for a case such as the present, where the sequence of simulations produce similar intensities and number of dips and it is generally only the position of those dips which is changing, then it may be a useful tool in the determination of the correct structure.

5.5.3 Performance of the R-factors

The results of comparisons using each of these R-factors are summarised in Table 5.5. Some additional remarks should be noted, particularly in the case of the Pendry R-factors. One important parameter in the calculation of the Pendry R-factor is the imaginary part of the electron self energy, V_{oi}. This parameter is related to the width of the peak by $\Delta E = 2\,|V_{oi}|$, where ΔE is the half width half maximum (HWHM). In LEED $|V_{oi}|$ is known to be around 4 eV. For application to MEIS it would seem sensible to choose a value equal to half the average width of a blocking dip. Given Equation 3.12 for the width of a blocking dip,

$$\psi = 4\left(\frac{A}{Es}\right)^{1/2} \qquad (5.7)$$

and taking a value for the distance between scattering, and blocking ion consistent with published structural parameters for rare earth silicides, one

Rare Earth	Bond	R_χ	R_χ Refined	R_{IS}	R_m	R_P (V_{oi}=1.5)	R_P (V_{oi}=7.5)	R_{Pflip}	R_{min}	"By Eye"
Gd	Si_1–Si_2 (Å)	2.39 ± 0.01	2.36 ± 0.02	2.40 ± 0.02	2.40 ± 0.02	2.39 ± 0.02	2.37 ± 0.02	2.36 ± 0.02	2.36 ± 0.02	2.36 ± 0.02
	Si_2–RE (Å)	2.89 ± 0.01	2.93 ± 0.02	2.89 ± 0.03	2.91 ± 0.03	2.95 ± 0.03	2.92 ± 0.03	2.92 ± 0.03	2.93 ± 0.03	2.93 ± 0.03
Dy	Si_1–Si_2 (Å)	2.37 ± 0.02	2.36 ± 0.02	2.39 ± 0.02	2.40 ± 0.02	2.37 ± 0.02	2.36 ± 0.02	2.35 ± 0.02	2.37 ± 0.02	2.36 ± 0.02
	Si_2–RE (Å)	2.87 ± 0.03	2.89 ± 0.02	2.86 ± 0.03	2.84 ± 0.03	2.90 ± 0.03	2.90 ± 0.03	2.90 ± 0.03	2.89 ± 0.03	2.90 ± 0.03
Ho	Si_1–Si_2 (Å)	2.39 ± 0.03	2.37 ± 0.02	2.39 ± 0.02	2.37 ± 0.02	2.35 ± 0.02	2.35 ± 0.02	2.35 ± 0.02	2.36 ± 0.02	2.36 ± 0.02
	Si_2–RE (Å)	2.86 ± 0.03	2.87 ± 0.02	2.85 ± 0.03	2.86 ± 0.03	2.88 ± 0.03	2.89 ± 0.03	2.89 ± 0.03	2.88 ± 0.03	2.90 ± 0.03
Er	Si_1–Si_2 (Å)	2.40 ± 0.03	2.38 ± 0.02	2.40 ± 0.02	2.40 ± 0.02	2.39 ± 0.02	2.38 ± 0.02	2.35 ± 0.02	2.37 ± 0.02	2.37 ± 0.02
	Si_2–RE (Å)	2.83 ± 0.03	2.86 ± 0.02	2.84 ± 0.03	2.84 ± 0.03	2.85 ± 0.03	2.86 ± 0.03	2.89 ± 0.03	2.87 ± 0.03	2.88 ± 0.03
Tm	Si_1–Si_2 (Å)	2.39 ± 0.02	2.38 ± 0.02	2.40 ± 0.02	2.39 ± 0.02	2.37 ± 0.02	2.38 ± 0.02	2.37 ± 0.02	2.37 ± 0.02	2.38 ± 0.02
	Si_2–RE (Å)	2.84 ± 0.02	2.86 ± 0.02	2.84 ± 0.03	2.84 ± 0.03	2.86 ± 0.03	2.86 ± 0.03	2.86 ± 0.03	2.86 ± 0.03	2.86 ± 0.03

Table 5.5: Comparison of the best fit models derived from comparing simulated and experimental blocking curves using a variety of R-factors. Also shown are the best subjective visual fits ("By Eye"). A trend in the Si_2–RE bond length is apparent in the results from a number of comparison methods; notably the "by eye" comparison, R_{min}, R_{Pflip} and R_χ-refined.

obtains a width of around 3 ½–6 ˚. There will be some broadening due to thermal effects, so it seems reasonable to accept a value of around 2–3 ˚ for the HWHM (a value consistent with the scattering curves from the rare earth silicides). This gives a value of V_{oi} of 1–1 ½ ˚.

Having performed the above analysis it was found that the Pendry R-factor failed to consistently arrive at a convincing solution for the best fit simulation. Whilst on some occasions the solution would appear to be a good fit, on others a visual inspection immediately revealed that the suggested solution was clearly incorrect. It was discovered, by a trial and error means, that the performance of the Pendry R-factor could be improved by using a value for V_{oi} of 7 ½ ˚. This would imply a HWHM of the blocking dips of around 15 ˚, which can clearly be seen not to be the case by looking at such a blocking dip. Indeed 15 ˚ is over halfthe typical angular range for a scattering curve (the MEIS analyser accepting ions over a scattering window of 27 ˚). There seems to be no physical basis for this choice of V_{oi} and due to the empirical nature of its determination it is possible that further optimisation is achievable. It is likely that the requirement for such a high value of V_{oi} is due to the R-factor attempting to fit Lorentzian peaks to a data set which consists of relatively flat regions and large *dips*. It is also possible that an entirely different value of V_{oi} would be required for use with scattering curves from a different structure. This does not make for a satisfactory R-factor.

The above failings in the Pendry R-factor led to the development of R_{Pflip}, in which the scattering curves are first inverted before calculation of the R-factor. This, at least qualitatively, produces a curve more reminiscent of the LEED *I–V* curves with which the Pendry R-factor has proven a success (see Figure 5.7). The initial estimate for the value of V_{oi} was again used. The “flipped” version of the Pendry R-factor (this is a somewhat misleading term—the R-factor remains the same but the data from which it is calculated has been “inverted”) selected a simulation which was a much better match to the experimental data than its predecessor did. This R-factor did still require some smoothing of the

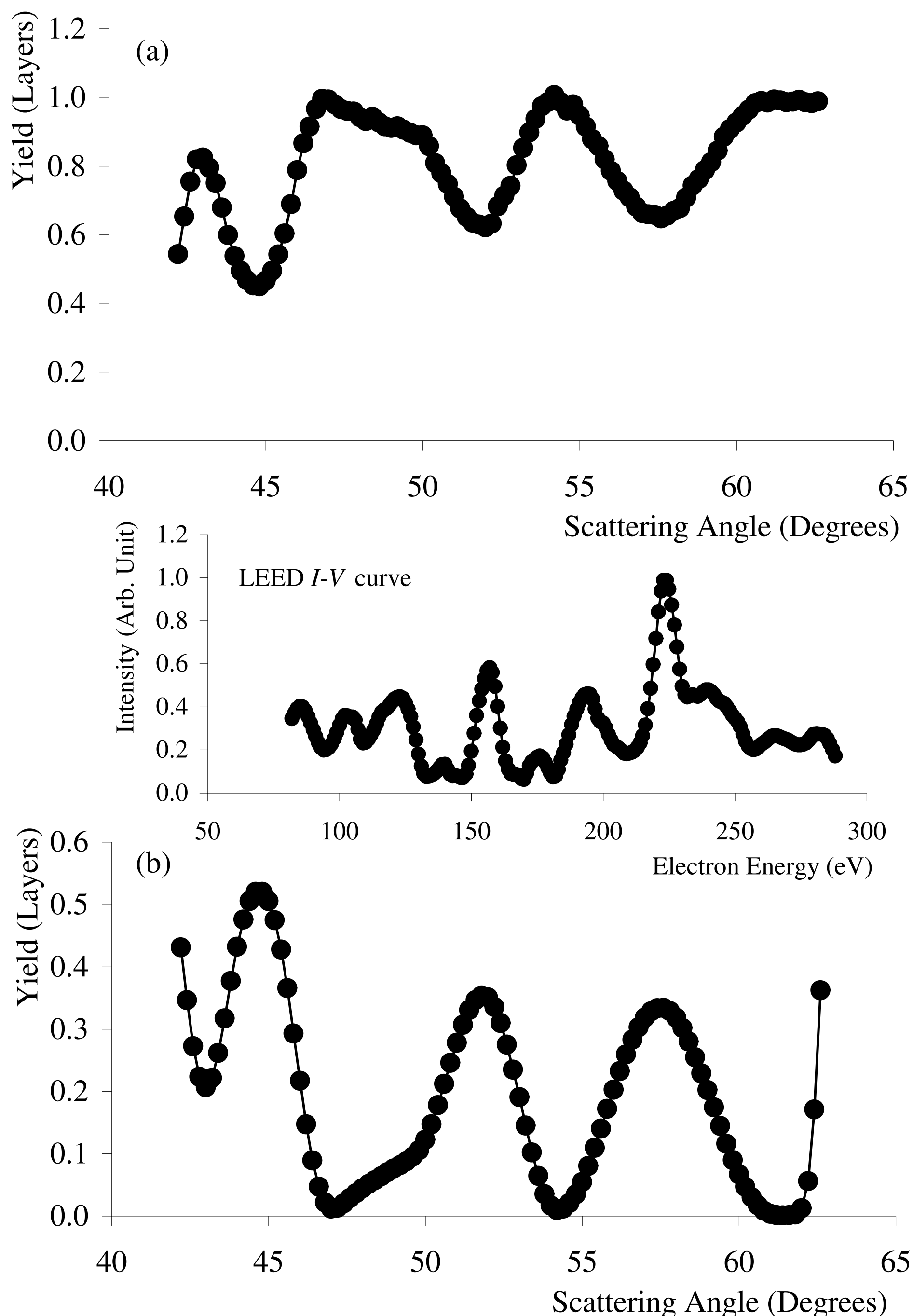

Figure 5.7: Comparison of (a) the original Tm silicide MEIS scattering curve and (b) the "flipped" version. The inset shows a typical LEED I–V *curve* [10]. *The Pendry R-factor was originally designed to deal with peaks rather than dips. The flipped data may be considered qualitatively more like the LEED data for which the Pendry R-factor is standard.*

experimental data in order to reduce the effects of noise but this had been a requirement for the original R_P with V_{oi} = 7.5 as well.

The R-factors R_{IS} and R_m performed poorly. In the case of R_{IS} this is probably due to the same issues observed for R_χ. The performance of R_m may have been influenced by the fit of the smooth spline to the scattering curves. The solutions were as poor a match as those found by the original R_χ and on occasion worse.R_{min} appears to reproduce the process of selecting the best fit model by eye well. However, it seems likely that this R-factor is not very robust when confronted with more complex data sets. It may prove useful in some cases, especially with blocking features which have a single origin.

5.5.4 Errors in the Results

The errors quoted in Table 5.5 deserve some mention. Those for χ^2 R-factors are calculated from Equation 4.2 and are comparable with those in the literature. The errors quoted for the “by eye” fits were estimated as for the case of Tm silicide in the previous chapter, i. e. they are themselves quite subjective but err on the side of caution—it was felt that each parameter could be fitted to within two or three steps of the simulations.

In the case of the Pendry R-factor it is usual in LEED to estimate the error using the variance in the minimum value of the R-factor [22]

$$\mathrm{var}(R_{min}) = R_{min}\sqrt{2/N} \qquad (5.8)$$

(strictly this is a standard deviation but it is common to maintain Pendry’s original nomenclature).

Here, N is the number of pieces of independent information contained within the data. In terms of LEED this is easily given by the number of well separated peaks which could be present. For the Lorentzian peaks involved, the full width half maximum is given by 2 V_{oi}, so well separated peaks occupy an energy width of 4

V_{oi} and N is given by

$$N = E / (4\ V_{oi}) \tag{5.9}$$

where E is the total energy range over which data is taken.

Relating the above to the case of the 2D silicides, Equation 5.9 would imply that for a single geometry (angular range 27 °) N = 4.5 for V_{oi} = 1.5. Over the two geometries available this would then give N = 9.

Another obvious estimate of N, in the case of MEIS, is the number of blocking features actually present (neglecting the fact that the features are not necessarily independent). For the 2D silicides this would give N = 5 for the two geometries available. This value is probably an underestimate as it only counts large blocking features, neglecting more subtle effects, and fails to account for the fact that the absence of a blocking feature may also convey structural information.

From the above arguments it would seem that a value of N in the region of 5–10 is not unreasonable. However, calculations using Equation 5.8 resulted in unrealistically large errors for each structural parameter. This may be related to the fact that in LEED a very small change in the structural model results in large changes in the I–V curves, whereas in MEIS—and especially in the case of 2D silicides—small structural parameter changes have only a small effect on one or two blocking features, which maintain their overall character. The R-factor curve around the minimum R-factor may therefore be expected to be steeper in LEED than MEIS.

The errors quoted for Pendry R-factors are hence not based on a quantitative calculation but rather estimated assuming that the selected model is correct within two steps for each parameter (i.e. the error in parameter a_j was taken to be $2\delta z_j$ where δz_j is the change in a_j between models of the multicalc). It also seems reasonable to assume that the maximum error in using an R-factor guided fit is no greater than that which can be achieved by fitting by eye.

Errors quoted for other R-factors have been estimated in an identical way as for the Pendry R-factors. It is an obvious advantage of the χ^2 R-factor that it offers a quantitative way in which to calculate the error in each parameter. It is felt that this is probably an over estimate of the true error in the results. Ideally the R-factor should distinguish just one structural model as the solution, implying an error of around half the parameter step size. Whilst it is not anticipated that the precision would necessarily be this good in the present case, a more realistic error would probably be something slightly less than those quoted, more reminiscent of those achieved using the revised χ^2 R-factor, i.e. around ± 0.02 Å at worst—at least for those R-factors which appear to perform consistently.

More importantly, a trend in the Si_2–RE bond length does emerge. Although such a trend is seemingly masked by the errors associated with the bond lengths, the weight of evidence points towards it. The trend consistently emerges whichever R-factor is used in the comparison. Further, visually comparing the data to the simulations, a method shown above to be at least partly reliable, and which in this case has possibly the largest over estimate of error, also shows a trend in the bond length. Perhaps the most compelling argument is the obvious visual shift in the position of the blocking dip as demonstrated in Figure 5.2 (and reflected in the geometrical calculations summarised in Table 5.2). Whilst the absolute value of the bond length retains some uncertainty, the author feels justified in a confidence that the bond length does decrease with increasing RE atomic number.

5.5.5 Conclusion

It has been shown that the selection of the best fit structural model based on an R-factor comparison of simulated and experimental blocking curves is, in the case of 2D rare earth silicides, problematic. Although the systems under consideration represent a special, and perhaps unusual case, these difficulties emphasise the importance of vigilance from the experimenter when examining data. Various other R-factors and workarounds have been tried. In the case of the Pendry R-factor improvements have been found by adjusting the data to better

resemble the LEED data that R-factor was designed to work with—this R-factor then gives the best general performance. While no completely satisfactory solution has been found, a combination of R-factors can give some confidence to the result.

5.6 Conclusion

A possible trend in the structural parameters of 2D rare earth silicides has been identified. Problems with the use of a χ^2 R-factor have been seen, which may have affected published results in the past. A variety of other R-factors have been applied to the experimental–simulation comparison, with varying degrees of success. The 2D rare earth silicides result in particularly peculiar MEIS scattering curves, in that the curves exhibit few, well defined blocking dips. This simplicity is thanks to the straight forward scattering and blocking geometries caused by the presence of only a single rare earth layer and the ability to isolate the scattering from this layer due to the mass separation. It might be expected that where the scattering data is more complex, as is the case in most systems, the problems associated with comparisons to model structures for the 2D silicides will not be so apparent. However, it is due to this simple, low number of blocking features that it is also possible to rapidly make a subjective assessment of fit. The R-factors which have been found to perform consistently, including adjustment of the range over which R_χ is calculated, support the conclusion that previous studies have under estimated the length of the Si_2–RE bond whilst over estimating the Si_1–Si_2 bond length (i.e. they have placed the z-position of Si_2 too "low"). This is consistent with results from other techniques such as LEED.

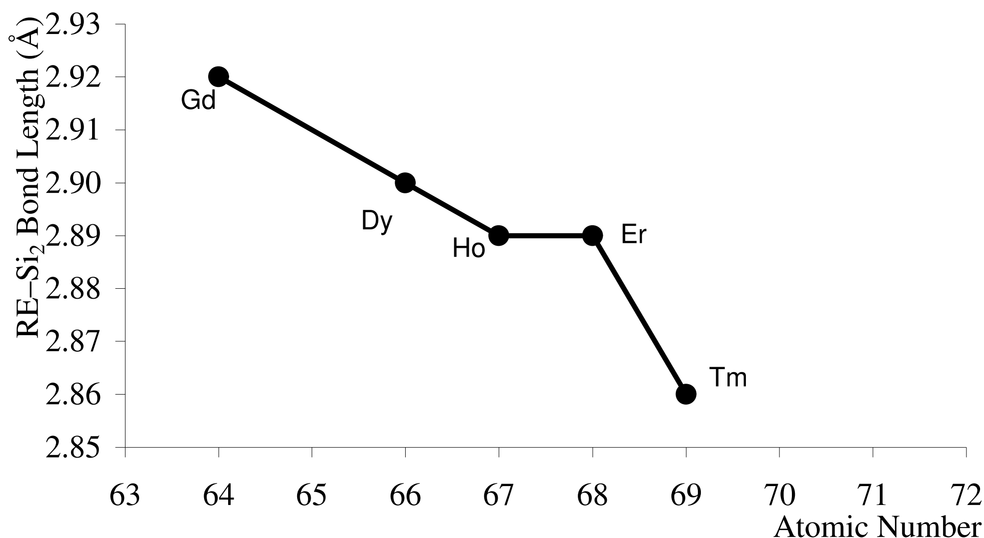

Figure 5.8: The structural trend in the Si_2–RE bond length across the rare earth series. This plot is derived from the structural model determined using R_{Pflip}. Other methods of determining the best fit model show a similar trend.

A trend has emerged for the Si_2–RE bond length to decrease as the mass of the rare earth metal in the silicide increases. This is illustrated in Figure 5.8 where the Si_2–RE bond length, as determined using R_{Pflip}, is plotted as a function of the RE atomic number. This trend is actually apparent in a comparison of the experimental blocking curves from each silicide as demonstrated in Figure 5.2. The trend matches that known for the Si–RE bond length in the bulk silicide and reflects the decreasing ionic radii of the rare earths. The Si_1–Si_2 bond length remains approximately constant across the series. It is hoped that identification of such a trend may be of some use in future work to build more complex systems based on 2D rare earth silicides.

References

1. J. A. Knapp and S. T. Picraux, *Appl. Phys. Lett.* **48** 466 (1986)

2. S. D. Barrett, *Surf. Sci. Rep.* **14** 271 (1992)

3. S. Vandré, T. Kalka, C. Preinesberger and M. Dähne-Prietsch, *Phys. Rev. Lett.* **82** 1927 (1999)

4. S. Vandré, T. Kalka, C. Preinesberger and M. Dähne-Prietsch, *J. Vac. Sci. Technol. B* **17** 1682 (1999)

5. L. Stauffer, A. Mharchi, C. Pirri, P. Wetzel, D. Bolmont, G. Gewinner and C. Minot, *Phys. Rev. B* **47** 10555 (1993)

6. C. Rogero, C. Koitzsch, M. E. González, P. Aebi, J. Cerdá and J. A. Martín-Gago, *Phys. Rev. B* **69** 045312 (2004)

7. D. J. Spence, T. C. Q. Noakes, P. Bailey and S. P. Tear, *Surf. Sci.* **512** 61 (2002)

8. C. Rogero, C. Polop, L. Magaud, J. L. Sacedón, P. L. de Andrés and J. A. Martín-Gago, *Phys. Rev. B* **66** 235421 (2002)

9. D. J. Spence, S. P. Tear, P. Bailey and T. C. Q. Noakes, *Private Communication*

10. C. Bonet, D. J. Spence and S. P. Tear, *Surf. Sci.* **504** 183 (2002)

11. D. J. Spence, S. P. Tear, T. C. Q. Noakes and P. Bailey, *Phys. Rev. B* **61** 5707 (2000)

12. H. Kitayama, S. P. Tear, D. J. Spence and T. Urano, *Surf. Sci.* **482-485** 1481 (2001)

13. M. Lohmeier, W. J. Huisman, G. ter Horst, P. M. Zagwijn, E. Vlieg, C. L. Nicklin and T. S. Turner, *Phys. Rev. B* **54** 2004 (1996)

14. P. Wetzel, C. Pirri, P. Paki, D. Bolmont and G. Gewinner, *Phys. Rev. B* **47** 3677 (1993)

15. M. H. Tuilier, P. Wetzel, C. Pirri, D. Bolmont and G. Gewinner, *Phys. Rev. B* **50** 2333 (1994)

16. M. Lohmeier, W. J. Huisman, E. Vlieg, A. Nishiyama, C. L. Nicklin and T. S. Turner, *Surf. Sci.* **345** 247 (1996)

17. T. C. Q. Noakes, P. Bailey and D. P. Woodruff, *Nucl. Instrum. Meth. B* **136-138** 1125 (1998)

18. B. W. Busche and T. Gustafsson, *Phys. Rev. B* **61** 16097 (2000)

19. M. Chester and T. Gustafsson, *Surf. Sci.* **256** 135 (1991)

20. M. Copel, T. Gustafsson, W. R. Graham and S. M. Yalisove, *Phys. Rev. B* **33** 8110 (1986)

21. P. Fenter and T. Gustafsson, *Phys. Rev. B* **38** 10197 (1988)

22. J. B. Pendry, *J. Phys. C.: Solid State Phys.* **13** 937 (1980)

23. E. Zanazzi and F. Jona, *Surf. Sci.* **62** 61 (1977)

Chapter 6
MEIS Study of the Initial Growth of Fe on Si(111)

6.1 Introduction

Fe silicides have attracted much recent attention due to their direct band gap of ~0.85 eV [1, 2] and potential applications in the electronics industry [3-5]. Depending on the exact Fe:Si composition several phases may be formed which have been seen to exhibit semiconducting or metallic properties [6-14]. Despite this attention the Fe silicide system is still not fully understood, the bulk phase diagram being complex (Figure 6.1) [15]. This is particularly true of low Fe coverage on the clean Si surface, which is relevant for the possible integration of such silicides with current electronics. The formation of the iron–silicon interface is also of relevance to the possible application of Fe silicide in spin electronics

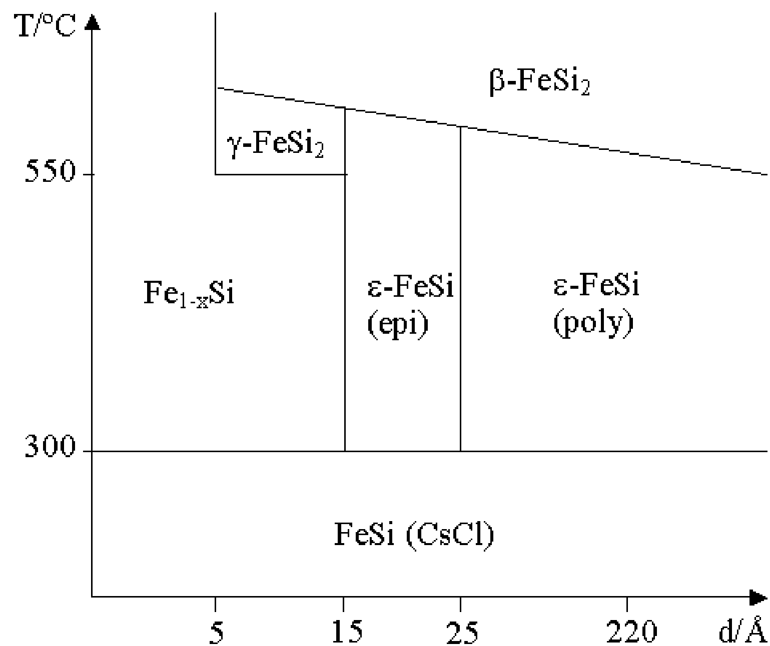

Figure 6.1: Bulk phase diagram for Fe silicide. After von Kanel et al. [15]. The FeSi system exhibits many phases in the bulk dependent on the precise Fe:Si composition and sample preparation.

(or "spintronics" as it has become known). One of the major problems within this rapidly developing field is the injection of spin polarised electrons into a semiconductor. One approach relies on a ferromagnetic layer to supply the spin polarised electrons. Fe silicides are obvious potential candidates for this ferromagnetic layer. Indeed, the first room temperature injection of spin polarised electrons into a semiconductor was demonstrated with Fe on GaAs [16]. However the Fe silicide–silicon interface is generally somewhat rough [7] which degrades efforts into spin injection from such a layer. A better understanding of the initial Fe growth ought to allow for a smoother interface to be developed.

In the context of the current body of work a MEIS study of the initial growth of Fe on the clean Si(111) surface was undertaken due to the interests as outlined above and as a precursor to the investigation of Fe growth on the 2D silicides described in previous chapters. In fact an initial investigation of such growth is briefly presented in the next chapter. The interpretation of Fe growth on 2D silicides would be greatly aided by a fuller understanding of the growth of Fe on Si.

6.2 Experimental Details

The MEIS experiments were performed at the CCLRC Daresbury Laboratory MEIS facility described in Chapter 2. Samples were prepared *in situ* under UHV conditions at a base pressure of around 1×10^{-10} mbar. Lightly doped, 100 Ω cm, *n*-type Si(111) wafers were cut into approximately 1×1 cm^2 samples. The samples were introduced into the UHV system and cleaned by repeated electron beam bombardment flash heating to 1200 ˚C followed by a slow (<100 ˚C/min) cool to room temperature. The temperature of the samples was monitored by means of an infra red pyrometer external to the vacuum chamber. The cleaned Si(111) samples produced a characteristic sharp 7 × 7 LEED pattern and AES showed no indication of surface contamination.

Fe was deposited onto the room temperature samples using an in house designed source consisting of a simple Fe wire heated by means of the passing of electrical current (15–20 A) through it. The pressure during this deposition remained below 1×10^{-9} mbar. Deposition rates were estimated from the MEIS spectra of as deposited samples. After deposition AES was used to ensure a lack of contamination (especially due to oxygen) and only a diffuse background was apparent from LEED. The samples were gently e^--beam annealed to around 300 ˚C, where upon a 1 × 1 LEED pattern could be observed. Further e^--beam annealing to about 500 ˚C produced a 2 × 2 LEED pattern. Such an evolution has been reported before (see for example Starke *et al*. [12] and Urano *et al.* [17, 18], though the structure is unclear). The 2 × 2 pattern could also be obtained from the freshly deposited samples by annealing to 500 ˚C without the intermediate anneal to 300 ˚C.

Once prepared in such a way the samples were transferred within the UHV system to the MEIS scattering chamber. A 100 keV H^+ ion beam was used in low index double alignment MEIS experiments. The beam dose was 10^{16} ions cm^{-2} and the size of the beam at the sample approximately 0.5 mm × 1 mm normal to the beam. In order to minimise sample damage the samples were moved vertically, maintaining the double alignment geometry, between acquiring data sets. Three double aligned scattering geometries were employed: [$\bar{1}$00] incidence with detection around [$\bar{1}$11]; [1$\bar{1}\bar{1}$] incidence with detection around [100]; and [1$\bar{1}$0] incidence with detection around [100].

6.3 Results and Discussion

6.3.1 Experimental Data

Typical MEIS spectra from the three scattering geometries are shown in Figure 6.2 and Figure 6.3. The mass separation effects are evident, allowing the signals from ions scattered from the Fe and Si to be clearly resolved, as indicated. Scattered ions with energy lower than those of the Si signal have been scattered

Original in colour

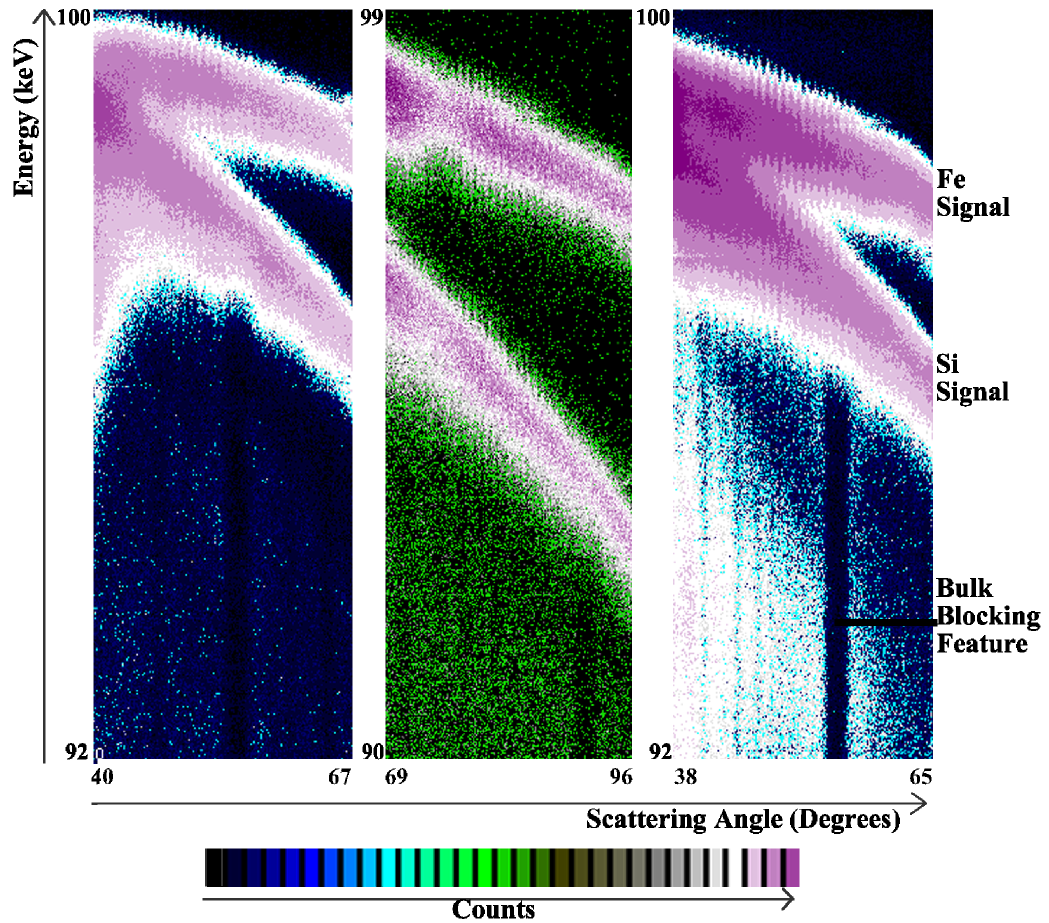

Figure 6.2: Typical MEIS spectra from the FeSi 1 × 1 phase. Left to right: [$\bar{1}$ 00]/[$\bar{1}$ 11], [1$\bar{1}$ 0]/[100], [1$\bar{1}$ $\bar{1}$]/[100]. The Fe signal shows clear blocking dips.

Original in colour

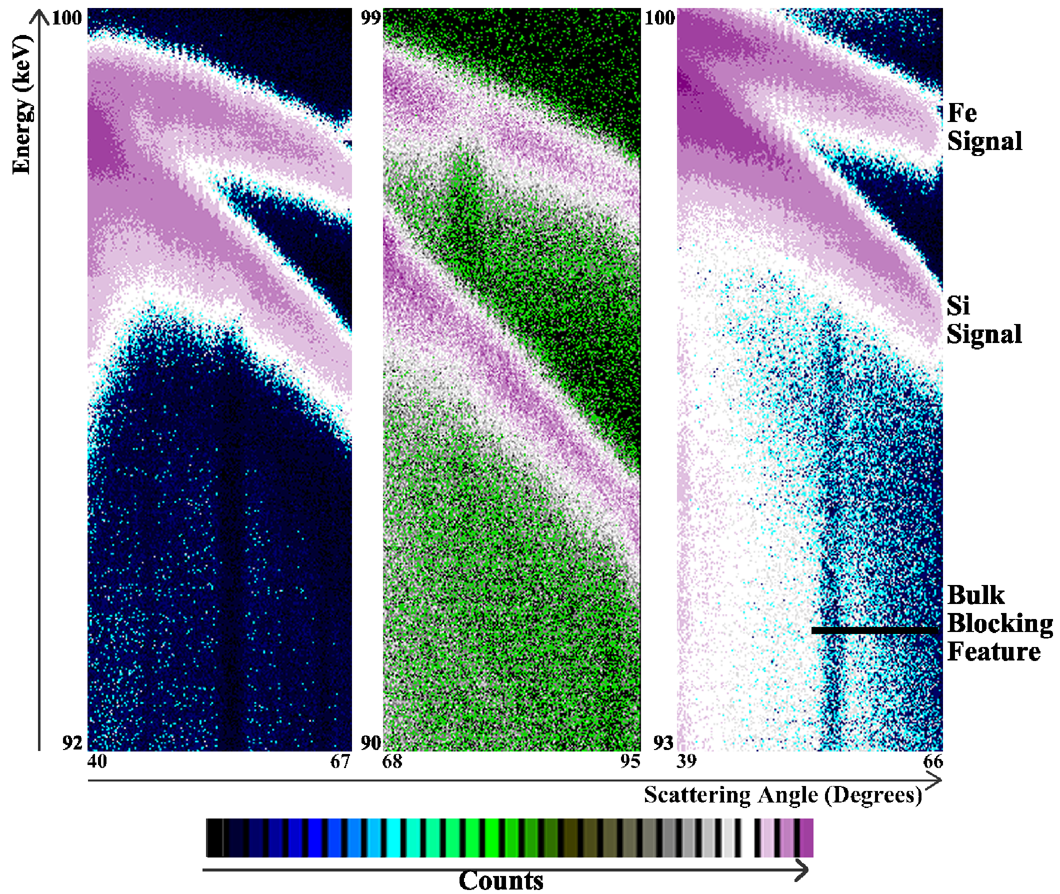

Figure 6.3: Typical MEIS spectra from the FeSi 2 × 2 phase. Left to right: [$\bar{1}$ 00]/[$\bar{1}$ 11]; [1$\bar{1}$ 0]/[100]; [1$\bar{1}$ $\bar{1}$]/[100]. The spectra are very similar to those observed for the 1 × 1 phase (Figure 6.2).

from the bulk Si. The main blocking dip in this bulk signal was used to calibrate the angular scale of the spectra correcting, for example, for any mechanical offset in the detector position. This was achieved by integrating the scattered ion count as a function of angle over the energy range corresponding to the bulk signal. The scattering curve so produced was then compared to a Monte Carlo computer simulation produced using the VEGAS code [19, 20] (see Chapter 3), of the scattering from bulk terminated Si and the blocking features examined. This allowed an angular shift to be determined to bring the blocking features into alignment and thus calibrate the angular scale.

The scattered ion count was similarly integrated as a function of angle over the energy range of the ions scattered from the Fe. This curve was then shifted by the angular offset determined from the bulk calibration procedure described above. The data was also corrected for the kinetic energy loss factor and the fall off in counts with scattering angle due to the Rutherford scattering cross section (the reader is directed to Chapter 3 for a fuller description of these effects).

The corrected scattering curves for both the 1 × 1 and 2 × 2 reconstructions are compared in Figure 6.4, Figure 6.5 and Figure 6.6. It is immediately apparent that the scattering curves from the two phases are extremely similar. This is consistent with the hypothesis that the 2 × 2 reconstruction is due to an ordered Si overlayer. Such a 2 × 2 overlayer would consist of ¼ monolayer (ML) of Si adatoms, which may be expected to contribute little to the blocking curves. However, this small contribution cannot in itself explain the similarity. It is also proposed that in these scattering geometries the 2 × 2 adatoms are effectively shadowed from the scattered ions by the layers below them.

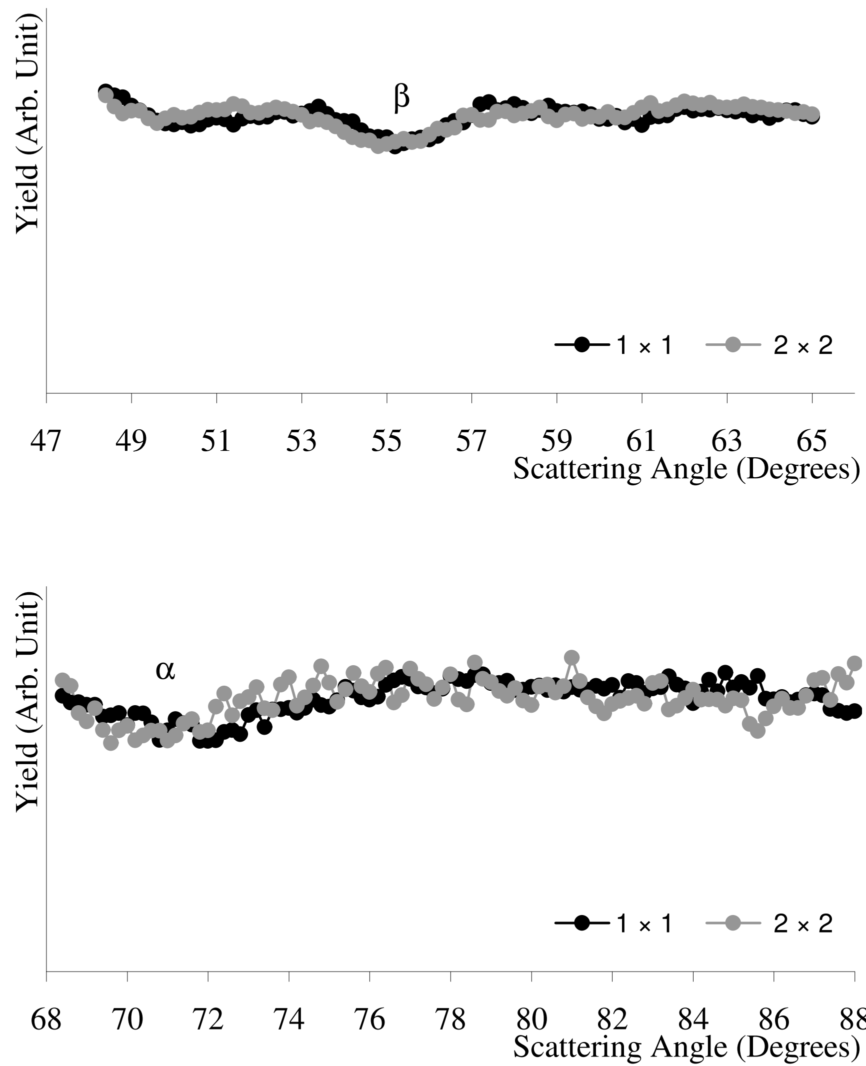

Figure 6.4: Comparison of scattering curves from the 1 × 1 and 2 × 2 phases. [$\bar{1}$ 00]/[$\bar{1}$ 11] geometry. The scattering curves from the two phases are extremely similar, indicating that their structures are very alike. See also Figure 6.5 and Figure 6.6.

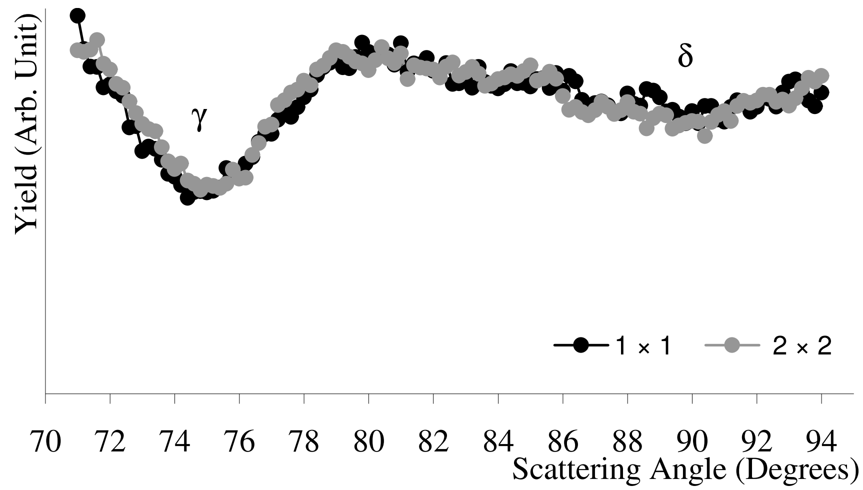

Figure 6.5: Comparison of scattering curves from the 1 × 1 and 2 × 2 phases. [1$\bar{1}$ 0]/[100] geometry. See also Figure 6.4 and Figure 6.6.

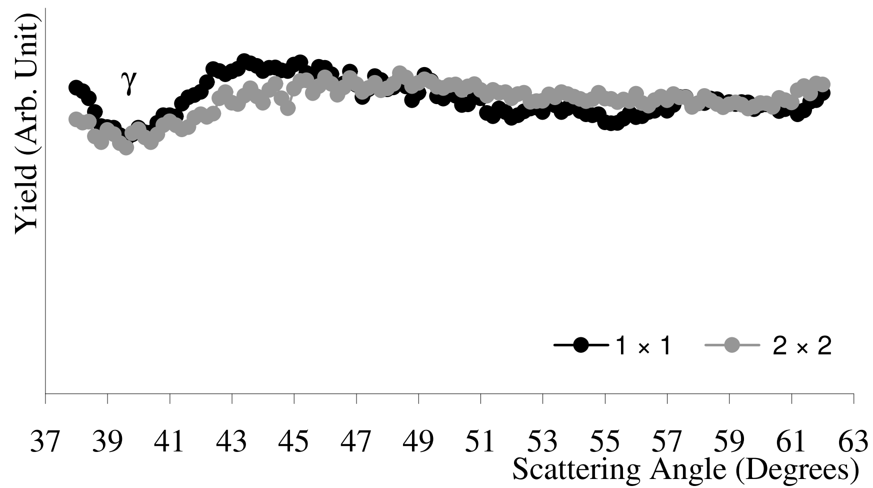

Figure 6.6: Comparison of scattering curves from the 1 × 1 and 2 × 2 phases. [1$\bar{1}$ $\bar{1}$]/[100] geometry. See also Figure 6.4 and Figure 6.5.

6.3.2 *Possible Models*

Bulk Fe silicides have a CsCl or CaF_2 type structure depending on the composition and anneal conditions. Based on geometric considerations of the position of blocking features in the Fe scattering curve several possible models for the Fe silicide were devised deriving from these structural types. Monte Carlo computer simulations of ion scattering from the Fe in these models were performed using the VEGAS codes, initially concentrating on just a 1×1 reconstruction.

From these simulations it was immediately apparent that there could be at most two Fe layers within the silicide. The introduction of a third or further, deeper, layers would introduce many more blocking features into the scattering curve than observed. This conclusion is consistent with the estimated Fe coverage of 1.7 ML which would imply at most two layers of Fe. It is noted here that for a single Fe layer there is no distinction between a CsCl- and CaF_2-type structure.

The simple CsCl- or CaF_2-type structures first modelled were found to be unable to reproduce the blocking features observed. Further careful consideration of the blocking features led to the construction of a model in which a CsCl-type Fe silicide layer has a “B-type” orientation with respect to the bulk Si, i.e. the “buckling” direction of the Fe silicide is reversed compared to that of the bulk Si. This model is shown in Figure 6.7. Such B-type orientated Fe silicide growth has been noted before [21-25]. Note that as the signal from Fe scattering was analysed the registration to the bulk Si, below the Fe, is unknown.

Figure 6.7 shows the 2×2 arrangement of Si adatoms. It is proposed that the 1×1 phase observed at lower anneal temperatures is identical but lacks this ordered 2×2 overlayer, though the extreme similarity of the blocking curves suggests that an unordered overlayer may be present with some Si atoms in T4 sites. Figure 6.8 shows the origin of the major blocking features in the three

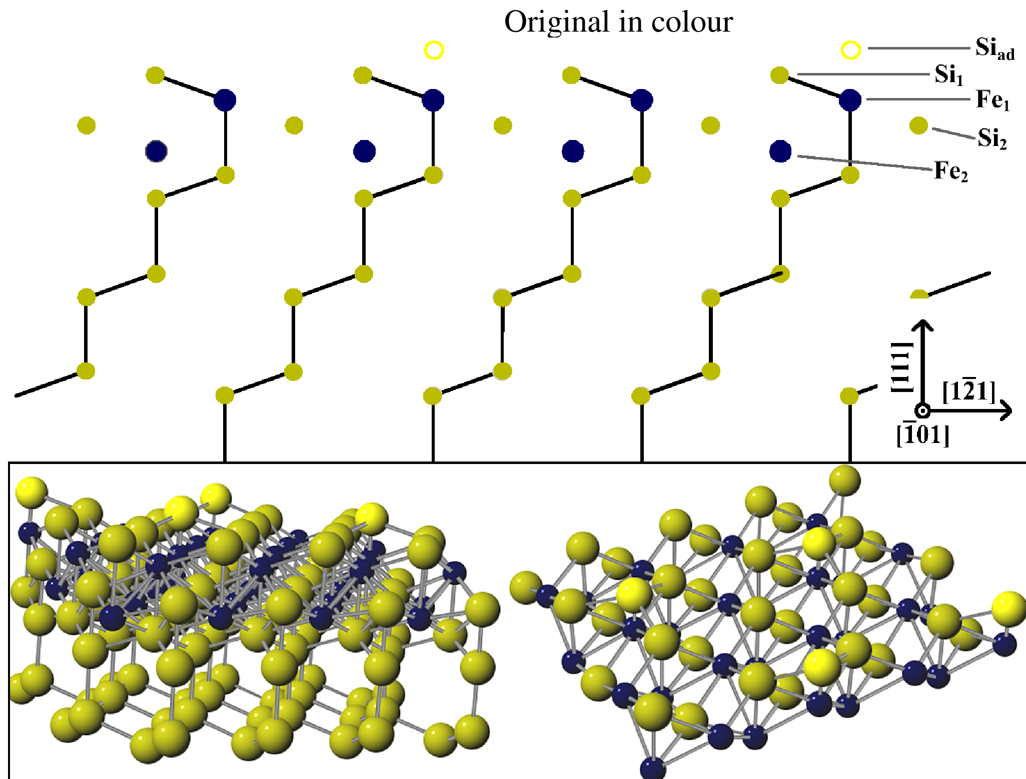

Figure 6.7: The proposed structural model for the initial Fe silicide growth. Side view showing the scattering plane. Note that the 2 × 2 phase is shown; the 1 × 1 phase is proposed to be identical but without the ordered Si overlayer, Si_{ad}. Inset: Ball and stick model of the surface—the model on the right has the bulk Si removed for clarity.

geometries for which data was available. It can be seen that the 2 × 2 arrangement of adatoms is mainly shadowed from the scattered ions.

6.3.3 Optimising Structural Parameters

A number of multicalc simulations were performed allowing the vertical heights of Si_{ad}, Si_1, Fe_1 and Si_2 to vary. The thermal vibrations of the atoms were estimated from the Debye temperatures [26] to give root mean square (rms) vibrational amplitudes of 0.08 Å. In order to adequately fit the size of the blocking curves it was necessary to develop a model in which the silicide contained 1 or 2 Fe layers in an equal ratio. i.e. half the surface covered with the silicide as shown in Figure 6.7 and the other half with the silicide lacking the Fe_2

layer. This is consistent with the estimated Fe coverage of 1.7 ML.

The analysis of the simulations was simplified by careful consideration of the origin of the blocking features. The feature labelled α in Figure 6.8 is due only to blocking by Fe_1 atoms of ions scattered from Fe_2. Therefore adjustment of the Fe_1 height, relative to Fe_2, to fit this blocking feature in the simulations allows the vertical separation of the two Fe layers to be fixed. The feature marked β could then be used to fix the vertical position of Si_1 and Si_{ad}—Si_{ad} must be at such a height as to remain in the shadow cone cast by the Si_1 atoms. The position of Si_1 could be confirmed from the γ feature. This blocking dip could also be used to determine the position of the Si2 atoms. Finally the δ blocking dip

Original in colour

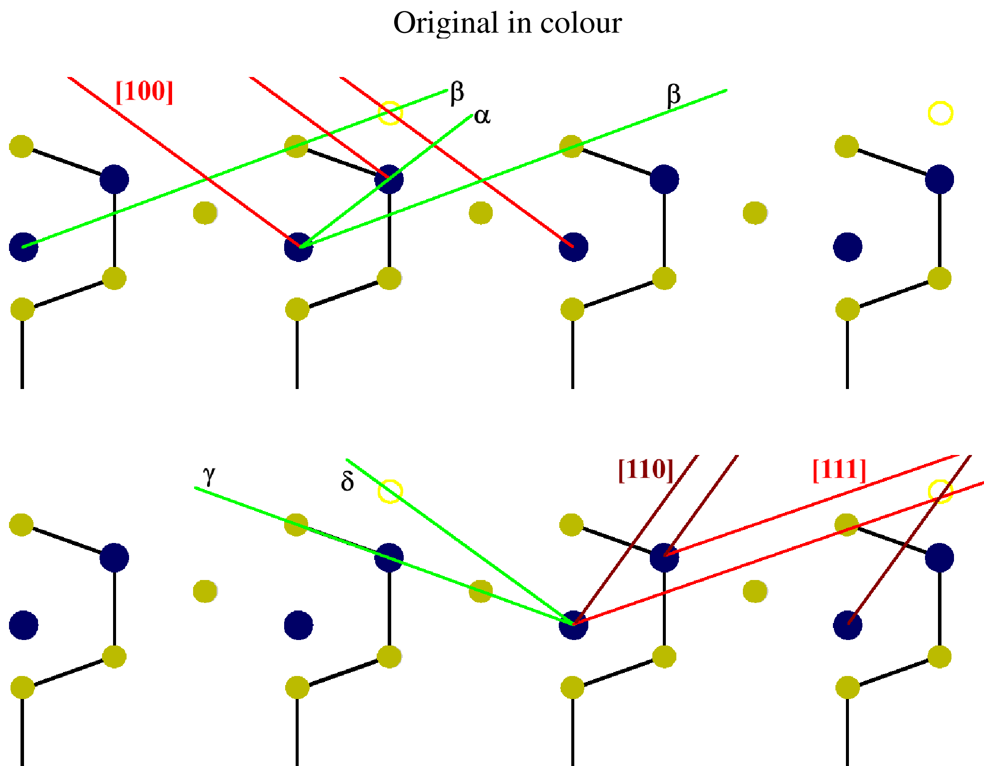

Figure 6.8: Origin of the blocking features. Note how the adatoms are mainly shadowed from the scattered ions. Red lines indicate the incident ion directions, green lines the origin of the observed blocking dips Top: [$\bar{1}$00]/[$\bar{1}$11] Bottom: [1$\bar{1}$0]/[100] and [1$\bar{1}\bar{1}$]/[100]—as ions are detected around [100] in both cases the same blocking dips are observed, although at different scattering angles.

confirms the position of the adatom. This feature is, however, weak due to it being only a $^1/_8$ monolayer contribution (the 2 × 2 adatom arrangement represents a $^1/_4$ monolayer but the blocking feature involves scattering from the second layer Fe, which is present in only half the surface area). In the case of the $[1\bar{1}\bar{1}]/[100]$ geometry the feature is weakened still further by the shadowing of the second layer Fe by the Si_1 atoms.

Comparisons of simulated scattering curves to the experimental data are presented in Figure 6.10, Figure 6.11, and Figure 6.12, for the 2 × 2 case. The structural parameters of this best fit model are given in Table 6.1 and shown in Figure 6.9. The Fe–Si bond lengths derived from this model are comparable to those for bulk Fe silicides (2.40 Å). The Si_{ad}–Si_1 bond length is slightly contracted compared to the Si–Si bond length of bulk Si (2.35 Å).

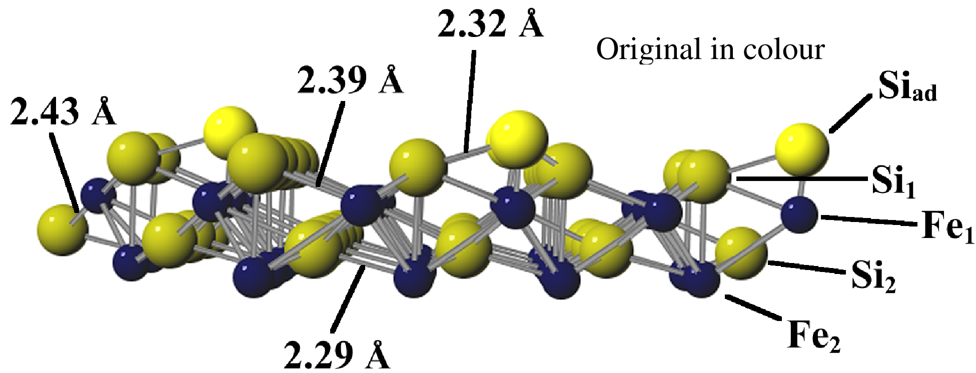

Figure 6.9: Ball and stick model of the surface, showing the bond lengths detailed in Table 6.1.

	Si_{ad}–Si_1 (Å)	*Si_1–Fe_1 (Å)*	*Fe_1–Si_2 (Å)*	*Si_2–Fe_2 (Å)*
Vertical Distance	*0.68 ± 0.05*	*0.88 ± 0.02*	*0.98 ± 0.04*	*0.58 ± 0.04*
Bond Length	*2.32 ± 0.03*	*2.39 ± 0.01*	*2.43 ± 0.02*	*2.29 ± 0.02*

Table 6.1: Structural parameters for the final model. See Figure 6.7 for labels.

Original in colour

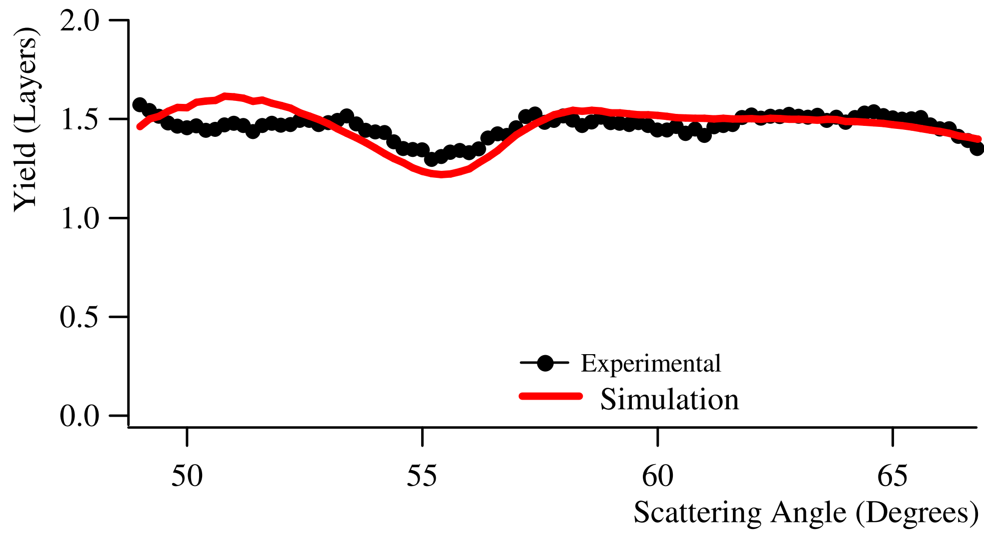

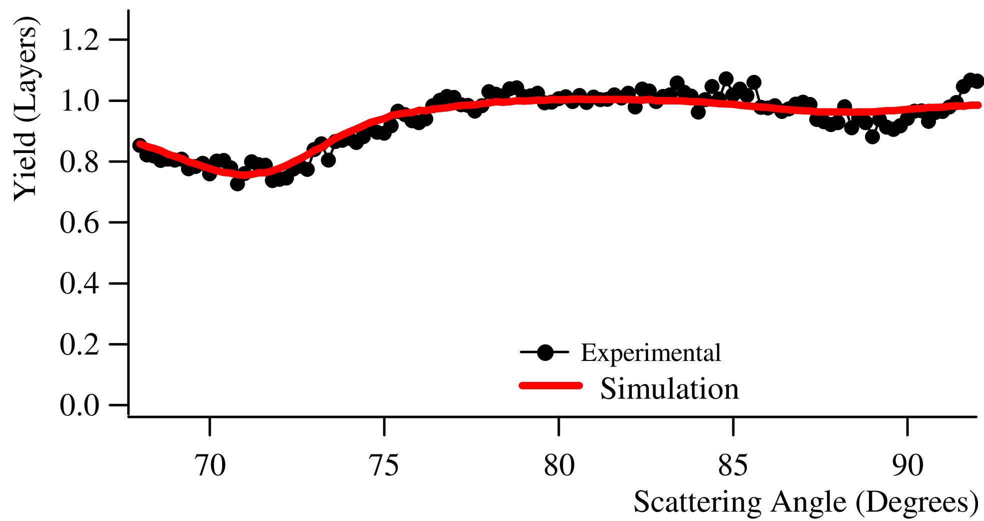

Figure 6.10: Comparison of simulated and experimental scattering curves for the final structural model. The [$\bar{1}$ 00]/[$\bar{1}$ 11] geometry.

Original in colour

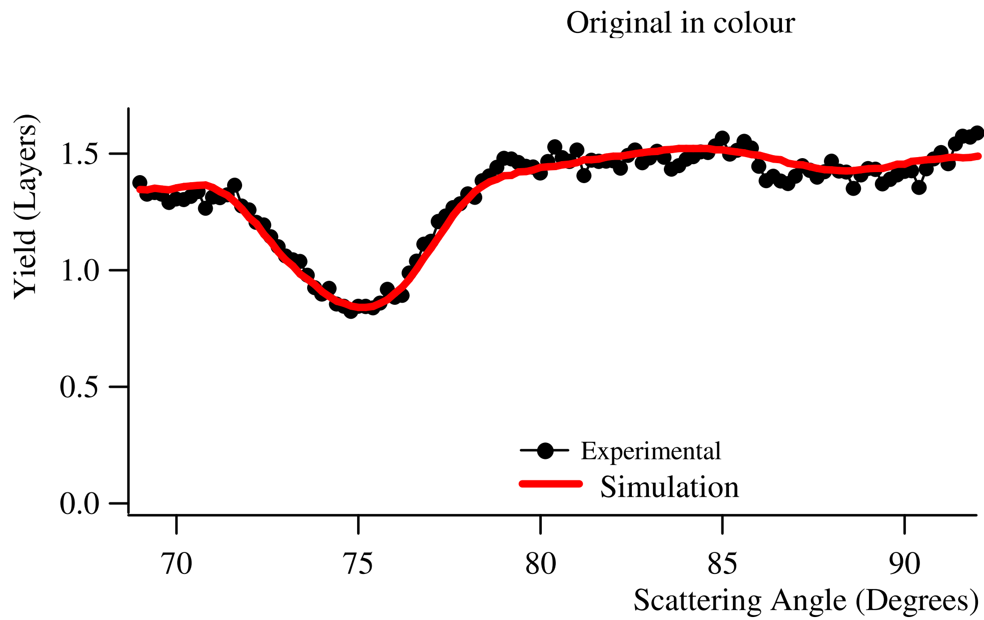

Figure 6.11 Comparison of simulated and experimental scattering curves for the final structural model. The [1$\bar{1}$ 0]/[100] geometry.

b)

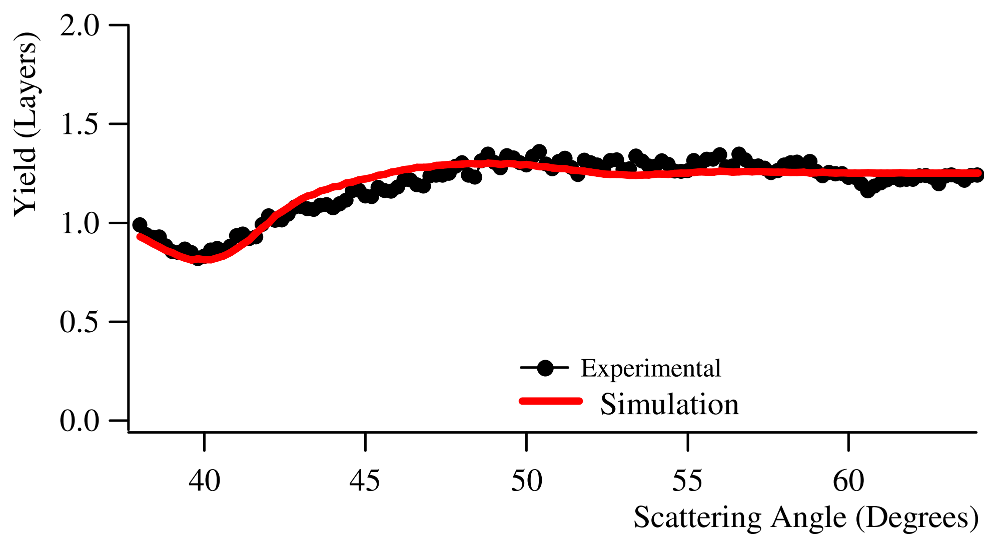

Figure 6.12: Comparison of simulated and experimental scattering curves for the final structural model. The [1$\bar{1}$ $\bar{1}$]/[100] geometry.

6.4 Conclusions

The initial growth of Fe on the Si(111) 7 × 7 surface has been studied by medium energy ion scattering. Depending upon the anneal conditions two possible phases have been formed. These phases exhibit a 1 × 1 reconstruction and a 2 × 2 reconstruction, as shown by LEED. The MEIS data shows the two phases to be extremely similar structurally, with very little difference in the blocking curves obtained from each phase.

It is proposed that the 2 × 2 phase is formed by the addition of a 2 × 2 overlayer of Si atoms, which are effectively shadowed from the scattered ions in this case. The structural model proposed consists of a B-type Fe silicide a with CaF_2 type structure. The adatoms rest in T4 sites above the first Fe layer, the Si–Si bond direction reverting to that of the bulk Si. To satisfactorily fit the observed blocking curves it was necessary to propose that the surface consisted of such a silicide with one and two Fe layers in equal proportion.

The structural model suggested could be confirmed with further MEIS data. While scattering data from slightly lower scattering angles within the scattering geometries used would provide further blocking features such data is not quite so readily obtained. At such low scattering angles the mass separation between the Fe and Si decreases making it difficult to extract the blocking curve from only one element. It is also important to maintain a bulk Si blocking feature within the data tile in order to calibrate the angular scale. A more rewarding approach may be to select a different scattering geometry, such as with the beam normal to the sample surface.

The surface also represents an ideal candidate for study by STM. The 2 × 2 Si overlayer would be apparent in STM images. STM may also reveal if there are indeed Si atoms within the T4 sites, but unordered, in the 1 × 1 phase as suggested by the similarity of the scattering curves.

This investigation of the initial formation of Fe silicide on the Si(111) 7 × 7 surface has resulted in a better understanding of the structures involved. This work may be used as a ba se for development of this understanding and also as an aid to understanding the interaction of Fe with more complex interfaces such as those formed by 2D silicides.

References

1. M. De Crescenzi, G. Gaggiotti, N. Motta, F. Patella, A. Balzarotti and J. Derrien, *Phys. Rev. B* **42** 5871 (1990)

2. N. E. Christensen, *Phys. Rev. B* **42** 7148 (1990)

3. T. Ehara, S. Nakagomi and Y. Kokubun, *Solid-State Electron.* **47** 353 (2003)

4. H. T. Lu, L. J. Chen, Y. L. Chueh and L. J. Chou, *J. Appl. Phys.* **93** 1468 (2003)

5. D. Leong, M. Harry, K. J. Reeson and K. P. Homewood, *Nature* **387** 686 (1997)

6. H. Moritz, B. Rösen, S. Popovic, A. Rizzi and H. Lüth, *Mat. Sci. Eng. B* **10** 1704 (1992)

7. J. de la Figuera, A. L. V. De Parga, J. Alverez, J. Ibanez, C. Ocal and R. Miranda, *Surf. Sci.* **264** 45 (1992)

8. W. Raunau, H. Niehus, T. Schilling and G. Comsa, *Surf. Sci.* **286** 203 (1993)

9. A. L. V. De Parga, J. de la Figuera, C. Ocal and R. Miranda, *Ultramicroscopy* **42-44** 845 (1992)

10. H. von Känel, R. Stalder, H. Sirringhaus, N. Onda and J. Henz, *Appl. Surf. Sci.* **53** 196 (1991)

11. U. Kafader, P. Wetzel, C. Pirri and G. Gewinner, *Appl. Phys. Lett.* **63** 2360 (1993)

12. U. Starke, W. Weiss, M. Kutschera, R. Bandorf and K. Heinz, *J. Appl. Phys.* **91** 6154 (2002)

13. X. Wallart, H. S. Zeng, J. P. Nys and G. Dalmai, *Appl. Surf. Sci.* **56-58** 427 (1992)

14. J. Alvarez, A. L. Vázquez de Parga, J. J. Hinarejos, J. de la Figuera, E. G. Michel, C. Ocal and R. Miranda, *J. Vac. Sci. Technol. A* **11** 929 (1993)

15. H. von Kanel, N. Onda, H. Sirringhaus, E. Muller-Gubler, S. Goncalces-Conto and C. Schwarz, *Appl. Surf. Sci.* **70/71** 559 (1993)

16. H. J. Zhu, M. Ramsteiner, H. Kostial, M. Wassermeier, H. -P. Schönherr and K. H. Ploog, *Phys. Rev. Lett.* **87** 016601 (2001)

17. T. Urano and T. Kanaji, *Appl. Surf. Sci.* **33/34** 68 (1988)

18. T. Urano, M. Kaburagi, S. Hongo and T. Kanaji, *Appl. Surf. Sci.* **41/42** 103 (1989)

19. R. M. Tromp and J. F. van der Veen, *Surf. Sci.* **133** 159 (1983)

20. J. F. van der Veen, *Surf. Sci. Rep.* **5** 199 (1985)

21. U. Kafader, C. Pirri, P. Wetzel and G. Gewinner, *Appl. Surf. Sci.* **64** 297 (1993)

22. S. Walter, R. Bandorf, W. Weiss, K. Heinz, U. Starke, M. Strass, M. Bockstedte and O. Pankratov, *Phys. Rev. B* **67** 085413 (2003)

23. S Walter, F Blobner, M Krause, S Müller, K Heinz and U Starke, *J. Phys. Condens. Matter* **15** 5207 (2003)

24. H. Sirringhaus, N. Onda, E. Müller–Gubler, P. Müller, R. Stalder and H. von Känel, *Phys. Rev. B* **47** 10567 (1993)

25. S. Hong, C. Pirri, P. Wetzel, D. Bolmont and G. Gewinner, *Appl. Surf. Sci.* **90** 65 (1995)

26. D. P. Woodruff and T. A. Delchar, *Modern Techniques of Surface Science*, Cambridge University Press (1986)

Chapter 7
Studies of the 2D Silicide Surface

7.1 Introduction

Two dimensional rare earth silicides have been seen to be novel and interesting structures. Their unusual properties may lead to technological applications. The crystallographic structure of these 2D silicides is now well known [1-7], and detailed study as described in Chapter 5 has revealed trends in this structure across the series. It is timely and interesting to study the electronic structure of these surfaces as well as investigating the interaction of this interface with further metallic overlayers.

Preliminary experiments along these lines have been performed. The first section of this chapter discusses an investigation of the electronic structure of the 2D silicide surface on the atomic scale by means of scanning tunnelling spectroscopy (STS). The second section describes an initial look at the possibility of using the unusual 1×1 surface as a novel growth template, in this case for the formation of Fe silicide.

7.2 STS of 2D Holmium Silicide

7.2.1 Introduction

Two dimensional Ho silicide has a structure extremely similar to that of the two dimensional Tm silicide, as discussed in Chapters 4 and 5. The structure has been well studied [2, 8, 9]. The electronic structure of similar 2D rare earth silicides has been investigated by a number of groups [4, 9-16]. Unsurprisingly given the similarities between rare earth metals and the structure of all these silicides, few differences have been observed in the electronic structure. The band structure

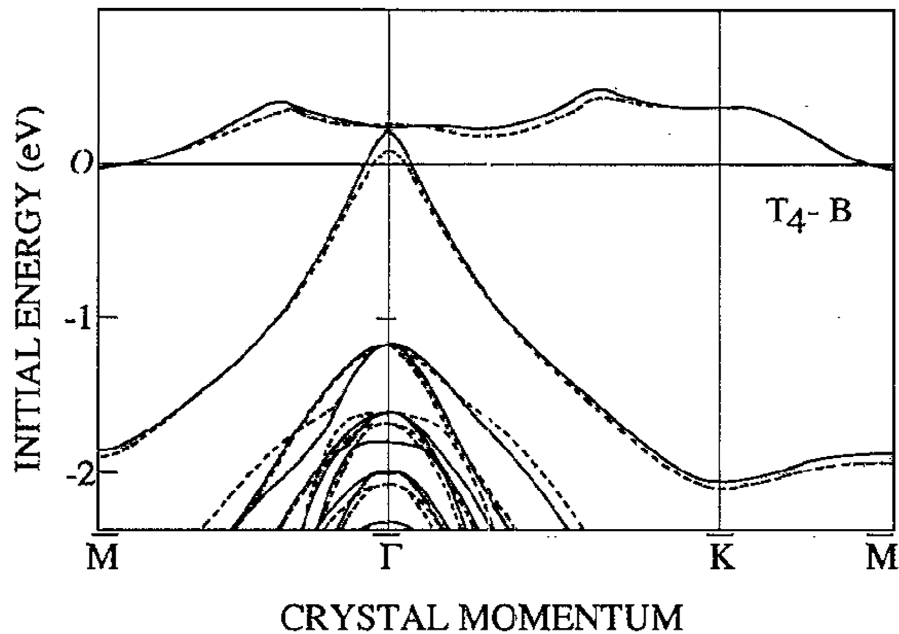

Figure 7.1: Theoretical band structure of RE 2D silicide [4]. Note the hole pocket at the $\bar{\Gamma}$ point.

(Figure 7.1) shows an interesting hole pocket at the Γ-point and electron pocket around the M-point. There is an occupied state approximately 1.3eV below the Fermi energy at the Γ-point and a flat band just above the Fermi energy.

Of the three rare earth valence electrons one saturates the upward pointing dangling bond of the Si bilayer beneath and a second the downward pointing dangling bonds of that above. The third valence electron forms a fairly delocalised 5d–3p hybridised state with the Si of the top bilayer.

7.2.2 Experimental

The STM and STS results reported here were obtained using the Omicron STMs described in Chapter 2. Si(111) samples were cut from lightly doped 100 Ω cm *n*-type wafers. The base pressure of the UHV systems was around 1×10^{-10} mbar. The samples were cleaned by passing direct current through them to repeatedly flash heat to ~1200 ˚C with slow cooling (<100 ˚C/min) to room temperature. The cleanliness of the surface was confirmed by the characteristic sharp 7 × 7 LEED pattern. Ho was deposited at room temperature onto the freshly prepared

sample from a homemade source similar to that used for the deposition of Tm in Chapter 4. The as deposited samples produced only a diffuse background when examined with LEED. Samples were annealed to about 500 ˚C by passing direct current through them, the temperature being measured using an external infra-red pyrometer. After anneal a sharp, low background 1 × 1 LEED pattern was observed and was taken to indicate the successful formation of a 2D Ho silicide. Samples were then transferred under UHV conditions to the STM instrument and probed using chemically etched tungsten tips.

7.2.3 Scanning Tunnelling Microscopy

The principles of STM and STS have been described in Chapter 2. STM was performed on the 2D Ho silicides, with atomic resolution. STM images of the surface of the 2D silicide reveal the 1 × 1 reconstruction of the uppermost Si bilayer. Figure 7.2 and Figure 7.3 show typical images. Figure 7.3 indicates several inequivalent sites on the surface. On Top indicates sites directly above the uppermost Si atom. Dark A and DarkB represent those sites located above the RE atoms (H3 sites) or above the lower Si atom of the terminating Si bilayer (T4 sites). Unfortunately there is no way to distinguish if Dark A corresponds to the former case (in which case Dark B would be above the Si) or the latter (in which case DarkB would be above the RE) from the STM image alone.

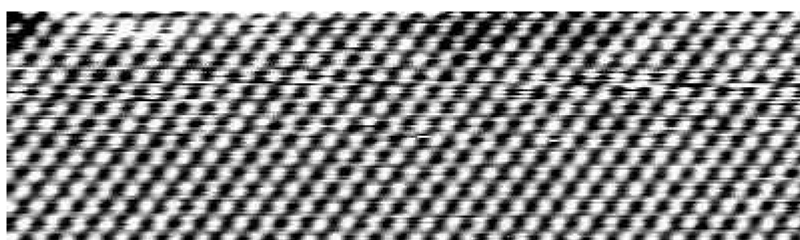

Figure 7.2: Atomically resolved STM image of the 2D Ho silicide surface. Imaged aquired at a bias voltage of 2V, tunnelling current 2nA. ~10 nm × ~3 nm.

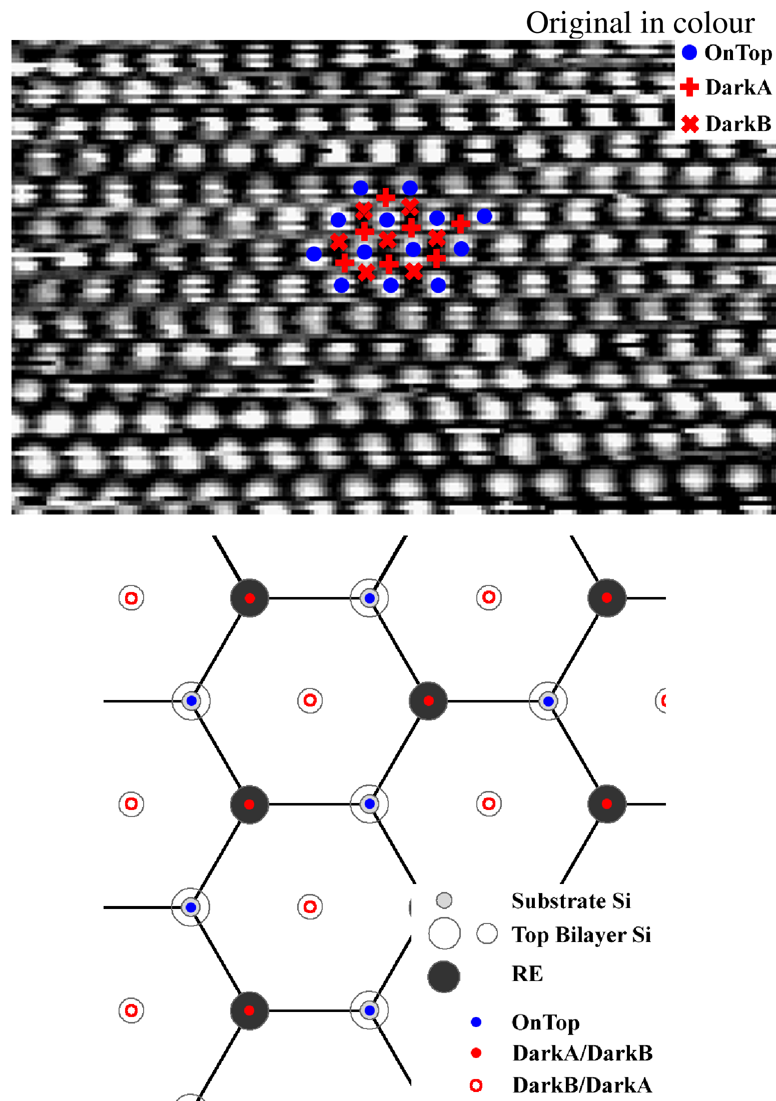

Figure 7.3: Inequivalent sites on the 2D silicide surface. Top: atomically resolved STM image, bias voltage 2 V, tunnelling current 2 nA. ~5.0 nm × ~3.6 nm. Bottom: Schematic top view of the surface.

7.2.4 Scanning Tunnelling Spectroscopy

Scanning tunnelling spectroscopy curves were obtained at a regular grid of points whilst preforming atomic resolution STM of the 2D Ho silicide. A typical plot of tunnelling current versus applied bias voltage is shown in Figure 7.4. It is well established [17-19] that a plot of the logarithmic derivative of the tunnelling current, (dI/dV)/(I/V)—or equivalently d[ln (I)]/d[ln(V)]—, produces a good representation of the local density of states. This quantity removes the

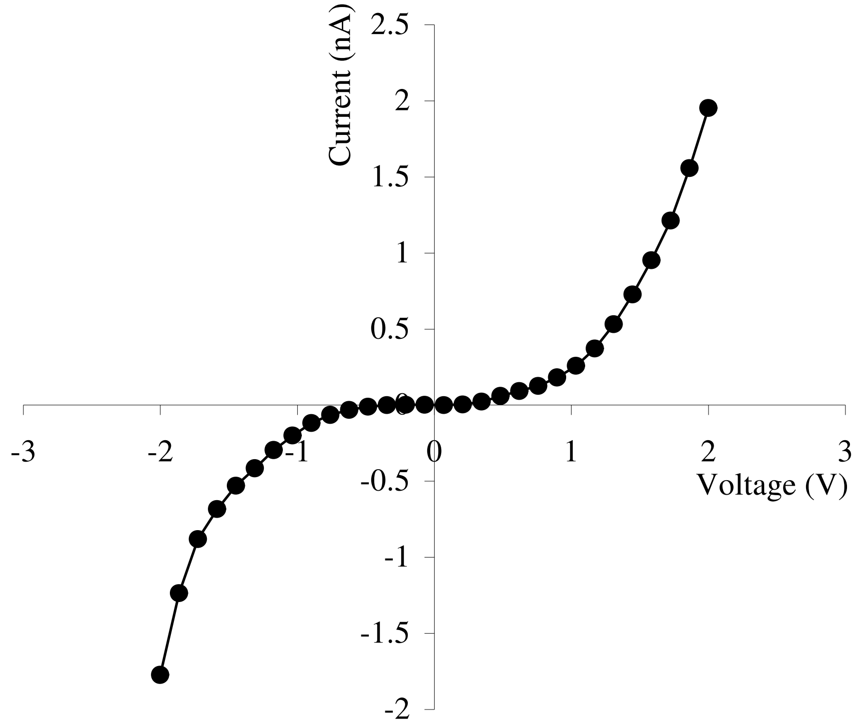

Figure 7.4: Typical plot of tunnelling current, I, versus bias voltage, V, averaged from equivalent sites on the atomically resolved 2D silicide surface close to zero applied voltage.

dependence of the tunnelling current on the sample–tip separation. Such a plot ~derived from the curve of Figure 7.4 is shown in Figure 7.5. It is noted that in practice the I/V curve is often noisy in the low voltage regime (~-0.3 V ≤ V ≤ ~+0.3 V). This can result in spurious large peaks in the logarithmic derivative. To prevent this problem the I/V curve is.broadened by convoluting it with a response function of the form exp(-|V/ΔV|), i.e.

$$\overline{I / V} = (I / V)\, e^{-\left|V/\Delta V\right|} \tag{7.1}$$

The term ΔV gives the width of the broadening function and must be chosen so as to be small enough not to wash out all detail while remaining large enough to remove the spurious noise. A value of ΔV = 0.66 V has been found to give

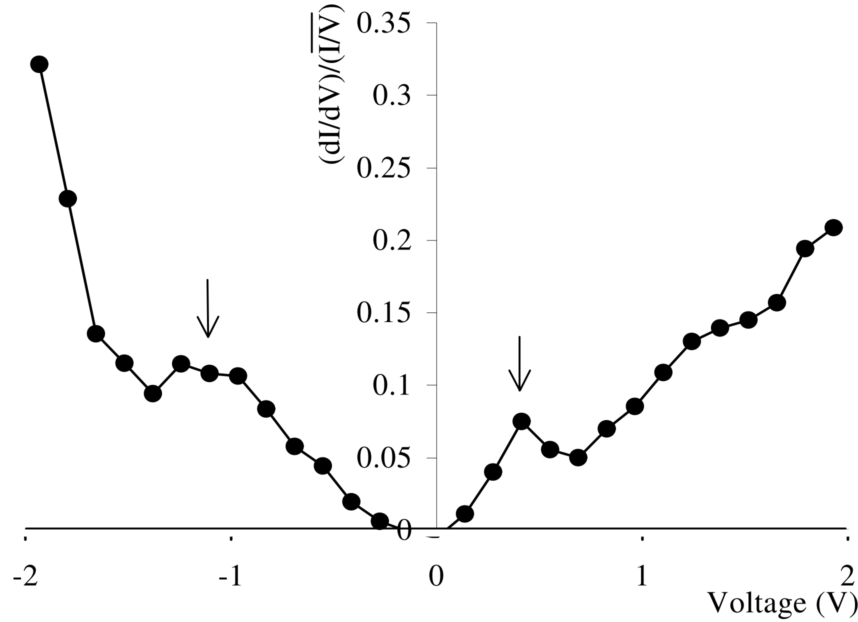

Figure 7.5: The LDOS is better represented by a plot of (dI/dV)/(I/V) versus bias voltage. Arrowed are features corresponding to bands in the 2D silicide band structure

satisfactory results [20]. It is this value which is used in the calculation of the logarithmic derivatives [19-21].

7.2.5 Spatially Resolved Spectra

STS spectra were obtained over a grid of points on a spatially resolved STM image. Three inequivalent sites were identified as indicated in Figure 7.3. For each of these sites the I/V curves from many equivalent points were averaged to give a final I/V curve and the logarithmic derivative calculated. The results of this exercise may be seen in Figure 7.6. It is immediately apparent that the spectra from each site are indistinguishable within error. This is unusual and in stark contrast to a surface such as the Si(111) 7 × 7 reconstruction where inequivalent sites show a clear difference in the STS spectra obtained [22-24]. Figure 7.7 shows STS collected from a region of 2D silicide imaged alongside a region of Si(111) 7 × 7. The different sites within the 7 × 7 unit cell can be distinguished and are in reasonable agreement with published results [22-24].

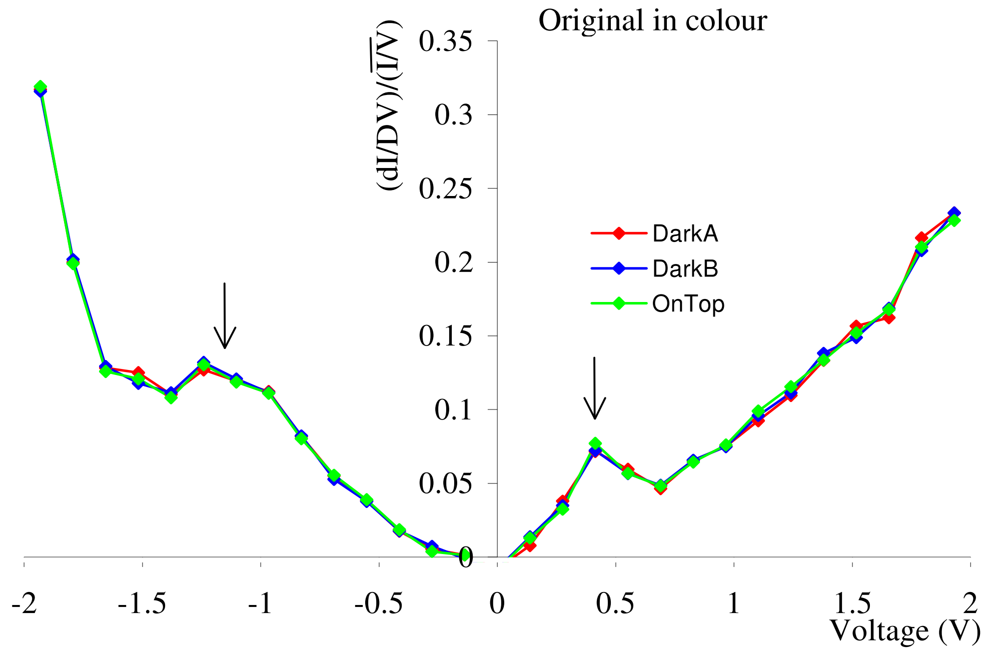

Figure 7.6: STS spectra from three inequivalent sites on the atomically resolved 2D Ho silicide surface. Arrowed are features corresponding to bands in the 2D silicide band structure.

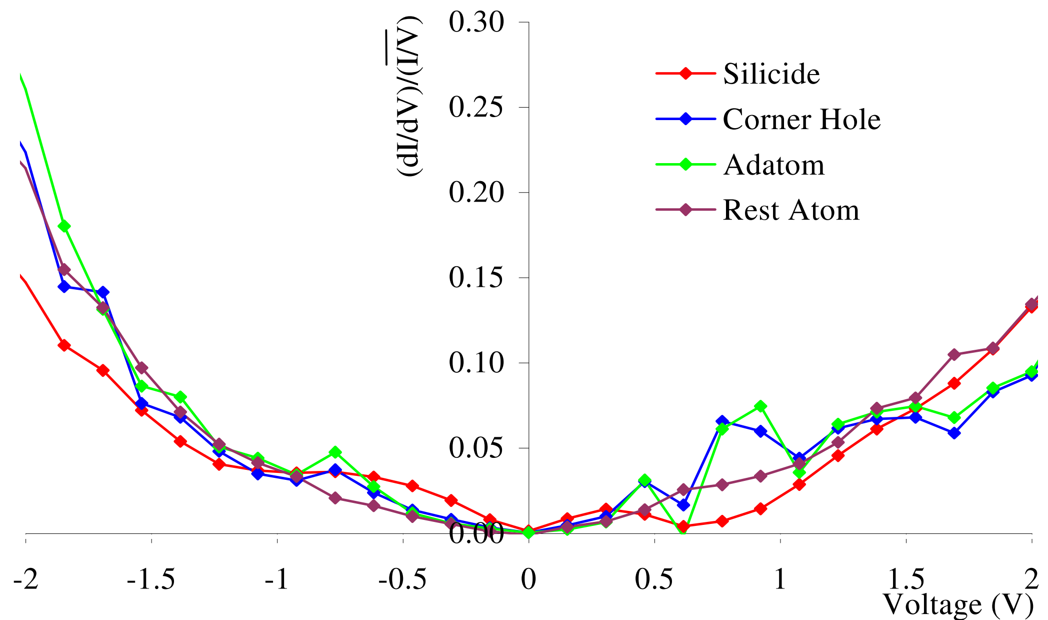

Figure 7.7: Comparison of STS from a region of 2D silicide and various sites within the Si(111) 7 × 7 unit cell.

This suggests that the tip electronic structure is having a negligible effect on the spectroscopy obtained.

The spectra obtained may be understood in terms of the band structure of 2D silicides. Although the experiments reported here involved Ho silicides theoretical and experimental band structures for other 2D silicides have been reported [4, 13, 16]. It is expected that the band structure in the Ho case will be very similar.

The states mainly involved with tunnelling will be those for which $k_{||}$ is small, i.e. those around the Γ-point of the surface Brillouin zone. As mentioned above the states around the Γ-point are formed by the hybridisation of the rare earth 5d and top layer Si dangling bond 3d states and are hence fairly delocalised. It is this delocalisation which means individual sites are so difficult to distinguish in the case of the Ho silicide. This delocalisation has previous been noted in the case of the so called 3D silicide formed at higher coverage [25]. As there, here it seems that the STM image closely reflects the actual topography of the sample.

The occupied state band at ~-1.3 eV is observed in the STS as is the empty state band ~0.5 eV above the Fermi level (indicated by arrows in Figure 7.6). Although the precise bias voltage at which these features occurs is seen to move slightly between samples (probably due to band bending and other tip–sample interactions—spectra taken with a higher current set-point tend to show the features at higher bias voltage) they consistently appear across spectra taken from a range of samples and with numerous tips. In fact STS offers one of the few ways to experimentally access the band structure above the Fermi level and confirm the theoretical predictions (at least around the Γ-point).

7.3 Initial MEIS Study of Fe Growth on 2D Holmium Silicide

7.3.1 Introduction

It has previously been mentioned that it is possible 2D rare earth silicides may find technological applications. The possibility of the rare earth layer acting as a barrier for a role in spin electronics was mentioned in Chapter 6. It is important to understand how this novel surface interacts with metallic overlayers. As an initial approach to the investigation of this problem a brief MEIS study of the growth of Fe on the surface of a Ho 2D silicide was undertaken. MEIS offers an ideal tool for the study of the crystallography of any interface at the surface of these systems. The rare earth signal may be extracted and analysed to give information about atomic positions of those layers closer to the surface. If the deposited metal is also well separated in mass from the Si and rare earth then the signal from all three elements may be observed. This is the case with Fe.

7.3.2 Experimental

The experiments were carried out at the Daresbury MEIS facility, previously described in Chapter 2. Samples were prepared in a similar manner to the Tm 2D silicides discussed in Chapter 4. One monolayer of Ho was deposited onto the freshly prepared Si(111) 7 × 7 surface and annealed to ~550 ˚C. The formation of a 2D silicide was confirmed by the sharp 1 × 1 LEED pattern and the characteristic blocking features. Note the clear blocking feature visible in the spectrum from the 2D silicide shown in Figure 7.8 and Figure 7.9 insets.

Fe was deposited from a source of similar design to that used in the experiments of Chapter 6. The Fe coverage was estimated from the MEIS spectra to be 1.7 ML. Immediately after the Fe deposition the 1 × 1 LEED pattern was seen to no longer be present with only a diffuse background observed. The sample was transferred under UHV to the MEIS scattering chamber and a series of MEIS

spectra taken.

7.3.3 Results and Discussion

The MEIS spectra from the as-deposited, room temperature Fe/Si(111) 1 × 1-Ho sample is shown in Figure 7.8a. The scattering signals from all three elements are clearly resolved. A small oxygen signal, (just visible in Figure 7.8b), was also detected. The uncorrected (for Rutherford scattering cross-section and TEA offset) scattering curves from the Ho and Fe signals are shown in Figure 7.9a. As this was a preliminary investigation only one data set was available and the scattering curves are hence noisier than might have been desired. Never the less, it is still clear that there are no major blocking features in any of the Fe, Ho or Si signals, indicating that the Fe has not formed an ordered structure and has disrupted the structure of the 2D silicide.

The sample was further annealed to around 550 ˚C. The MEIS spectra shown in Figure 7.8b was taken after this anneal. The broadening of the Fe scattering signal indicates that the Fe is beginning to diffuse into the bulk. The slight broadening of the Ho scattering signal is probably due to intermixing of the Fe and Ho. The scattering curves from this system are shown in Figure 7.9b. Again although noisy the scattering curves clearly lack the blocking features expected from an ordered surface.

The sample was annealed yet further to ~700 ˚C. This succeeded only in causing the Ho and Fe to both completely diffuse into the bulk, as shown by Figure 7.8c. Throughout the annealing sequence there was no LEED pattern detectable, only a bright, diffuse background, confirming the lack of ordered surface structure.

Original in colour

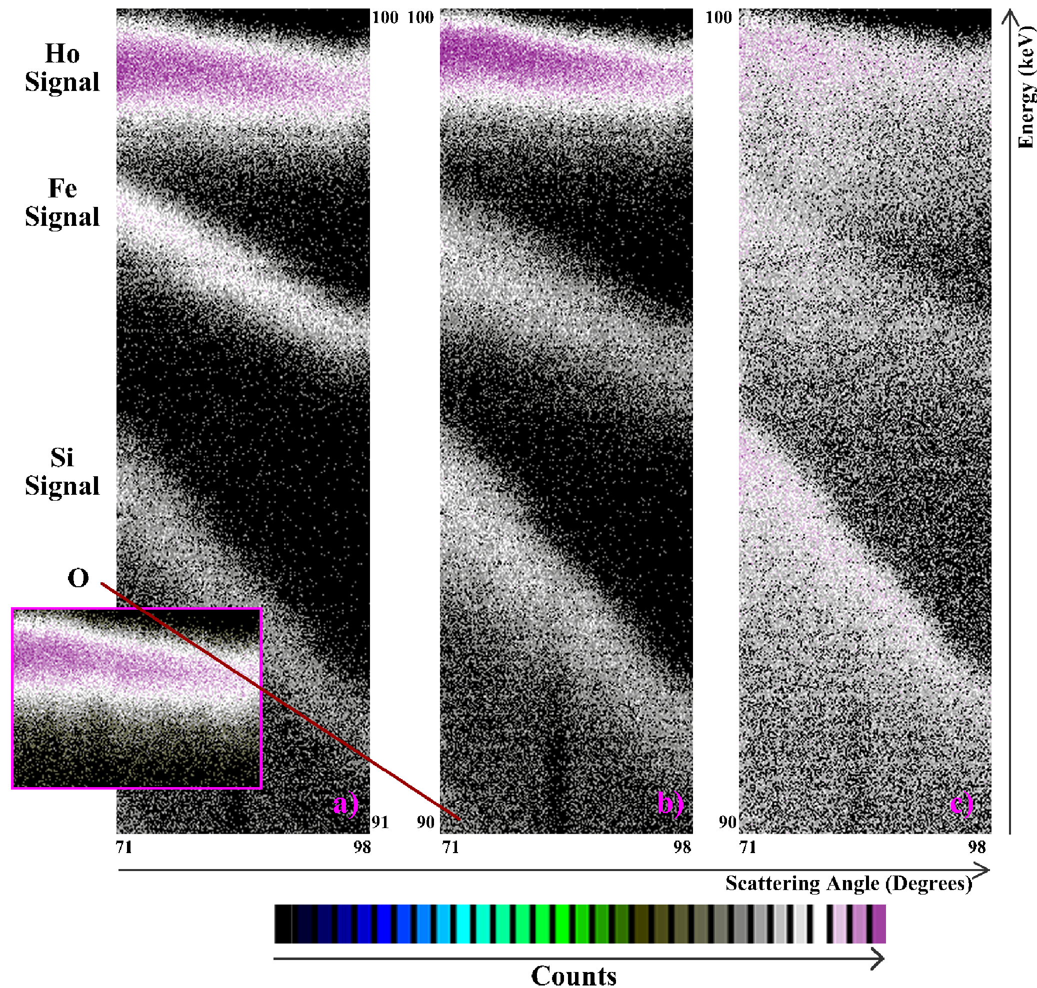

Figure 7.8: The sequence of MEIS spectra from Fe deposition on Ho 2D silicide. [1$\bar{1}$ 0] incident direction with detection around [100]. a) As deposited b) After anneal to ~550 ˚C c) After anneal to ~700 ˚C. The inset shows the Ho scattering signal from the 2D silicide before Fe deposition. The surface is initially disrupted and increasing annealing simply causes diffusion of the Fe and Ho into the bulk substrate.

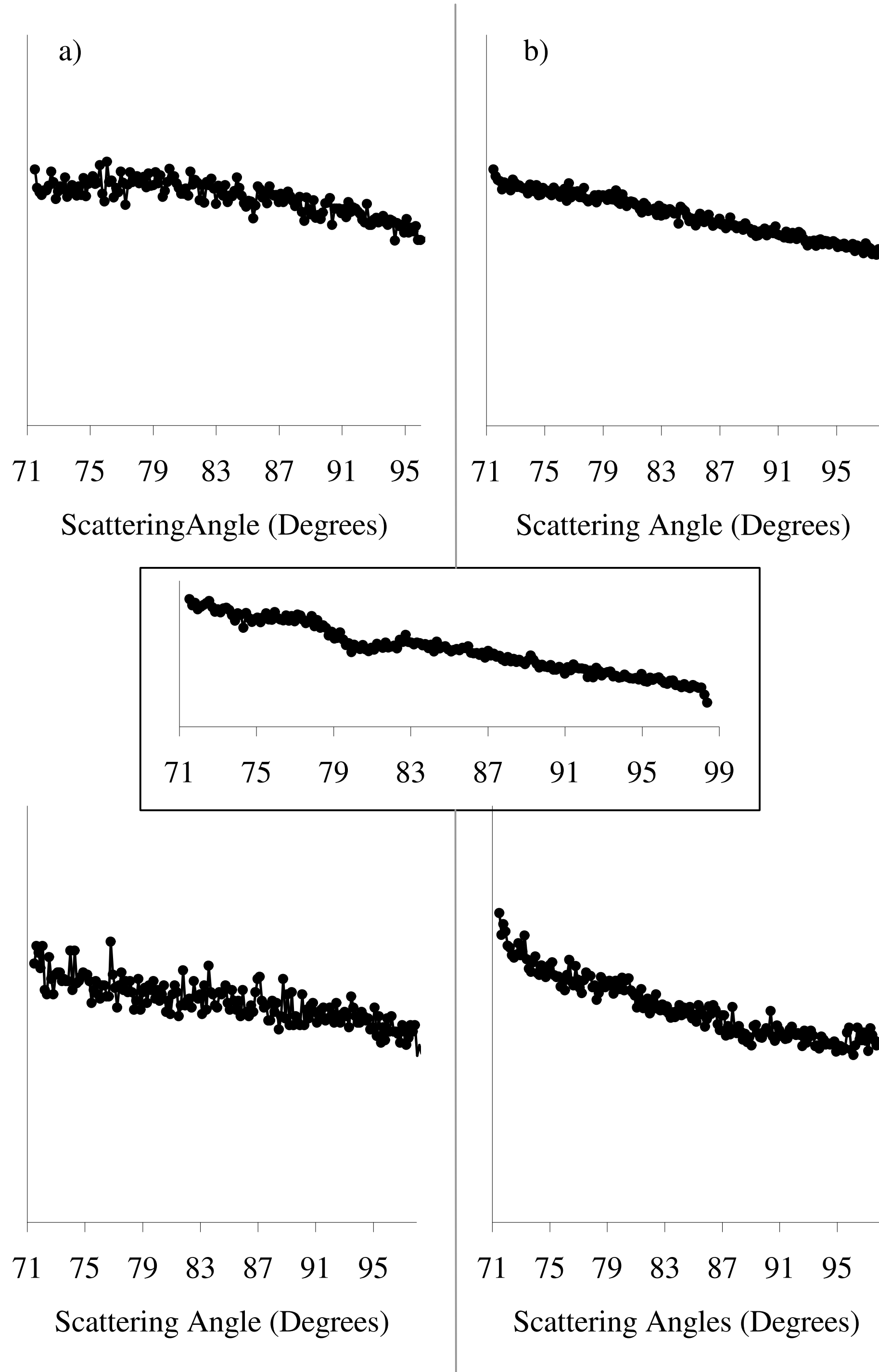

Figure 7.9: Scattering cross section through the Ho (top) and Fe (bottom) signals of spectra shown in Figure 7.8. a) As deposited b) After anneal to ~550 ˚C. Inset: The scattering curve through the Ho signal before Fe deposition. The lack of blocking features in the Ho and Fe signals indicate a lack of order at the surface.

7.4 Conclusion

Preliminary studies into the unique surface of the two dimensional rare earth silicides have been made. The electronic structure of the surface has been investigated by means of scanning tunnelling spectroscopy. The spectroscopy is unusual in that it has not been possible to distinguish between spectra from atomically resolved inequivalent sites. This indicates a delocalised state near the Fermi energy of the surface. The spectra obtained are in qualitative agreement with experimentally and theoretically determined band structures of rare earth silicides and offer a rare opportunity to confirm theoretical predictions regarding the band structure of the empty states.

The use of the surface as a growth template has also been examined. Fe silicides have possible applications in spintronics but their use is hampered by the rough silicide–silicon interface. The possibility that the rare earth layer may act as a form of buffer and the 1×1 surface atomic arrangement a better growth template presents itself. To investigate this an initial MEIS study of Fe growth on Ho 2D silicide was performed. Unfortunately the Fe was seen to disrupt the silicide surface and no ordered structure was obtained. There is however the possibility that oxygen contamination played some role in this disruption. Oxygen is known to disrupt the 2D silicide structure [26]. Further investigation of the use of the 2D silicides as a growth template for Fe is therefore merited.

References

1. D. J. Spence, S. P. Tear, P. Bailey and T. C. Q. Noakes, *Private Communication*

2. H. Kitayama, S. P. Tear, D. J. Spence and T. Urano, *Surf. Sci.* **482-485** 1481 (2001)

3. D. J. Spence, T. C. Q. Noakes, P. Bailey and S. P. Tear, *Surf. Sci.* **512** 61 (2002)

4. L. Stauffer, A. Mharchi, C. Pirri, P. Wetzel, D. Bolmont, G. Gewinner and C. Minot, *Phys. Rev. B* **47** 10555 (1993)

5. C. Rogero, C. Polop, L. Magaud, J. L. Sacedón, P. L. de Andrés and J. A. Martín-Gago, *Phys. Rev. B* **66** 235421 (2002)

6. P. Wetzel, C. Pirri, P. Paki, D. Bolmont and G. Gewinner, *Phys. Rev. B* **47** 3677 (1993)

7. M. Lohmeier, W. J. Huisman, G. ter Horst, P. M. Zagwijn, E. Vlieg, C. L. Nicklin and T. S. Turner, *Phys. Rev. B* **54** 2004 (1996)

8. D. J. Spence, S. P. Tear, T. C. Q. Noakes and P. Bailey, *Phys. Rev. B* **61** 5707 (2000)

9. O. Sakho, F. Sirotti, M. Desantes, M. Sachhi and G. Rossi, *Appl. Surf. Sci.* **56-58** 568 (1992)

10. S. Vandré, T. Kalka, C. Preinesberger and M. Dähne-Prietsch, *J. Vac. Sci. Technol. B* **17** 1682 (1999)

11. S. Vandré, T. Kalka, C. Preinesberger and M. Dähne-Prietsch, *Phys. Rev. Lett.* **82** 1927 (1999)

12. J.-Y. Veuillen, D. B. B. Lollman, T. A. N. Tan and L. Magaud, *Appl. Surf. Sci.* **65/66** 712 (1993)

13. C. Rogero, C. Koitzsch, M. E. González, P. Aebi, J. Cerdá and J. A. Martín-Gago, *Phys. Rev. B* **69** 045312 (2004)

14. J.-Y. Veuillen, L. Magaud, D. B. B. Lollman and T. A. N. Tan, *Surf. Sci.* **269/270** 964 (1992)

15. R. Hofmann and F. P. Netzer, *Phys. Rev. B* **43** 9720 (1991)

16. P. Wetzel, C. Pirri, P. Paki, J. C. Peruchetti, D. Bolmont and G. Gewinner, *Solid State Commun.* **82** 235 (1992)

17. C. J. Chen, *J. Vac. Sci. Technol. A* **6** 319 (1988)

18. N. D. Lang, *Phys. Rev. B* **34** 5947 (1986)

19. R. M. Feenstra, *J. Vac. Sci. Technol. B* **7** 925 (1989)

20. M. J. Hadley, Doctorial Thesis, *Physics, University of York* (1993)

21. P. Mårtensson and R. M. Feenstra, *Phys. Rev. B* **39** 7744 (1989)

22. Ph. Avouris and I. -W. Lyo, *Studying surface chemistry atom-by-atom using the scanning tunneling microscope*, in *Chemistry and Physics of Solid Surfaces*, p. 371, Springer-Verlag: Berlin (1990)

23. R. M. Tromp, R. J. Hamers and J. E. Demuth, *Science* **234** 304 (1986)

24. R. J. Hamers, R. M. Tromp and J. E. Demuth, *Phys. Rev. Lett.* **56** 1972 (1986)

25. P. Wetzel, S. Saintenoy, C. Pirri, D. Bolmont, G. Gewinner, T. P. Roge, F. Palmino, C. Savall and J. C. Labrune, *Surf. Sci.* **355** 13 (1996)

26. D. J. Spence and S. P. Tear, *Personal Communication* (2004)

Chapter 8
Conclusion

The Tm/Si(111) surface has been studied using the technique of medium energy ion scattering. The structure of the Tm silicide has been shown to be similar to that of other known rare earth silicides and a comparison of the structural parameters with those of the other RE silicides has revealed a trend across the series. Some problems with the common method of performing R-factor analysis of the MEIS data have been identified and remedies investigated. MEIS has also been used to study the initial growth of Fe on the Si(111) surface, in the monolayer regime. A structural model for the silicide formed has been proposed. The surface of the rare earth silicides has been further investigated. Scanning tunnelling microscopy has been used to study the electronic structure and their possible use as growth templates has begun to be studied using MEIS.

8.1 MEIS Study of Thulium Silicide

A quantitative MEIS study of Tm growth on the Si(111) 7 × 7 surface in the monolayer regime has been performed. Deposition of 1 ML of Tm followed by anneal at ~ 500 ˚C formed a silicide which exhibited a 1 × 1 LEED pattern. The MEIS data confirmed that the structure of this silicide is very similar to the known structure of other RE silicides. These silicides consist of a single layer of RE beneath a bulk-like Si bilayer which is rotated by 180˚ with respect to the bulk. A structural model of the Tm silicide formed was constructed based on this known basic structure. Comparisons to the experimental data of Monte Carlo computer simulations of ion scattering from the Tm confirmed such a structure. Further, comparison to multiple models allowed a quantitative determination of structural parameters, although some problems in the fitting procedure (discussed below) were identified. The bond length between the Si atoms within the

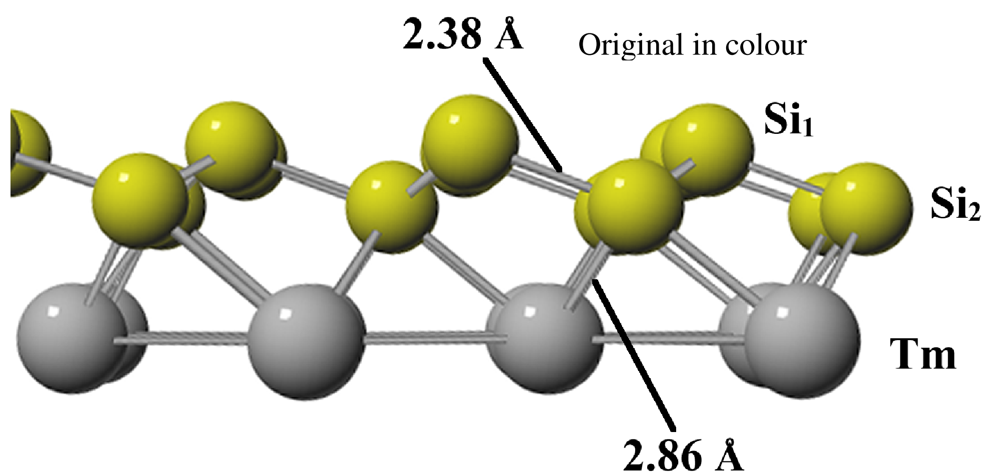

Figure 8.1: Side view of the Tm 2D silicide structure indicating the bond lengths. Bulk Si has been omitted for clarity. The silicide consists of a single RE layer beneath a bulk-like Si bilayer. The bilayer is rotated by 180 ° with respect to the bulk.

terminating bilayer was found to be 2.38 ± 0.02 Å (a 1.3 % expansion compared to the bulk Si bond), with a bilayer Si–Tm bond length of 2.86 ± 0.02 Å (Figure 8.1).

8.2 Structural Trends in 2D Silicides

The structural result for two dimensional Tm silicide has been compared to that for other 2D silicides. Initially it appeared that the structure of Tm silicide did not fit the trend evident from other RE silicides. However, further consideration revealed that the problems inherent with fitting simulations to the Tm experimental data were also present, unspotted, in the case of the other RE silicides. This may have affected the results published in the literature. These problems have been further investigated, as summerised in Section 8.3.

Such careful consideration of the structural parameters of the series of rare earth 2D silicides has led to the identification of a trend across the series. Though inherent problems have been identified in the fitting of the data to simulated models, the weight of evidence still makes a convincing argument for the trend,

even if the absolute values of the bond lengths remain uncertain. Due to the unusual nature of the 2D silicide scattering data—in which the Si–RE bond is represented by a single blocking dip—the trend can be visually discerned by comparison of the data from each of the silicides. Indeed, visually fitting simulation and experiment also reveals the trend.

As the RE mass increases the Si–RE bond length contracts slightly, decreasing by around 2 % across the series. This trend reflects that seen in the RE–Si bond lengths of bulk rare earth silicides. The Si–Si bond within the terminated bilayer remains approximately constant.

8.3 R-factor Analysis of MEIS Data

As briefly discussed above, problems were identified in the common method of comparing experimental MEIS data to computer simulations using a χ^2 R-factor. It was found that in the case of the 2D silicides the simplicity of the scattering curves allowed a reasonable comparison of experiment and simulation to be performed by eye. This revealed that the fitting of the experimental blocking curves to the simulations by the χ^2 R-factor was not the best possible. Further investigation showed that this particular form of R-factor placed too much emphasis on the fitting of blocking features at lower scattering angles. More specifically the R-factor over emphasised the fitting of the blocking dip depth whilst neglecting the fitting of the angular position of other features. In the specific case of the 2D RE silicides this had the effect of producing a poor fit to the scattering angle of the higher angle blocking dip, which corresponds to the Si_2 atomic position. It is this unusually straightforward correspondance between an individual blocking dip and an atomic position which makes the 2D silicides an ideal case for identifying and investigating such problems. It is noted that there is no guarantee that such problems do not exist in the comparison of more complex scattering curves, however, and that this represents an important issue for the MEIS community in general.

Several other R-factors were investigated to try and identify a more reliable

comparison technique. No completely satisfactory method was found, though a combination of methods could at least give some confidence in the overall results. A form of R-factor based on the Pendry R-factor of LEED analysis shows the greatest promise for a more permanent solution.

8.4 Iron Growth on Si(111)

While the Fe–Si interface has been well studied there is still little known of the crystallographic structure in the monolayer regime. The initial growth of Fe on the Si(111) surface was studied using MEIS. At a coverage of ~ 1.7 ML two phases—a 1 × 1 phase and a 2 × 2 phase—were observed by LEED, depending on anneal temperature. The 1 × 1 phase was observed after annealing at around 300 ˚C and the 2 × 2 phase at higher anneal temperatures (~ 500 ˚C). MEIS data was acquired from both phases and showed that the two are structurally extremely similar. Ions scattered from Fe atoms were seen to be blocked at characteristic angles in a number of geometries. Based initially on considerations of the location of these dips a structural model was derived. Comparison of the data with computer simulations has led to the confirmation of this structural model. The model is based on a CsCl-type structure with the bonding direction of the silicide reversed with respect to the bulk bonds. The 2 × 2 phase is formed by

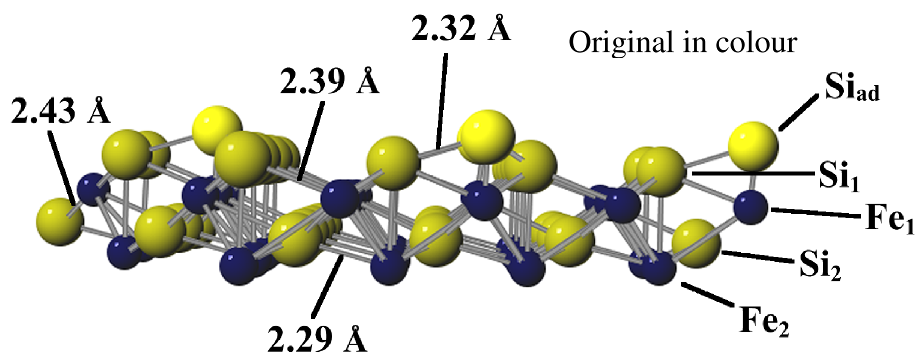

Figure 8.2: Side view of the Fe silicide, showing the 2 × 2 Si adatom layer and indicating bond lengths. Bulk Si has been omitted for clarity. The silicide is a CsCl-type structure with, in the case of the 2 × 2 phase, an additional layer of Si adatoms in a 2 × 2 arrangment.

the addition of an ordered Si adatom layer atop the 1×1 phase. Multiple computer simulations allowed this model to be refined. The surface model and bond lengths found are shown in Figure 8.2.

8.5 Studies of the Silicide Surface

8.5.1 Iron Growth on 2D Silicides

As mentioned above two dimensional rare earth silicides have been well studied over the last few years and the structure is now well established. The novel surface offered by these materials has potential as an interesting growth template, both from a fundamental science point of view and with respect to possible technological applications, such as in the field of spintronics. An initial MEIS study of the growth of Fe on 2D Ho silicide was made. On deposition of around 1.7 ML Fe immediate disruption of the interface was seen. Progressive annealing failed to restore an ordered surface, merely resulting in the migration of the Fe, and eventually Ho, into the bulk substrate. However, the presence of slight oxygen contamination may have played a roll in the experiment, as O is known to disrupt the RE 2D silicide surface.

8.5.2 STS of 2D Silicide

The electronic structure of the 2D silicides has also begun to be investigated. The 2D Ho silicide surface has been studied by atomically resolved STS. It has been found that unusually no difference between STS data from inequivalent sites could be detected, indicating a delocalised surface state. The STM image obtained would thus seem to reflect the true surface topography rather than any electronic effects. The STS data was found to be in broad qualitative agreement with theoretical calculations and experimental measurements of the 2D silicide band structure.

8.6 Future Work

Two dimensional silicides have been structurally well established. Their use as a basis for further growth however, has only just begun. Whilst the initial investigation reported in this work was disappointing in terms of the lack of ordered structure formed, it may have been affected by unintentional oxygen contamination. The further study of Fe and other metal growth (where the growth of the metal on clean Si is better understood) on these novel silicides is certainly of interest. The possibility of further Si growth, perhaps burying the single rare earth layer, also presents itself. It is hoped that the subtle differences between the 2D silicides identified by the trend in structural parameters may be of some aid in future growth investigations.

In both metal and semiconductor growth on these RE silicide templates MEIS could prove an invaluable technique. The ability to separate the signal from each element due to the mass difference allows the rare earth signal to be used as a "searchlight" to determine the structure of the layers above it. However, for such a method to reach its full potential further investigation is needed into the problems associated with the standard R-factor comparison of simulated and experimental data. Studying the performance of various R-factors applied to the RE silcides and other systems should give a fuller understanding of the problem and its extent. Certainly it seems that a more robust approach is required. Whilst other R-factors may give greater convidence in a result a more quantitative method of error estimation is required. Perhaps there is no "one size fits all" solution in terms of reliability factor, but if this is the case a larger toolbox of comparison techniques needs to be developed, with the vigilence of the experimenter being of great importance. It is the author's belief that it is vital to resolve these problems to in order to have the fullest confidence in such simulation–experiment comparisons, especially when the blocking features are more complicated than those involved in the 2D silicide comparison.

An understanding of the formation of Fe silicide at low coverages is far from complete. The Fe silicide structure found in this work could benefit from further

MEIS study utilising carefully chosen scattering geometries. These might better reveal the Si adatoms in the 2×2 phase as well as further differences between the 2×2 and 1×1 phases. As the main distinction is in the termination of the surface an STM study is suggested. This could reveal if the 1×1 phase already has an adatom overlayer which is then ordered during the anneal to form the 2×2 phase. It seems likely that the two phases could be found to coexist under some circumstances.

Glossary

2D....................................Two dimensional
AES ....Auger electron spectroscopy
AFM ....Atomic force microscopy
ARUPS.............................Angle resolved ultraviolet photoelectron spectroscopy
EELS ....Electron energy loss spectroscopy
EXAFS ....Extended X-ray fine structure
HEIS.................................High energy ion scattering
HREELS...........................High resolution electron energy loss spectroscopy
ISS ....Ion scattering spectroscopy
LEIS ....Low energy ion scattering
MEIS ....Medium energy ion scattering
ML...................................Monolayer
RBS ....Rutherford backscattering spectroscopy
RE....................................Rare earth
RHEED ....Reflection high energy electron diffraction
SEXAFS...........................Surface extended X-ray fine structure
1D....................................One dimensional
TEA ....Torodial electrostatic analyser
TSP..................................Titanium sublimation pump
SBZ ....Surface Brillouin zone
STM ....Scanning tunnelling microscope/microscopy
STS..................................Scanning tunnelling spectroscopy
SXRD ....Surface X-ray diffraction
UHV ....Ultrahigh vacuum
UPS ....Ultraviolet photoelectron spectroscopy
XPS ....X-ray photoelectron spectroscopy